

## Reply to the reports on manuscript AMT-2020-89

Thomas Trickl, September 9, 2020

The text of the two reports are given in italics, the replies normal. A file with the changes marked is submitted as supplementary material. Most changes were made as suggested, in addition to several small corrections introduced by ourselves. Unfortunately, some of the additional literature suggested in the second report had to be rejected: The reviewer obviously misunderstood the purpose of the already existing citations.

### Review 1:

*This is an overview paper that mainly summarises the lessons learned from a dedicated team that built several ozone dial systems and have operated them over no less than three decades. The paper includes many details that are excellent learning material for scientists and technicians in this field.*

*The paper is well structured.*

*There are a number of minor corrections needed:*

*pp 1*

*29 Due to a considerable technical progress meanwhile rather small changes of the mixing ratio of the order of just 30 a few parts per billion (ppb) may be resolved, which is necessary for distinguishing also the influence of minor*

*change 'meanwhile' to 'it has been shown that nowadays'*

Changed as suggested. In addition, I remove “of the order of”.

*pp 2*

*32 In the mid-1990s also a mobile ozone DIAL was built in co-operation with OHB System (Bremen, Germany; change 'also a mobile ozone DIAL was built' to 'a mobile ozone DIAL was also built'*

I changed that phrase to “was additionally built”.

*pp 5*

*8 The conversion efficiency was determined for a laser repetition rate of 10 Hz. During the lidar measurements it 9 turned out that the second-Stokes output may significantly increase when selecting a repetition rate of 100 Hz, 10 sometimes even leading to range signal overflow in the transient digitizer. This effect was unexpected and must 11 be taken into account when setting the detector supply voltages. We did not analyse this behaviour in detail.*

*It is rather surprising that this behaviour was not studied in detail or that the conversion efficiency experiments were not performed at a laser repetition rate of 100 Hz at which the measurements are actually performed. Some additional explanatory text is needed here to describe the choices of the authors. In particular, the conversion efficiency impacts the signal strength (as is described) so this is an important parameter in setting the optimal detector gain and integration time for the ozone measurements.*

I agree that an experiment at 100 Hz would have been desirable. We detected this effect rather late during routine measurements. It does not always occur (why??? Gas quality?) so that we missed it at the beginning. After I realized it (due to a slight signal overflow) the signal level was routinely

carefully adjusted.

As in the case of Kempfer et al. (1994) the conversion efficiency was determined at 10 Hz to avoid damage to the power meter. This is now explained.

*pp 5*

*22 remote control option. The manufacturer had promised external control of warm up and rotation of the change 'manufactured' to 'manufacturer'*

Changed.

*pp 6*

*6 We derive a guess of the unknown pump wavelength of our Powerlite laser model. The authors give a value for the laser wavelength that is derived from experiments with other lasers so it seems and state 'the individual values varying strongly'. Please indicate the range in which the value of the laser wavelength can vary.*

I removed "the individual values varying strongly" and add the sentence "Due to a high thermal sensitivity the emission wavelengths of Nd:YAG lasers may vary considerably from model to model." at the beginning of the paragraph. I do not understand the last sentence: The variation for 266 nm determined from the available wavelengths is specified! The standard deviation is huge in comparison with the bandwidth of a broadband Nd:YAG laser!

*pp 7 12 All lenses with focal lengths below 0.2 m are anti-reflection coated in order to avoid angle-dependent transmittances. Why are not all lenses coated?*

This is a just a design principle. The angular effect is not severe for long focal lengths. All lenses in lidar systems built after 1995 have been routinely AR coated in order to avoid losses. This was possibly not the case in the 1994 version. I added one sentence.

*pp 8 33 An aperture with four adjustable blades (custom-made by OWIS) was placed at the entrance of each*

*This could be supported by a figure/diagram.*

This is a standard procedure and does not require an extra figure.

*pp 24 The paper describes a major achievement of long term observations. A series of valuable technical recommendations is given. However, a clear statement about the prospects of continuation of the time series in Garmisch-Partenkirchen could be added.*

At this time, no final decision on the future of the stationary ozone DIAL is available. This depends on the funding for the ACTRIS European infrastructure which is not yet approved in Germany. We do not want to make a statement on the funding situation in a scientific paper.

## **Review 2:**

All comments of Reviewer 2 are given in a copy of the manuscript. We refer here to all comments made. Most changes were made as suggested, with the exception of a number of citations after critical review.

(1) Title: "Germany" added

(2) P. 1, lines 18-22: Changed.

- (3) P. 1, line 30: There has been agreement for many years that “mixing ratio” means the volume mixing ratio. Using the mass mixing ratio does make sense given the ideal gas law. Nevertheless, I added “volume” in the text.
- (4) P. 1, line 36: The papers mentioned in the review do not yield key contribution to the mixing issue. They are cited elsewhere in the paper.
- (5) P. 1, line 36: Thank you for bringing that paper to my attention! It seems that this system has the capability for lidar sounding of all three relevant species. However, I just see RH measurements in the paper. In the papers I cite here routine measurements of ozone, H<sub>2</sub>O and aerosol are presented.
- (6) P. 3, line 8: (Papayannis et al., 1990) is a feasibility study, not a general overview on stimulated Raman scattering in lidar systems. I now cite it in the Introduction. Also Tzortzakis et al. do not give a general overview. They focus on the Nd:YAG laser. There are numerous papers on specific lidar systems based on SRS. We also do not cite our own paper here.
- (7) P. 3, line 35: As mentioned that paper is a feasibility study and does not contribute to the issue of the preference on short “on” wavelengths.
- (8) P. 6, line 13: Again: This paper is not on SRS! Some information is given in Table 1, but without specifying the origin of the data. The maximum conversion efficiency given is 30 %, not 50 %.
- (9) P. 6, line 18: Why should I use the abbreviations?
- (10) P. 8, line 30: I prefer f.w.h.m. by long tradition. Same on p. 11.
- (11) P. 23, line 19: Thank you for pointing out this omission! This had been, indeed, planned by me. I adopted these papers and a review paper that verifies the OHP activities.

# Three Decades of Tropospheric Ozone Lidar Development at Garmisch-Partenkirchen, Germany

Thomas Trickl, Helmuth Giehl, Frank Neidl, Matthias Perfahl and Hannes Vogelmann

Karlsruher Institut für Technologie, Institut für Meteorologien und Klimaforschung (IMK-IFU), Kreuzeckbahnstr. 19, D-82467 Garmisch-Partenkirchen, Germany

*Correspondence to:* Dr. Thomas Trickl, [thomas@trickl.de](mailto:thomas@trickl.de), Thomas-Knorr-Str. 47, D-82467 Garmisch-Partenkirchen, Germany; Tel. +49-8821-50283

8 **Abstract.** Since 1988 two ozone lidar systems have been developed at IMK-IFU (Garmisch-Partenkirchen,  
9 Germany). A stationary system, operated at the institute, has yielded about 5000 vertical profiles of ozone from  
10 next to the ground to typically 3 km above the tropopause and has contributed data for a large number of  
11 scientific investigations. A mobile system was successfully operated in a number of field campaigns after its  
12 completion in 1996, before it was destroyed in major flooding in May 1999. Both systems combine a high data  
13 quality with high vertical resolution dynamically varied between 50 m in the lower troposphere and 250-500 m  
14 below the tropopause (stationary system). The stationary system has been gradually upgraded over the years. The  
15 noise level of the raw data has reached a level of about  $\pm 1 \times 10^{-6}$  of the input range of the transient digitizers after  
16 minor smoothing. As a consequence, uncertainties of the ozone mixing ratios of 1.5 to 4 ppb have been achieved  
17 up to about 5 km. The performance in the upper troposphere, based on the wavelength pair 292 – 313-nm varies  
18 between 5 and 15 ppb, depending on the absorption of the 292-nm radiation in-by ozone and the solar  
19 background. In summer it is, therefore, planned to extend the measurement time for-from 41 s to a few minutes  
20 in order to improve the performance to a level that will allow us to trust automatic data evaluation. As a result of  
21 the time needed for manual refinement For longer time series automatic data acquisition has been used. The  
22 number of measurements per year has been confined to less than 600. since fully automatic data evaluation has,  
23 still, had its limitations and some manual actions are needed. For longer time series automatic data acquisition  
24 has been used.

25 *Key words:* Tropospheric ozone, lidar, differential absorption, DIAL

26 1. Introduction

27 Lidar measurements of tropospheric ozone have resulted in important contributions to atmospheric research.  
28 Large variations of the concentrations on time scales of less than one hour may be observed, which have led  
29 insight into a number of tropospheric transport processes (see Table A1 for a large number of examples). In  
30 addition, measurements with ozone lidar systems have contributed to numerous air-quality studies (Table A2).  
31 Due to a considerable technical progress meanwhile nowadays, rather small changes of the volume mixing ratio  
32 of the order of just a few parts per billion (ppb) may can be resolved, which is necessary for distinguishing also  
33 the influence of minor contributions and for reliable trend studies.

34 Still, important tasks in tropospheric ozone research exist such as a clarification of the positive ozone trend  
35 observed until 2003 at high-lying observational sites in Europe (Scheel, 2003; Ordoñez et al., 2007) despite the  
36 pronounced reduction of ozone precursors over Europe (Jonson et al., 2006; Vautard et al., 2006), a detailed  
37 analysis of the rather complex contributions of different sources to long-range transport, or the influence of  
38 vertical mixing on free-tropospheric layers, in particular on stratospheric air intrusions (Trickl et al., 2014; 2015;

1 2016). Although vertical sounding, including lidar measurements of complementary quantities such as aerosols  
2 and water vapour (e.g., Trickl et al., 2014; 2015, 2020; Strawbridge et al., 2018; Fix et al., 2019), can yield key  
3 information for the understanding of the role of the underlying atmospheric processes, for a long time there was  
4 no significant growth in the number of tropospheric ozone lidar stations towards something like an international  
5 network. By contrast, more and more ozone lidar systems have even been shut down. Opposite to this  
6 development, recently a Tropospheric Ozone Lidar Network (TOLNet, <https://www-air.larc.nasa.gov/missions/TOLNet/>) with seven lidar stations was established in North America (e.g., Newchurch et al., 2016; Wang et al.,  
7 2017; Leblanc et al., 2018). It is important to note that even vertical profiles from the impressive MOZAIC  
8 (Measurements of Ozone and Water Vapor by Airbus In-Service Aircraft) (Marenco et al., 1998) data base are  
9 not able to resolve the fine-scale temporal variability of the vertical distribution of trace constituents because of  
10 the rather confined time slots for the aircraft departures and arrivals at the individual airports. Satellite  
11 measurements cannot yield the necessary information because of presently insufficient spatial resolution and  
12 global coverage within a day.

13 With a few exceptions mostly ultraviolet (UV) differential-absorption lidar (DIAL) systems for tropospheric  
14 applications have been proposed and developed since the late 1980s–1975 (Papayannis et al., 1990; Table A3).  
15 Here, the advantages of high Rayleigh backscattering and strong absorption cross sections are combined. In  
16 Europe, the TESLAS (Tropospheric Environmental Studies by Laser Sounding) subproject of EUROTAC  
17 (EUREKA Project on Transport and Chemical Transformation of Environmentally Relevant Trace Constituents  
18 in the Troposphere over Europe; EUROTAC, 1997) has resulted in the co-ordinated development of several  
19 state-of-the art ozone lidar systems (TESLAS, 1997). Lidar sounding of tropospheric ozone is a demanding  
20 technical task (Weitkamp et al., 2000) because of the considerable dynamical range of the backscatter signal  
21 covering up to about eight decades, the presence of aerosols and clouds, interfering trace gases such as SO<sub>2</sub> and  
22 NO<sub>2</sub>, the solar background (stratospheric ozone measurements are normally made during night-time), all  
23 necessitating an elaborate optical and electronic design. The data evaluation is based on derivative formation that  
24 is particularly sensitive to signal perturbations, which that set limitations to resolving the frequently rather small  
25 changes in free-tropospheric ozone.  
26

27 At IFU (Fraunhofer-Institut für Atmosphärische Umweltforschung; now: Karlsruher Institut für Technologie,  
28 IMK-IFU), a differential-absorption lidar (DIAL) with a particularly wide operating range from next to the  
29 ground to the upper troposphere was completed in 1990 in the framework of TESLAS and subsequently applied  
30 for a full year (1991) within the TOR (Tropospheric Ozone Research) subproject of EUROTAC (Carnuth et al.,  
31 2002). The operating range of this system was extended to roughly 15 km by introducing three-wavelength  
32 operation (Eisele and Trickl, 1997). Due to thoroughly upgrading of the data-acquisition system an uncertainty  
33 level of 1.5 to 4 ppb has been achieved up to the mid-troposphere (slightly higher in the upper free troposphere,  
34 depending on the ozone concentration and solar background).

35 In the mid-1990s also a mobile ozone DIAL was additionally built in co-operation with OHB System (Bremen,  
36 Germany; Brenner et al., 1997). This system, that was completed in spring 1996 and presented at the 1996  
37 International Laser Radar Conference, could be operated in a vertical range between 0.2 and more than 4 km  
38 with a similar accuracy as our stationary system at low altitudes and was used in a number of field campaigns  
39 before it was destroyed by 2 m of water during major flooding in southern Bavaria in May 1999 when waiting  
40 for the VOTALP "Munich field campaign" (VOTALP II, 2000).

41 In this paper we review the experience gained with these two lidar systems. The development of these two  
42 systems has significantly contributed to the state of the art in this field. Meanwhile, even the dream of a

1 meaningful automatic data-evaluation looks feasible due to the technical progress made. Most approaches and  
2 instruments used are the same in both lidar systems, which simplifies the description.  
3 Most of the paper is devoted to the stationary DIAL. We describe only deviating design properties of the much  
4 compacter mobile system such as the laser approach or the wavelength-separation technique chosen. This system  
5 has been extensively used over three decades, but no full-size technical description has been given. We do not  
6 want to give a full description of all the technical improvements made over the years. Just the decisive steps are  
7 reported.  
8 Most of the approaches of the ozone DIAL systems have been successfully transferred also to the other lidar  
9 systems of IMK-IFU.

10 **2. General design considerations**

11 In both IFU DIAL systems fixed-frequency lasers and stimulated Raman shifting in H<sub>2</sub> and D<sub>2</sub> have been used  
12 for generating suitable “on” and “off” wavelengths (see (de Schoulenikov et al., 1997; Milton et al., 1998) for  
13 general overviews). In this way just a single high-power laser source is needed. Both systems are three-  
14 wavelength lidars with two “on” wavelengths and one “off” wavelength. This offers the opportunity of a wide-  
15 range operation starting below 0.3 km above the ground, with stronger absorption and accuracy as well as good  
16 vertical resolution for the shorter of the two “on” wavelengths and a range extension with lower vertical  
17 resolution for the longer “on” wavelength. In addition, the comparison of ozone profiles obtained from two  
18 separate wavelength pairs allows for internal quality control. In fact, as described in Sect. 6, for an optimum  
19 alignment and sufficient backscatter signal the agreement between the different ozone profiles is almost perfect.  
20 Apart from the wavelength separation methods the basic optical layout principles and detection electronics are  
21 mostly the same. Both systems feature automatic data acquisition.  
22 The stationary system (Fig. 1) is operated in two separate, rather large laboratories at IFU (47.477° N, 11.064° E,  
23 740 m a.s.l.). This offers several advantages such as a simple optical layout, good alignment control due to long  
24 beam paths, reduced thermal drifts because of no direct exposition of the laser system to outside air, or the long  
25 distance between detection electronics and the interfering laser system. Two separate power systems are used for  
26 laser and electronics. The laser PC is connected to the cleaner ~~eletronics~~-power system [for the electronics](#) and  
27 controls the laser system via optical fibres. Remote control of the laser is achieved via RS232.  
28 Due to the clean-air conditions prevailing at this rural site the wavelength choice is less critical. The ambient  
29 concentrations of SO<sub>2</sub> and NO<sub>2</sub>, species with absorption bands in the spectral range of ozone DIAL systems, at  
30 are low which is known from the local long-term monitoring stations. Thus, the choice of the laser source was  
31 determined by high power in order to achieve a short measurement time. Krypton fluoride lasers have been used  
32 (Kempfer et al., 1994; Eisele and Trickl, 1997), since 1994 a model with a maximum available average power of  
33 54 W at 248.5 nm (all wavelengths in this paper are given for vacuum).  
34 The laser choice was different for the mobile system (Fig. 2). A frequency-quadrupled Nd:YAG laser with up to  
35 4.2 W of average power at 266.1 nm served as the basic source of ultraviolet (UV) light. This approach was  
36 preferred for several reasons: Due to the expected operation also in heavily polluted areas at least one  
37 wavelength combination (266 nm – 299 nm) reduces the cross sensitivity with respect to SO<sub>2</sub> and NO<sub>2</sub> to about  
38 0.01 ppb ozone per ppb of these species. Under such conditions, also the perspective of low interference by  
39 aerosols is important, which is fulfilled for short “on” wavelengths (Völger et al., 1996; Eisele et al., 2005).  
40 Thus, wavelength combinations involving 266 nm are favourable. Finally, due to the choice of a solid-state laser  
41 source the dangerous gas handling in an excimer laser could be avoided, an issue for the mobile operation.

1 A clear design goal for the mobile system had been a vertical range significantly exceeding the boundary layer  
2 by a few kilometres. This requirement had been seen as crucial for meaningful investigations during air-pollution  
3 field campaigns. The mobile ozone DIAL was mounted inside an air-conditioned truck (Fig. 2) and was designed  
4 for autonomous operation with an on-board power generator, batteries, automatic positioning (GPS) and a  
5 detailed safety control management including rain and wind sensors, shutter control of the laser, and many  
6 interlocks. Critical safety conditions immediately overrode any other action. The operator could be automatically  
7 informed about incidents in his hotel during night-time via telephone. After rain, the system could be restarted  
8 automatically, unless the laser was shut down (see Sect. 3.2).

9 The detection system of this DIAL was much simpler, with a less demanding optical set-up (single telescope for  
10 both near- and far-field detection, simple filter polychromator) and with less electronic components due to a  
11 sequential emission of two of the three operating wavelengths. All this resulted in a considerable reduction of  
12 costs, at that time an attractive perspective also in view of the goal of our industrial partner of an affordable  
13 commercial system.

14 Overall specifications of the two systems are listed in Tables 1 and 2. All optical components and dielectric  
15 coatings have been provided by Laseroptik G.m.b.H. (Garbsen, Germany) unless otherwise specified.

### 16 3. Transmitter Design

#### 17 3.1. Stationary Lidar

18 The transmitter of the system (Fig. 1, Table 1) is based on a KrF excimer laser (Lambda Physik, LPX 250,  
19 maximum repetition rate 100 Hz) consisting of a tunable narrowband oscillator and a three-pass power amplifier.  
20 CaF<sub>2</sub> is used for transmitted optics. CaF<sub>2</sub> is not birefringent and, thus, polarization effects (Kempfer et al., 1994)  
21 and ageing are avoided. The energy was considerably enhanced by anti-reflection (AR) coating the outer side  
22 windows of the amplifier gas cell and the beam splitter in front of the energy monitor A pulse energy of up to  
23 540 mJ was measured several metres away from the laser where divergent components also emerging from the  
24 amplifier can be separated and blocked by an aperture. For the lidar measurements the laser energy is usually set  
25 to 400 mJ. The unstable cavity of the amplifier yields a highly collimated rectangular beam with a divergence of  
26 0.2 mrad. The wavelength was set for maximum output and the prism-grating combination never touched again.  
27 In 2010 measurements with a HighFinesse WS6 ( $\Delta\lambda = 0.6$  pm) wavelength meter carried out over several days  
28 yielded 248.5078 nm  $\pm$  0.0060 nm, in agreement with the results of Kempfer et al. (1994). The spectral  
29 bandwidth is specified as 0.2 cm<sup>-1</sup> (6 GHz). Locking the amplifier to the oscillator can be nicely verified by an  
30 enhancement of the pulse energy by up to 70 mJ under our standard operating conditions.

31 The output of the KrF laser is split by a 50-% beam splitter and focused into two Raman cells with  $f = 1.0$ -m  
32 AR-coated plano-convex CaF<sub>2</sub> lenses. One cell is filled with hydrogen and the other one with deuterium, and the  
33 same pulse energy per cell as previously used for a single cell (Kempfer et al., 1994) is ensured (almost 0.2 J). A  
34 total of six Stokes components are generated in hydrogen, just 277.124 nm (S1) and 313.188 nm (S2) are taken  
35 (Table 1). For deuterium the second Stokes (S2) component (291.838 nm) is used. The outer surfaces of the CaF<sub>2</sub>  
36 windows of the Raman cells are AR coated. The inner ones are not coated because of the possibility of ageing in  
37 the presence of photolysed hydrogen. The pump radiation leaving the evacuated Raman cells is of the order of  
38 160 mJ. The output of the Raman cells is combined with a pair of dichroic beam combiners and collimated with  
39 an  $f = 5$ -m, 150-mm-diameter concave spherical mirror. The beam combiners reflect 99 % of the 292-m  
40 radiation at 45° and transmit 88 to 90 % of all the other relevant spectral components. Overlap and pointing of

1 the 292-nm beam are optimized by placing a wire cross in front of the D<sub>2</sub> cell or behind the second beam  
2 combiner, by watching the images of the cross in front of mirror M4.

3 The Raman conversion efficiency obtained with the LPX 250 laser system is lower than that previously  
4 published (Kempfer et al., 1994). We ascribe this to the smoother energy distribution in the beam profile of the  
5 new laser. As an example, Fig. 2-3 shows the conversion efficiencies obtained for hydrogen for a laser pulse  
6 energy of almost 200 mJ per Raman cell, attenuated by the optics, in particular by the single-side AR coated cell  
7 entrance windows). The sum of all conversion efficiencies is less than 1.0 starting at low pressures already. This  
8 loss of overall energy is tentatively ascribed to optical breakdown. Above 3 bar the loss starts to level off. The  
9 non-negligible fourth Stokes emission (Kempfer et al., 1994) was not determined. The maximum second-Stokes  
10 conversion efficiency for deuterium is approximately 17 % (at 11 bar). The operating pressures have been  
11 chosen around 3.3 bar and 11 bar for H<sub>2</sub> and D<sub>2</sub>, respectively.

12 The conversion efficiency was determined for a laser repetition rate of 10 Hz, in order to avoid damage to the  
13 power meter used. During the lidar measurements it turned out that the second-Stokes output may significantly  
14 increase when selecting a repetition rate of 100 Hz, sometimes even leading to range signal overflow in the  
15 transient digitizer. This effect was unexpected and must be taken into account when setting the detector supply  
16 voltages. We did not analyse this behaviour in detail.

17 Linear polarization is important for single-line output of the Raman shifters (Kempfer et al., 1994). We placed a  
18 Glan prism and a Fresnel rhomb (both from Halle) in the beam between oscillator and amplifier. All mirrors and  
19 beam splitters of the transmitter section were manufactured with minimum polarization sensitivity. The Fresnel  
20 rhomb is rotated for optimum backscatter signal (Fig. 4). The strong modulation of the lidar signal in Fig. 4 is  
21 mainly caused by the holographic gratings used in the receivers (Sect. 3).

22 Due to the high average power of the laser system the time for a single ozone measurement, carried out with a  
23 repetition rate of 99 Hz, is as short as 41 s.

#### 24 **3.2 Mobile Lidar**

25 The pump laser of the mobile DIAL was a frequency-quadrupled Nd:YAG laser with 30 Hz repetition rate and  
26 pulse energies of up to 140 mJ at 266 nm (Continuum, Powerlite 9030). The laser was selected because of a  
27 remote control option. The manufactured manufacturer had promised external control of warm up and rotation of  
28 the frequency doubling and quadrupling crystals. The 1064-nm and 266-nm powers were measured by two  
29 Molelectron power meters for a PC-based power optimization. However, the computer control never worked  
30 properly: Automatic warm up of the laser was never achieved. The reason was a conflict with “keep-alive”  
31 pulses that had to be sent by the external control.

32 The quadrupling was achieved by using BBO (beta barium borate). This approach yielded high conversion  
33 efficiency and moderate thermal loading. However, after more than one year of infrequent operation of the lidar  
34 the surface of the crystal started to degenerate. This turbid layer did not strongly reduce the UV emission and  
35 polishing was, therefore, postponed.

36 At maximum pump energy (1.6 J at 1064 nm) ring-the 266-nm radiation exhibited a ring-shaped mode, at a  
37 pulse-energy level of 140 mJ. We reduced the pulse energy to 1.1 J. Still, 120 mJ could be produced, now with a  
38 filled beam profile. However, a hot spot formed that focussed in the Raman-shifting compartment and we  
39 reduced the UV output to about 70 mJ for safety reasons. This hot-spot problem was solved by the manufacturer  
40 in a later (“Precision”) version of the laser.

1 A ceramics shutter was added to the exit holes of the Powerlite laser that was controlled by both the safety  
2 system and the lidar PC. Closing the shutter was preferred to switching off the laser oscillator in order to  
3 maintain stable thermal conditions in the laser during an interruption.

4 A side view of the lidar including the entire transmitter is given in Fig. 2, the lower level of the frame in Fig. 5.  
5 Figure 5 shows the Raman shifting compartment that also contained a 6:1 beam expander used for reducing the  
6 beam divergence. Rotating beam splitters were used for directing the laser pulses into the H<sub>2</sub> and D<sub>2</sub> cells. These  
7 beam splitters were based on a circular quartz plates differently coated on the two halves of the surface, high  
8 reflecting for the lidar wavelengths on one half and high transmitting on the other one. The rotation was  
9 synchronized to the laser pulses. The control unit issued pulses for identifying the Raman cell actually passed for  
10 the data-acquisition system. Two precision motors with measured out-of-axis rotation of just about  $\pm 2$   $\mu$ rad and  
11  $\pm 40$   $\mu$ rad, respectively, were chosen (KaVo, model EWL 4025; with custom-made electronic control).

12 Due to a high thermal sensitivity the emission wavelengths of Nd:YAG lasers may vary considerably from  
13 model to model. We derive a guess of the unknown pump wavelength of our Powerlite laser model from (Trickl  
14 et al., 1989; 2007) and wavelength measurements for three other injection-seeded Nd:YAG lasers in our  
15 laboratory. The average pump wavelength of 266.120 nm  $\pm$  0.011 nm (the individual values varying strongly).

16 This yields first-Stokes-shifted wavelengths of 289.103 nm (in D<sub>2</sub>) and 299.209 nm (in H<sub>2</sub>).

17 We reached maximum first-Stokes (S1) conversion efficiencies of almost 50 % both in hydrogen and deuterium  
18 at pressures of as low as 0.9 bar and 1.6 bar, respectively. This is remarkable in two respects: the theoretical  
19 Raman conversion efficiency reaches 50 % at higher pressures and the Raman gain of deuterium is substantially  
20 smaller than that of hydrogen (de Schoulepnikov et al., 1997). A total of five Stokes orders and one anti-Stokes  
21 order were visually observed for hydrogen, less orders in deuterium. There was some contribution of the second  
22 Stokes order (particularly low at 1 bar due to gain competition with S1), but those for the higher orders were  
23 below the 1 mW detection threshold of the power meter used. Starting at pressures below the threshold for  
24 Raman conversion absorption was realized and, in H<sub>2</sub>, the conversion efficiency rapidly dropped to zero above  
25 about 1 bar. The same effect was observed also in pure helium and argon. Thus, we ascribe these observations to  
26 laser-induced breakdown. The role of the hot spot in igniting this breakdown could not be examined. Quite  
27 obviously, the Stokes emission was emitted prior to the breakdown maximum (see also Trickl, 2010). In any  
28 case, the high conversion efficiency achieved was more than enough for the lidar operation.

29 Motivated by the hot-spot problem the focussing lens was replaced by a pair of crossed  $f = 1.0$  m cylindrical  
30 lenses during the final phase of operation of this lidar system. As suggested in by Perrone and Piccinno (1997)  
31 this may result in a softer focus, a larger focal volume and higher Raman conversion. The maximum possible  
32 distance between the two lenses was about 12 cm and was chosen for the lidar operation. In Fig. 6 the conversion  
33 efficiencies as a function of cell pressure for this distance and also for the minimum possible distance of about 5  
34 cm is given. A clear change in behaviour was seen. The transmitted pump energy no longer dropped to zero  
35 above 1 bar. As one would expect the depletion for pressures up to 2 bar is smaller for the larger distance  
36 between the two lenses. Quite interestingly, the pump depletion in D<sub>2</sub> was much less pronounced than that in H<sub>2</sub>.  
37 Despite these obvious improvements, the maximum conversion efficiency just rose for H<sub>2</sub> (to 61 %, comparable  
38 to the results by de Schoulepnikoff et al., 1997).

39 The rectangular beam-steering mirror was mounted on two mutually orthogonal rotation stages (OWIS). The  
40 beam pointing angle was set on the lidar PC.

41 **4. Receiver Design**

1    **4.1 Design Principles**

2    The optical layout of the IFU lidar systems built or modernized since 1990 is based on several design principles:  
3    (1) The use of Newtonian telescopes for a less critical alignment than in the case of a Cassegrain telescope and  
4    for an easier discrimination of the near-field signal.  
5    (2) Separate detection in near-field and far-field channels in order to reduce the giant dynamical range of the  
6    backscatter signal covering roughly eight-decades.  
7    (3) No optical elements or detectors are placed close to the focal points in order to avoid a modulation of the  
8    backscatter signal by the near-field scan of the focal point across inhomogeneously transmitting or detecting  
9    surfaces. A severe example for a photomultiplier tube (PMT) is given by Simeonov et al. (1999). In  
10   particular, this principle also strongly prohibits the use of optical fibres because of their unknown input  
11   surface quality (apart from the coupling losses).  
12   (4) Particularly inhomogeneous surfaces must be placed in or very close to image planes (exit pupils) where the  
13   image spots and the light bundle as a whole stay stable in space. As a result even very long beam paths do  
14   not matter as long as no aperture is hit due to an excessive pointing drift of the laser beam. In this way a  
15   stable performance is achieved over long periods of time. Also the diameter of the light bundle reaches its  
16   minimum in the exit pupil, and it is important to place components with limited diameter in (or very close  
17   to) this plane, such as detectors, optical filters, gratings or beam splitters.  
18   (5) All lenses with focal lengths below 0.2 m ~~are must be~~ anti-reflection coated in order to avoid angle-  
19   dependent transmittances. Anti-reflection coating was applied to all lenses in IFU lidar systems after 1995  
20   also to avoid transmission losses.

21   In most of our lidar systems we have chosen a modular design composed of a series of relay-imaging pairs of  
22   equal lenses (distance  $2f$ ) with beam splitters or filters close to the centre between the lenses (Vogelmann and  
23   Trickl, 2008; Giehl and Trickl, 2010; Klanner et al., 2020). This approach is also implemented in the receiver of  
24   the stationary ozone DIAL, however with a holographic grating instead of optical filters. However, in the mobile  
25   system a convergent beam path was chosen behind the ocular of the telescope in order to save space.

26   **4.2 Telescopes**

27   *Stationary system*

28   The large dynamical range of the backscattered light of about eight decades is reduced by using two separate  
29   Newtonian telescopes (Kempfer et al., 1994) as shown in Fig. 1 (manufacturers: Vehrenberg (entire small  
30   telescope) and Lichtenknecker (mirrors only). The primary mirrors have diameters of 0.13 m and 0.5 m, and  
31   focal lengths of 0.72 m and 2.0 m, respectively. The axes of the two telescopes are in plane with the outgoing  
32   laser beam and located about 0.2 m and 1.8 m from that of the beam, respectively.  
33   The solar background was reduced by both black surfaces and a black circular baffle around the input path of the  
34   backscattered radiation. This turned out to be insufficient after introducing new detectors in 2012 that are more  
35   susceptible to the background (Sect. 4.4).  
36   The approximate vertical range is 0.2 to 2.5 km above the ground for the small near-field telescope and 1.5 to 3-  
37   5 km above the tropopause for the large far-field telescope with a dynamically adjusted vertical resolution of 50  
38   to 300-500 m. Both telescopes are combined with 1.1-m grating spectrographs. This led to a much better  
39   daylight rejection in comparison with Kempfer et al. (1994).  
40   The alignment of the small telescope is very difficult, given the very long beam paths through the polychromator  
41   (Sect. 3.3). It was highly difficult to avoid nonlinearities of the results on the first few hundred metres. The

1 signal had to be attenuated by a factor of ten. The solution was found a few years ago. During the routine four-  
2 quadrant (“telecover”) testing (Freudenthaler et al., 2008), introduced for quality assurance within EARLINET  
3 (European Aerosol Research Lidar Network; e.g., Amodeo et al., 2010; <http://www.earlinet.org/>), it turned out  
4 that almost the entire near-field return passed through the quadrant on the side of the outgoing laser beam  
5 (named “north” sector). This explains the observed sensitivity to misalignment.

6 The north sector of the telescope was subsequently covered by a triangular piece of cardboard. After this, the  
7 alignment sensitivity of the near-field receiver (including the spectrograph, see below) disappeared, a stable  
8 linear performance was obtained and the signal was attenuated to an acceptable level due to the missing “north”  
9 quadrant. Another important consequence was that no additional attenuators had to be used after this  
10 change. Most importantly, after the design change a very reliable diurnal variation of ozone could be retrieved in  
11 the boundary layer with a morning minimum and an afternoon maximum.

12 The alignment of the far-field receiver has remained stable during the past 24 years. The only parameters  
13 routinely optimized have been the laser-beam pointing and the overlap of the two partial laser beams from the  
14 two Raman shifters. Slight deviations in the overall beam pointing do (inside the slits in the focal planes) not  
15 matter (despite the long distances in the receivers) due to the imaging principles applied: The final and the  
16 intermediate images of the primary mirrors are not shifted.

17 ***Mobile System***

18 A single Newtonian telescope with an  $f = 1.56$  m, 317.5-mm-diameter principal mirror (Intercon Spacetec) was  
19 used. The distance between the laser and the telescope axes was 0.5 m. The exit of the telescope towards the  
20 detection polychromator was (horizontally) perpendicular to these two axes.

21 **4.3 Wavelength Separation**

22 ***Stationary System***

23 After 1994, the wavelength separation for the stationary system was achieved with two identically built 1.1-m  
24 grating spectrographs, one per telescope (Figs. 1 and 7). A grating spectrograph has the advantage of the  
25 transverse near-field-far-field beam walk and the spectral separation taking place in separate, mutually  
26 orthogonal planes. As explained in more detail by Kempfer et al. (1994), a near-Wadsworth configuration was  
27 chosen in order to reduce the astigmatism to an acceptable level. The Wadsworth angle for a given wavelength is  
28 defined by an exit of the first diffraction order along the grating normal. As shown by ray tracing the spectral  
29 resolution is also close to optimum for this approach and was expected to be 0.2 nm. The design described by  
30 Kempfer et al. (1994) was extended by placing  $f = 80$  mm lenses in front of the detectors for imaging the  
31 primary mirrors of the telescopes on to the photocathode of the PMT. The spherical grating (Carl Zeiss,  $r = 1995$   
32 mm) was also placed in an image plane of the primary mirror to minimize the diameter of the radiation bundle.  
33 Detailed numbers are given by Eisele (1997).

34 The true spectral resolution was determined with a mercury lamp to be about 0.35 nm, achieved with low-  
35 intensity emission lines not exhibiting line broadening due to absorption in the lamp prior to emission. Due to  
36 the defocusing caused by the beam walk the effective spectral range for the components of the integrated lidar  
37 return is 1.0 nm (full width at half maximum, f.w.h.m.), but with sharp edges. The grating efficiency was  
38 specified as 70 % by the manufacturer (Carl Zeiss, Oberkochen) in auto-collimation, which may be different for  
39 the Wadsworth configuration.

1 An aperture with four adjustable blades (custom-made by OWIS) was placed at the entrance of each  
2 spectrograph in the focal plane of the primary mirror for reducing the level background light. In the large  
3 receiver the vertical blades were adjusted to block the near-field return and to transmit the return from all longer  
4 distances. These vertical blades were never touched again and laser beam steering mirror always set for a peak  
5 signal at 8.0  $\mu$ s. The horizontal blades are set for a slit width of 2-3 mm, after alignment with a narrow slit. The  
6 minimum slit width possible for the S1 radiation is 0.7 mm (0.35 mrad), more being needed for the S2  
7 components. The consequence of the small spot size is a low susceptibility to typically observed laser pointing  
8 drifts, and the 277-nm return always yields correct ozone values.

9 Further adjustable slits (widely open) were placed in the secondary focal planes in front of the PMTs. However,  
10 this was just for occasionally controlling the alignment since no cross talk between the different wavelength  
11 channels was observed. As mentioned no alignment drifts were found.

12 As already mentioned in Sect. 3.1 the lidar signal varies with the polarization angle of the laser (Fig. 4). An  
13 approximate 5:1 sinusoidal modulation is seen. The polarization angle was set for optimum signal.

#### 14 **Mobile System**

15 The polychromator design for the mobile system is quite different and is based on dielectric mirrors,  
16 beam splitters, an edge filter and adjustable-slit apertures (Fig. 8). The 289 nm and 289 nm returns were  
17 separated by temporal discrimination, triggered by the rotating beam splitters described in Sect. 3.2. The data  
18 were stored in different areas of the transient digitizers. The separation of the larger gap between 266 nm and the  
19 two longer wavelengths could be conveniently achieved by pairs of dielectric beam splitters (BS3), each of them  
20 transmitting just 3 % of the longer wavelengths and fully reflecting the 266 nm component at an incidence angle  
21 of 45°. In this way, two 266-nm channels were available for both the near- and the far-field sections of the  
22 polychromator. As seen in Fig. 8, the entire arrangement is highly symmetrical and almost identical for the near-  
23 and far-field parts. A 1:100 beam splitter and an O.D. 1.0 neutral density filter (Andover) were used to separate  
24 and to attenuate the near-field return. In the far-field section the signal was first adjusted to match perfectly the  
25 near-field signal for low PMT gain. After this procedure, OWIS adjustable-blade apertures (see above), placed in  
26 the focal planes in front of the PMTs, were used to cut off the strong near-field return that was shifted  
27 horizontally (due to the perpendicular geometry of the outgoing laser beam, the telescope axis and the telescope  
28 output axis). Finally, the PMT gain was increased to maximize the far-field signal. This approach is a rather  
29 simple alternative to the use of two telescopes as done in our stationary system and is also applied in our water-  
30 vapour DIAL (Vogelmann and Trickl, 2008). However, it requires very constant pointing of the outgoing laser  
31 beam in order to avoid changes in signal level. This was not perfectly the case for the laser used here, but could  
32 be verified for the more recent (“Precision”) version of the Powerlite laser of the H<sub>2</sub>O DIAL.

33 An OWIS adjustable-slit aperture was also placed in the focal plane of the telescope (top of Fig. 8) for the  
34 reduction of the solar background. To account for the changing position of the “focus” as a function of the  
35 changing position of the outgoing laser pulse the orientation of the slit was horizontally tilted (i.e., perpendicular  
36 to the orientation in the stationary system, due to the 90° rotation of the telescope exit). The vertical blades of the  
37 aperture could be closed to 1.7 mm (corresponding to an acceptance angle of 1 mrad) without a loss of signal,  
38 but were set slightly wider during normal operation.

39 Each of the four detection channels principally look the same, apart from the different surfaces of the  
40 components (HR1 (high reflector for 266 nm) and BS3). As mentioned the set-up deviates from the conventional  
41 modular set-up with relay-imaging lenses. The  $f_l = 100$  mm ocular (L1) does not collimate the lidar return, it

1 directly refocusses the radiation to an intermediate focal point. In this way, the overall distance to the detectors  
2 could be shortened. Just one additional lens ( $L_2, f_2 = 50$  mm) was used for exactly imaging the principal mirror  
3 of the telescope onto the photocathodes of the PMTs. Most optical components were placed in the vicinity of the  
4 intermediate images of the primary mirror (green dots in Fig. 8).

5 One deficiency that was never overcome before the destruction of the system was that just a single PMT was for  
6 both “on” and “off” channels in the far-field section. Since the “on” signal peak is already rather small at the  
7 beginning of the far-field signal, the “off” component should be attenuated, e.g., by rotating quartz plates with  
8 two differently coated halves similar to those next to the Raman shifter should be used. This would allow the  
9 “off” signal to be reduced to about the same level as the “on” signal, and a higher PMT gain could be used.

#### 10 4.4 Detectors

11 The detectors are key components of our lidar development, which calls for an explicit description. After the  
12 experience in early years (Kempfer et al., 1994) we used until April 1996 exclusively the fourteen-stage EMI  
13 9893B photomultiplier tubes (PMTs). For linear performance the 9893B detectors were operated with maximum  
14 analogue signal levels below 10 mV (50- $\Omega$  termination). This means that the very high gain of this fourteen-  
15 dynode PMT (up to eight decades) is completely unnecessary. The big plus was range gating (Kempfer et al.,  
16 1994) lifting the far-field signal level to values mostly well above the electronic imperfections of the signal  
17 processing system. The range-gating circuit was further improved for repetition rates of more than 20 Hz.

18 However, after very positive testing in 1995, we introduced Hamamatsu H5783P-06 PMT modules to both  
19 DIAL systems in spring 1996 (Brenner et al., 1997; Eisele and Trickl, 1997). The miniature PMT features a  
20 built-in Cockcroft-Walton power supply, an 8-mm-diameter photocathode and six mesh dynodes, leading to a  
21 maximum current gain of  $3 \times 10^5$ . This gain is sufficient for obtaining a very big lidar signal. This module is  
22 extremely linear over at least five decades for analogue signals up to at least 100 mV (50  $\Omega$  termination) in the  
23 operating voltage range around the most recommended 800 V. Fluorescence-free Corion SB-300-F short-pass  
24 filters were placed on the PMTs and efficiently removed radiation for wavelengths beyond 320 nm.

25 The small size of the modules allowed us to achieve a very compact design of the polychromators of the two  
26 lidar systems. In particular, side-by-side operation of all three PMTs in the spectrographs of the stationary DIAL  
27 became possible. These modules were used in our stationary system for more than fifteen years without  
28 discernible signs of ageing.

29 Finally, driven by the hope for further improvement, we replaced in 2012 the Hamamatsu H5783P-06 modules  
30 by an actively stabilized version optimized for us in 1999 for our three-wavelength aerosol lidar (Kreipl, 2006)  
31 by Romanski Sensors (RSV). This device had to be based on the follow-up PMT version Hamamatsu R7400U-  
32 03, because the 5600 series was longer available. The socket was further modified to deliver optimized single-  
33 photon spikes without the ringing of the original PMTs (Figs. 9a and 9b). The power connection cable is  
34 shielded, but the shield is grounded just on one side.

35 Similar to the Hamamatsu module the RSV socket generates a clean reference voltage (5 V). This voltage is  
36 produced from the 15 V supply voltage. The 5-V reference, corresponding to a PMT voltage of 1000 V, is then  
37 returned to the power supply where it is divided to the adjustable final control voltage level (0 to 5 V) that is sent  
38 back to the detector (Fig. 3.12 of Kreipl (2006)). This loop was necessary to clean the lidar signals to a level  
39 below  $10^{-5}$  of the peak signal. Sending in just an external control voltage had resulted in an unacceptable baseline  
40 crossing of about  $10^{-4}$  of the peak lidar signal.

1 The diameter of these detector modules, 50 mm, was too large for operating the PMTs for 277 nm and 292 nm  
2 side by side in the spectrograph of the stationary system. In order to make this possible RSV delivered four of  
3 the modules with the small PMT tubes mounted off axis.

4 Testing of the PMTs in our three-wavelength aerosol lidar had shown that above peak signals of 40 mV signal-  
5 induced nonlinearities become observable that are attributed to photocathode overload (Fig. 3.10 of Kreipl  
6 (2006); English version: <http://www.trickl.de/PMT.PDF>). However, this result was obtained for a PMT supply  
7 voltage of the order of just 450 V, and, therefore, corresponded to an excessive photon flux (see Fig. 10 for a  
8 gain curve). For voltages around 800 V (maximum: 1000 V), as recommended for photon counting, the incident  
9 radiation levels for creating the same signal are roughly 100 times lower. As a consequence, much higher signal  
10 levels can be afforded and, in recent years, we have routinely set the peak signals in the far-field receiver to 70  
11 mV, this being a rather conservative choice. This setting was motivated by decision to stay within the 100 mV  
12 input range of the transient digitizer (Sect. 4.5).

13 We ascribe this unprecedented performance due to the mesh layers of the dynode stages that likely to act as  
14 electrostatic kinetic energy filters for the electrons. A pulse-height spectrum of one of the PMTs for the  
15 recommended operating voltage of 800 V is shown in Fig. 11. This spectrum was derived from a time scan with  
16 a 1-GHz digital oscilloscope (Tektronix, DPO 7104). No rise in photon counts towards 0 V pulse height is seen  
17 that would indicate signal-induced cathode emission, this result being limited by the chosen trigger level of the  
18 scope of  $-1.5$  mV. It is important to mention that the pulse-height distribution does not end at  $-23$  mV. As can  
19 be concluded from Figs. 9a and b much higher pulses exist that can reach almost  $-200$  mV. For one-hour  
20 measurements with our Raman lidar (Klanner et al., 2020) we did not observe dark counts in 7.5-m bins for  
21 discriminator thresholds of 4 mV and PMT supply voltages beyond 900 V.

22 In the far-field receiver we found that a high number of photons is more important than a high peak analogue  
23 voltage because the photon noise dominates the signal at large distances. Thus, we no longer attenuate the  
24 signals and irradiate the photocathode with all the light emerging from the spectrograph. For compensation we  
25 reduce the PMT voltage to about 700 V. Now, the 70 mV signal level corresponds to about 2.5 times more  
26 photons per time interval than before. This change has resulted in considerable lowering of the ozone noise for  
27 the 292 – 313-nm wavelength combination in recent years. Photon counting at 700 V and the resulting much  
28 lower single-photon amplitudes has not been tested so far (Sect. 4).

29 A really bad surprise was that the 7400 PMT is more than one order of magnitude more susceptible to daylight  
30 than the old modules. The H5783P-06 modules had stayed linear up to about 12 mV of constant-background  
31 analogue signal. Now, the constant signal background must be kept below 1 mV. This task has been demanding  
32 at 313 nm during the brightest part of the day, aggravated by the degraded surface of the primary mirror and in  
33 the presence of clouds. In spring and summer even signal undershoot to below the signal base line has been  
34 observed during the hours around noon. We added a 5.7-nm (f.w.h.m.) filter from Laseroptik was used for  
35 additional background blocking. Still, mathematical corrections had to be made, which were particularly  
36 important for optimum aerosol retrievals. A filter with a 0.5-nm flat top and very steep edges is needed.  
37 Additional solutions could be an additional light baffle above the telescope and replacing the aged primary  
38 mirror of the telescope.

39 **4.5 Transient Digitizers**

40 For the digitization of the analogue signal a 12-bit transient digitizer was found to be sufficient for avoiding the  
41 influence of single-bit steps since the shot-to-shot noise is larger than a least significant bit (LSB). This has

1 anticipated by numerical simulations with artificial noise before the 1994-1995 upgrading of the stationary  
2 system that demonstrated the absence of steps for a noise amplitude of 4 LSBs. A saw tooth generator built for  
3 randomizing the single-bit steps turned out to be unnecessary. By contrast, Langford (1995) reported a  
4 significant improvement in his system achieved by modulating the signal.

5 In the upgraded stationary system, the a 12-bit, 20 Hz system from DSP Technology was used until 2003. Since  
6 the mobile system was built one year later the first 12-bit, low-noise 20 Hz transient digitizers systems from  
7 Licel became available and was used. The performance was excellent with lower noise than in the DSP system.  
8 In 2013, the Licel transient digitizers were upgraded on our request by introducing custom-made ground-free  
9 input amplifiers. This latest version has led to an unprecedented performance with a relative noise level of about  
10  $\pm 1 \times 10^{-6}$  of the full 100 mV voltage range after minor smoothing (Sect. 7.1), yielding also highly sensitive  
11 aerosol measurements at 313 nm despite the short wavelength. This unprecedented performance has made  
12 possible to operate the system without photon counting with very little loss of quality.

13 Though being much noisier, the DSP Technology system was more linear than that of Licel as resolved down to  
14 a level of  $2 \times 10^{-5}$  of the full scale (Kreipl, 2006; Fig. 3.10: <http://www.trickl.de/PMT.PDF>). When firing the laser  
15 of our mobile aerosol lidar near-horizontally on to a rock at a distance of 9 km, where the peak equalled the  
16 signal maximum, the return from beyond the rock instantaneously and exactly returned to zero. By contrast, the  
17 Licel system yields small undershoot for distances beyond remote clouds, larger for larger signal areas. Of  
18 course, the performance is perfect in the absence of clouds that generate very pronounced spikes. The  
19 performance of the most recent version of the Licel system is discussed further in Sect. 7.1.

## 20 **4.6 Pre-amplifiers**

21 In order to lift the PMT output, typically around 10 mV for the old PMTs and 70 mV for those from Hamamatsu  
22 (into  $50 \Omega$ ), to the coarsest range of the transient digitizers adjustable-gain pre-amplifiers were used until 2011  
23 (Analog Modules, model 351, bandwidth 4 MHz, gain adjustable between 1 and 10). In two of the far-field  
24 channels (“on” wavelengths”) these pre-amplifiers produced some very small small ringing. Between 1997 and  
25 2003 these problems were overcome by using photon-counting data. For many years of exclusively using  
26 analogue data the ringing had to be removed by mathematical corrections. The ringing and the additional noise  
27 finally completely disappeared after disconnecting the zero voltage. After introducing the latest (ground-free)  
28 version of the Licel input stage the preamplifiers were removed.

## 29 **4.7 Photon counting**

30 In the stationary ozone DIAL single-photon counting was applied between spring 1997 and 2003 with a FDC700  
31 1-GHz photon-counting system from Optec. The signals were fully linear starting in the middle troposphere, but  
32 produced extra counts at lower altitudes, presumably due to pile-up effects of the PMT ringing (Fig. 9a). The  
33 signal for photon-counting was separated from the analogue output by an impedance-matched junction  
34 containing an adjustable discriminator custom made by RSV. In the first version the discriminator level could  
35 not be reduced to below 11 mV. This level had to be chosen to ensure linear performance and maximum signal  
36 (Fig. 11). The unit was upgraded several year ago for picosecond time resolution and discriminator levels down  
37 to 2 mV.

38 The new PMT units delivered by RSV are free of the ringing of the original Hamamatsu tubes (Sect. 4.4) and  
39 feature pulse widths of about 1.5 ns (Fig. 10). In order to benefit from this considerable time resolution we  
40 recently purchased MCS6 and MCS6A five-channel high-speed photon counting systems from Fast Comtec for

1 several of our lidar systems. The signals are scanned for selectable pulse edges at intervals of 100 ps which  
2 means a maximum count rate of about 5 GHz for equidistant picosecond pulses. For both reasons a highly linear  
3 photon-counting performance was achieved that is presented in detail in the parallel publication on our Raman  
4 lidar for water vapour and temperature (Klanner et al., 2020).

5 The simultaneous analogue and photon-counting measurements from a single PMT lead to a deterioration of the  
6 analogue signal with an artificial perturbation of the signal of the order of  $10^{-4}$  of the peak voltage. This could be  
7 reduced by one order of magnitude by adding an optocoupler to the trigger input of the counting system.  
8 However, the shape of the perturbation was somewhat complex and, thus, difficult to correct mathematically. In  
9 addition, we do not have experience with photon counting at the currently preferred PMT voltages around 700 V  
10 or less (see above). At this time the simultaneous application of photon counting is postponed until a better  
11 solution becomes available.

## 12 **4.8 System Control**

13 All connections between electronic components of the two DIAL systems ([Ingenieurbüro W. Funk](#)) are ground-  
14 free. The trigger pulse is derived from a photodiode and subsequently distributed into numerous output channels  
15 via optocouplers ([Ingenieurbüro W. Funk](#)). The supply voltages for the PMTS, preamplifiers and discriminators  
16 ([Ingenieurbüro W. Funk](#)) are generated implying high-quality DC-DC converters (TRACO POWER, models  
17 TYL 05-05S30 and TYL 05-15W05). They are transferred to the different devices in shielded cables. The shields  
18 of the cable leading to the PMTs are open on the side of the detectors. The supply voltage can be set by the lidar  
19 PC via an I<sup>2</sup>C bus, but this option has never been used in the stationary system because of the rather stable clean-  
20 air conditions at Garmisch-Partenkirchen. Also the opening and closing of flap in the roof was initiated via I<sup>2</sup>C  
21 bus.

22 Electromagnetic interference from outside (e.g., the laser) has been kept at a negligible level by using doubly  
23 shielded signal cables (Suhner, G03332; the outer shield is left open on one side) and ground-free circuits. The  
24 trigger pulses were obtained from photodiodes and then distributed via optocouplers.

25 The firing of the XeCl laser was initiated via RS232 remote control of the computer of the excimer laser. The  
26 power for the high-voltage circuits of the laser is supplied by a separate source. The laser PC was connected to  
27 to the clean power in the lidar laboratory. The laser itself is controlled by its computer via optical fibres. Finally,  
28 both cables connecting the lidar laboratory and the laser PC are shielded which successfully removed any  
29 interference from the high-voltage pulses (Eisele and Trickl, 1997).

## 30 **4.9 Automatic Operation**

31 Both DIAL systems have been extensively operated under automatic control by the lidar PC. In the mobile  
32 system an external start and warm-up of the laser was not possible due to issues in the programs delivered by  
33 Continuum. The laser output was continuously controlled: The measurements were interrupted if the 1064-nm  
34 and 266-nm power levels were below maximum.

35 Among the various error conditions the most important ones are rain or high wind speed. This results in  
36 immediate closing the flap in the roof. As to the KrF laser the high-voltage is shut down, and as to the Nd:YAG  
37 laser the output shutter is closed the laser continuing to fire in order to maintain thermal equilibrium of the  
38 frequency doubling crystals.

1 Time series under automatic control have been extended for the stationary system to up to four days. In this was,  
2 numerous atmospheric transport studies could be made, the first four-day series leading to the first detection of  
3 North American ozone over Europe (Eisele et al., 1999; Trickl et al., 2003).

4 **5. Data Processing**

5 The number density of ozone,  $n_{O_3}$ , is obtained by computing the DIAL equation

6 
$$n_{O_3}(r) = -\frac{1}{2\Delta\sigma} \frac{d}{dr} \ln \frac{P(\lambda_1, r)}{P(\lambda_2, r)} + \frac{1}{2\Delta\sigma} \frac{d}{dr} \ln \frac{\beta(\lambda_1, r)}{\beta(\lambda_2, r)} - \frac{1}{\Delta\sigma} (\alpha_r(\lambda_1, r) - \alpha_r(\lambda_2, r)) \quad (1)$$

7 with the difference

8 
$$\Delta\sigma = \sigma_{O_3}(\lambda_1) - \sigma_{O_3}(\lambda_2)$$

9 of the absorption cross sections of ozone.  $P$  is the power returning from the atmosphere ("lidar signal"),  $\beta$  the  
10 total backscatter coefficient and  $\alpha_r$  the residual extinction coefficient that includes Rayleigh and particle  
11 scattering as well as absorption by molecules other than ozone. In the absence of aerosols and interfering gas Eq.  
12 1 reduces to:

13 
$$n_{O_3}(r) = -\frac{1}{\Delta\sigma} \left( \frac{1}{2} \frac{d}{dr} \ln \left( \frac{P(\lambda_1, r)}{P(\lambda_2, r)} \right) + (\alpha_r(\lambda_1, r) - \alpha_r(\lambda_2, r)) \right), \quad (2)$$

14 the subscript R denoting "Rayleigh". The Rayleigh extinction coefficients can be calculated in the ultraviolet  
15 spectral region with relative uncertainties less than 1 % if radiosonde data are used for deriving the atmospheric  
16 density. For short "on" wavelengths (266 nm, 277 nm) the absorption of the radiation by ozone dominates the  
17 extinction coefficients and, thus, the uncertainty due to the Rayleigh term is, therefore, negligible.

18 Under the clean-air conditions prevailing at Garmisch-Partenkirchen Eq. 2 is mostly a reasonable approximation.  
19 However, occasionally aerosol corrections must be made. Due to the large wavelength separation in UV ozone  
20 DIALs the inference by aerosols may contribute more seriously than in DIAL systems measuring species with a  
21 well-resolved line structure allowing the use of neighbouring wavelengths. Operational procedures based on  
22 iterative parameter search were developed that are in detail described in our preceding publication (Eisele and  
23 Trickl, 2005). For calculating ozone in the presence of structured aerosol distributions the lowest errors have  
24 been obtained for the wavelength pair 277 nm – 292 nm, followed by 277 nm – 313 nm and 292 nm – 313 nm.  
25 The most important factor is a strong absorption cross section of ozone, and then a minimum (but finite)  
26 wavelength difference (Völger et al., 1996; Eisele and Trickl, 2005), in contrast to a frequently heard, but  
27 obviously wrong opinion.

28 Our numerical approach was significantly modified with respect to that published earlier (Kempfer et al., 1994).  
29 Previously, the derivatives in the DIAL equation were calculated by fitting third-order polynomials to the  
30 backscatter profiles within a given evaluation interval. This method worked rather well, but was slow. A faster  
31 modified approach resulted in small steps in the generated ozone profiles requiring to apply some moderate data  
32 smoothing in addition (Kempfer et al., 1994).

33 From the point of view of numerical filter theory polynomials are not ideal because their transfer functions  
34 expose ringing. We decided to calculate the derivative with a simple linear least-squares fit of just a short  
35 interval keeping the vertical resolution (see further below) at about 50 m, followed by optimized numerical  
36 filtering. A ~~four~~<sup>five</sup>-step algorithm is applied, consisting of

1 (1) data pre-smoothing at a level roughly corresponding to the chosen minimum vertical resolution of 50 m  
 2 (important for smooth aerosol retrievals for the near-field telescope),  
 3 (2) calculation of the derivative with a constant number of data points in a sliding interval,  
 4 (3) range-dependent data smoothing with a vertical resolution of about 50 m at low altitudes and 250 m to 500  
 5 m in the tropopause region, depending on the noise level of the respective measurement,  
 6 (4) truncation of the uppermost ozone profiles is truncated at an altitude below the onset of diverging noise, in  
 7 summer sometimes even below the tropopause,  
 8 (5) final minor smoothing of the composite ozone profile put together from the best segments of the partial  
 9 ozone profiles from different wavelength combinations and the two telescopes.

10 The smoothing intervals in step 3 have been mostly minimized in order not to suppress existing ozone structures.

11 For a linear fit and equidistant data points the result of the fits may be expressed in a rather simple formula,  
 12 resulting in the following solution of the DIAL equation for the  $i^{\text{th}}$  data point (Vogelmann and Trickl, 2008).  
 13 Selecting a fit interval between data point  $i - k$  and  $i + k$  one obtains

$$14 \quad 15 \quad \frac{d}{dr} \ln q_i \approx \frac{3}{\langle q_i \rangle \Delta r} \frac{\sum_{j=i-k}^{i+k} (j-i) q_j}{k(k+1)(2k+1)} , \quad (3)$$

16 with the signal ratio

$$17 \quad q_i = \frac{P(\lambda_{\text{on}}, r_i)}{P(\lambda_{\text{off}}, r_i)} \text{ and } \langle q_i \rangle = \frac{\sum_{j=i-k}^{i+k} q_j}{2k+1} ,$$

18  $\Delta r$  being the size of the range bin of the transient digitizer or photon-counting system. Application of Eq. 3  
 19 allows a fast computation of the derivative, in particular for constant  $k$ , when only the sum in the numerator must  
 20 be calculated for each step. In Eq. 3  $\langle q_i \rangle$  is written instead of  $q_i$  as by Vogelmann and Trickl (2008). This is  
 21 explained further below.

22 Another important advantage of Eq. 3 is that the least-squares fit is not applied to the logarithm, but to the signal  
 23 ratio itself, due to the transformation

$$24 \quad \frac{d}{dr} \ln q_i = q_i^{-1} \frac{d}{dr} q_i .$$

25 In contrast to the noise of the logarithm of  $q_i$  the noise of the signal ratio is symmetrical and fulfills a key  
 26 prerequisite of least-squares fitting. A negative density ozone bias is, therefore, avoided.

27 However, the application of Eq. 3 has limitations. Its application to simulated lidar profiles revealed that there  
 28 are numerical biases with growing interval sizes  $2k$ . This is further discussed below.

29 The linear approach in Eq. 3 is reasonable for interval sizes  $L = 2k \Delta r$  not exceeding a scale representing the  
 30 ozone distribution. Eq. 3 is reasonable choice for data smoothing, but it is not a perfect frequency filter and  
 31 transmits residual high-frequency noise. Therefore, we have used a combination of Eq. 3 in a limited interval and  
 32 numerical low-pass filtering.

33 Numerical low-pass filtering of data points  $y_i$  is based on the general equation (Eisele, 1997; and references  
 34 therein)

$$y'_i = \sum_{j=i-k}^{i+k} a_j y_{i-j}$$

1 , (4)

2 with the smoothed value  $y'_i$  and the coefficients

3 
$$a_j = a_{-j} = N \frac{\sin(2\pi j f_c f_s^{-1})}{j\pi} ;$$

4  $f_c$  and  $f_s$  being the cut-off and sampling frequencies, respectively, and  $N$  a normalization factor. The interval  
5 width is  $L = 2 k \Delta r = 2 k c f_s^{-1}$ . One general problem with numerical low-pass filtering is the occurrence of  
6 ringing. This can be minimized by introducing window functions  $w_j$

7 
$$y'_i = \sum_{j=-k}^k a_j w_j y_{i-j} . \quad (5)$$

8 After comparing several listed window functions a Blackman-type window (Blackman and Tukey, 1959) was  
9 chosen:

10 
$$w_j = 0.42 + 0.50 \cos\left(\pi \frac{j}{k}\right) + 0.08 \cos\left(2\pi \frac{j}{k}\right). \quad (6)$$

11 The best performance was achieved by selecting

12 
$$f_c = \frac{f_s}{2 k} = \frac{c}{2 k \Delta r} , \quad (7)$$

13  $c$  being the speed of light. The response function obtained for applying Eqs. 5 – 7 with  $k = 25$  is depicted in Fig.  
14 12 together with that for a sliding arithmetic mean over  $2 k + 1 = 51$  symmetrically arranged data points. A  
15 linear least-squares fit is equivalent to the arithmetic mean. These linear operations, though suitable for  
16 smoothing, are not perfect frequency filters and, therefore, transmit residual high-frequency noise. More details  
17 on the frequency transfer functions for some filters are given by Eisele (1997), and, more recently, by Iarlori et  
18 al. (2015) and Leblanc et al. (2016).

19 The vertical resolution can be defined in a number of ways (Iarlori, 2015; Leblanc, 2016). For practical reasons  
20 the German Engineering Society (Verein Deutscher Ingenieure, VDI, 1999) introduced a definition of the range  
21 resolution as the the interval between 25 % and 75 % of the rise of the response to a Heaviside step (Fig. 12).  
22 Here, the response reaches a signal level of 100 % at large distances from the step. Since the VDI guideline was  
23 published we have preferred to apply this definition. In spectroscopy, mostly a response to a delta peak and its  
24 full width at half maximum is used to define spectral resolution. As we can see in Fig. 12 without normalization  
25 the delta response is much smaller than the original one, which looks strange in practise.

26 From Fig. 12 we derive for the Blackman filter a VDI vertical resolution of 19.2 % of the full filtering interval  $L$ .  
27 The response of the Blackman filter to a single-channel (“delta”) peak ( $5 \times 10^{17} \text{ m}^{-3}$  to  $1 \times 10^{18} \text{ m}^{-3}$ ) was found to  
28 exhibit a full width at half maximum of 34.3 % of  $L$  (Fig. 12). This fraction looks surprisingly large in  
29 comparison with the step response. The fractions for the pure Blackman filter (Eqs. 5, 6) are also valid for much  
30 smaller smoothing intervals [than in this example](#).

31 We also give in Fig. 3 an example for numerical differentiation of a simulated lidar measurement based on Eq. 3.  
32 The DIAL equation was synthesised for the wavelength pair 277 – 313 nm, based on the artificial ozone density  
33 step between bins 999 and 1000 and on an air density profile calculated from the U.S. Standard Atmosphere  
34 (1976). The absence of particles and absorbing molecules other than ozone was assumed. The application of Eq.

1 3 yields a similar step (Fig. 3) that matches that for the Blackman filter within most of the rise if one selects  $k =$   
 2 27. In contrast to an ideal filter the derivative filter transmits some residual noise. The VDI vertical resolution is  
 3 about 45 % of the filtering interval ( $k = 10$  to 30, presumably in a wider  $k$  range).  
 4 It is important to note that due to the curvature of the backscatter profiles Eq. 3 yields a bias that is absent in the  
 5 case of missing Rayleigh scattering. This bias grows with  $k$ , and is negative for Eq. 3 (for  $k = 27$ :  $-0.0050 \times 10^{17}$   
 6  $\text{m}^{-3}$  ( $-0.10\%$ ) ahead the step and  $-0.0033 \times 10^{18} \text{ m}^{-3}$  ( $-0.33\%$ ) behind it). This bias is small, and it becomes  
 7 even negligible for, e.g.,  $k = 10$  (and less). However, it grows with  $k$ . Thus, it is reasonable to use moderate  
 8 values of  $k$  for the derivative and subsequent numerical filtering with Eqs. 5 and 6 to remove the residual noise.  
 9 Finally, the use of  $q_i$  instead on  $\langle q_i \rangle$  in the denominator of Eq. 3 yields a positive bias larger than the negative  
 10 one for using Eq. 3. This justifies the choice of  $\langle q_i \rangle$ . One could think about an empirical mathematical  
 11 correction interpolating between  $q_i$  and  $\langle q_i \rangle$ .  
 12 The filter interval for the smoothing is dynamically enhanced with height applying a linear relation for simplicity  
 13 (a quadratic dependence might be better). The coefficients  $c_1, c_2$  are pre-selected for each wavelength pair,  
 14  $k = c_1 + c_2 * i$  for bin  $i$ .  
 15 For example, for the large telescope of the stationary lidar  $c_1 = 0, c_2 = 0.125$  for the pair 277 – 313 nm,  $c_1 = 0, c_2$   
 16 = 0.156 for 292 – 313 nm. This results in filtering intervals  $2k$  of the order of 250 and 500 near the upper end of  
 17 the respective useful range (VDI vertical resolutions of 360 m and 720 m, respectively). These preset  
 18 coefficients are used for the initially automatically produced set of quick-look profiles, but are afterwards  
 19 reduced in size in some subranges if allowed by the noise level. In ranges with clearly distinguishable ozone  
 20 gradients (e.g., stratospheric intrusion peaks or tropopause) or strong narrow features the vertical resolution is  
 21 also reduced as far as reasonable. In particularly noisy subranges in the upper troposphere sometimes  
 22 homogeneously distributed ozone is fitted to the corresponding density segments. The different segments are  
 23 pasted into the actual overall ozone profile.  
 24 As a consequence of this complexity, a solution for automatically deriving uncertainties for all partial data  
 25 segments has been postponed. In the early 1990s uncertainties for the much less sophisticated evaluation  
 26 procedure had been calculated from the least-squared fitting approach applied (Kempfer, 1992).  
 27 The calculation of mixing ratios and the retrieval of aerosol backscatter coefficients require the knowledge of the  
 28 atmospheric density. Within the troposphere this is not extremely important and simple annual average density  
 29 profiles do not contribute more than a few per cent to uncertainty (Carnuth et al., 2002). However, with growing  
 30 data quality and a range reaching the stratosphere the incorporation of a better density profile became mandatory.  
 31 This is achieved by importing the radiosonde data for the nearest-by station of the German Weather Service,  
 32 Munich or Stuttgart, from the University of Wyoming data base (<http://weather.uwyo.edu/upperair/sounding.html>).  
 33 313-nm aerosols backscatter coefficients have been routinely calculated for each measurement since 2007 based  
 34 on the methods mentioned above (Eisele and Trickl, 2005). They are publically available for all years starting in  
 35 2007 from the EARLINET data base (<https://data.earlinet.org/>).  
 36 The quality of the aerosol backscatter coefficients for the latest period of lidar operation has been extremely high  
 37 during most of the day, as can be seen in (Trickl et al., 2015) and in Sect. 7.1. This has served as an additional  
 38 quality criterion for the ozone retrieval, together with the comparison of the DIAL profiles for different  
 39 wavelength combinations and the single-wavelength ozone retrieval for 292 nm. In absence of aerosol this single  
 40 channel is extremely reliable and, in summer, less noisy than the DIAL solution for 292 – 313 nm. However, the  
 41 Rayleigh backscatter coefficients must be calculated from radiosonde data in order to achieve good quality.

1 After the introduction of the 7400 PMTs, a slight correction of the far-field 313-nm profiles became necessary  
2 during the hours around noon (Sect. 4.4). The overshoot of the normally negative signal is particularly  
3 pronounced in summer due to the PMT overload effects in the presence of a daylight background exceeding 1  
4 mV. Aerosol retrievals mostly perfect during night-time; just a constant displacement of the order of  $10^{-7} \text{ m}^{-1}$   
5  $\text{sr}^{-1}$  must be corrected. As the 313-nm PMT starts to exhibit overshoot for large distances a mathematical  
6 correction becomes necessary, in summer even before 10 CET. In the absence of [UTLS](#)-aerosol [in the upper](#)  
7 [troposphere and the lower stratosphere](#) the corrections can be nicely verified by comparing the DIAL ozone with  
8 the 292-nm single-signal ozone retrieval.  
9

## 10 **6. System Validation and Measurements**

### 11 **6.1 Calibration**

12 Since the first measurement series in 1991 the ozone data have been calibrated by using the absorption cross  
13 sections from the University of Reims (Daumont et al., 1992; Malicet et al., 1995). The motivation for this is  
14 described Kempfer et al. (1994). Most importantly, the measurements account for the decomposition of ozone  
15 during the absorption measurements by precise pressure measurements. The cross sections have measured again  
16 and again (e.g., Gorshelev et al., 2014; Serdyuchenko et al., 2014; and references therein), but no improvement  
17 has been achieved, except for, perhaps, the temperature dependence. Very recently, four new cross sections  
18 measured between 244 nm and 254 nm at an uncertainty level of 0.1 % have been provided by Viallon et al.  
19 (2015). In view of the choice for our ozone DIALs it is extremely satisfactory that the agreement with the  
20 corresponding values in the Reims data is within  $\pm 0.06 \text{ %}$ .  
21 The temperature dependence as a function of altitude is obtained by interpolation of the cross sections from  
22 Reims measured for different temperatures.

### 23 **6.2 Validation**

24 For the convenience of data users, the system performance is summarized in Table 4 for the different periods of  
25 operation. The uncertainties have been derived from validation exercises, sensitivity studies in low-signal ranges  
26 and noise estimates and reproducibility of the ozone densities during diurnal series of measurements.  
27 The lidar system has been systematically validated ([since 2007 on each sounding day](#)) by using the in-situ data  
28 from the nearby mountain stations Wank (1780 m a.s.l.) and Zugspitze (2962 m a.s.l.) until the measurements at  
29 these sites were discontinued (evaluated data are available until 2010). Afterwards, the ozone values of the  
30 Schneefernerhaus (UFS) Global Atmosphere Watch station have been used for occasional comparisons (Trickl et  
31 al., 2014; 2020). UFS is located in the southern face of Zugspitze, at a distance of 9 km from the ozone DIAL at  
32 IFU. The gas inlet is at 2670 m. The average ozone mixing ratios are about 1 % lower than those at the summit  
33 (Ludwig Ries, personal communication). The lidar data agree similarly well with those from UFS as previously  
34 with the Zugspitze ozone.  
35 In addition, a large number of successful comparisons have been made with the Hohenpeissenberg ozone sondes  
36 (distance: 38 km), a few examples were given by Eisele et al. (1999). A more extensive comparison is planned  
37 for the 2018 data, accompanied by a highly successful comparison with a sonde launched by colleagues from  
38 Jülich directly at IMK-IFU in February 2019. The latter side-by-side comparison for mixing ratios of about 50  
39 ppb yielded a rather constant, bias of the sonde of 2 to 3 ppb up to 7 km and, above this, a slightly higher  
40 variability of the differences.

1 These comparisons have certain limitations. In the case of the Hohenpeißenberg sondes the air-mass difference  
2 matters in certain altitude ranges due to a 48 km distance between both stations. Under comparable conditions  
3 the differences between the profiles have been between 5 and 10 %.  
4 The lidar has shown a slightly positive bias with respect to the Wank site, mostly not exceeding 5 ppb. This bias  
5 is not present during night-time, but mostly forms in the morning under warm conditions. It has, therefore, been  
6 ascribed mostly to slope winds (Carnuth and Trickl, 2000, Fig. 5) venting morning-type low-ozone air from the  
7 valley up this rather isolated summit that acts like a chimney. Frequently the summer-time morning values agree  
8 better with the 5:00 CET measurement than with the Wank mixing ratio for the true data-acquisition time. Until  
9 2011 some alignment issues could occasionally exist that enhanced the uncertainty for distances below 0.5 km.  
10 The Wank site has been invaluable for verifying good alignment of the near-field telescope, until 2011 resulting  
11 in problems.  
12 The comparisons with the Zugspitze in-situ data have been mostly very convenient. The differences of the  
13 mixing ratio have rarely exceeded 2 ppb, exceptions typically occurring if there is a pronounced ozone gradient  
14 around 3000 m. In absence of an extended comparison since 2012 an example from a four-day series in May  
15 (Trickl et al., 2003; 2011) is shown in Fig. 13 that exhibits more noise than recent comparison. The data are  
16 compared for two lidar altitudes, 2970 m and 2786 m. The lower altitude accounts for the air-mass rise during  
17 the final approach towards the high mountain. The results for 2970 m show a few positive departures that results  
18 in a positive average difference between lidar and station of 0.82 ppb (standard deviation: 2.15 ppb). For the  
19 lower altitude the “bias” is just 0.34 ppb (standard deviation: 1.61 ppb). These values are all small in comparison  
20 with the average Zugspitze mixing ratio, but its sign agrees with the expectation for the 1.8-% bias of the in-situ  
21 measurements obtained in the recent cross-section study by Viallon et al. (2015).

22 ~~During the period 2007–2010 daily comparisons with the data from the mountain sites were made. The~~  
23 ~~deviations rarely exceeded 2 ppb with respect to the Zugspitze ozone.~~

24 The performance of the mobile system is discussed in Sect. 5.5.

### 25 **6.3 Interference by Other Gases**

26 Important species absorbing in the typical wavelength range of ozone DIAL systems are SO<sub>2</sub>, NO<sub>2</sub> and some  
27 hydrocarbons. Under the clean-air conditions prevailing at the Alpine site Garmisch-Partenkirchen and in the  
28 free troposphere spectral interference from these constituents should be very rare. As mentioned, for the mobile  
29 DIAL retrievals for the wavelength pair 266 – 299 nm are almost insensitive with respect to SO<sub>2</sub> and NO<sub>2</sub>.  
30 Oxygen must be also considered in the wavelength region below 285.66 nm (Krupenie, 1972; Jeunouvier et al,  
31 1999). The absorption cross sections of O<sub>2</sub> in this region (Herzberg bands) are rather low, but absorption cannot  
32 be completely neglected due to the high concentration of this molecule. We found some approximate  
33 coincidences with not relevant high rotational levels, and an approximate coincidence of the 277.11 nm emission  
34 with J = 5–7 components of the extremely weak A' → X (2,0) band. 266.12 nm is slightly outside a group of O<sub>2</sub>  
35 lines. In summary, absorption of the emissions used in the two DIAL systems in oxygen can be neglected, in  
36 agreement with the good validation results.

### 37 **7. Measurements**

#### 38 **7.1 Examples for the Stationary System**

39 After the first upgrading of the stationary DIAL in 1994 and 1995 the system yielded a greatly improved  
40 sensitivity and a much larger vertical range up to about 15 km due to the tree-wavelength operation. The number

1 of measurements per year grew and time series under automatic control were extended up to four days, the first  
2 four-day series being the well-documented one in May 1996 published by Eisele et al. (1999), [Stohl et al. \(2000\)](#),  
3 Cristofanelli et al. (2003) and Trickl et al. (2003). However, until 2003 the operation was limited to funded  
4 projects and focussed research topics. After the second major system upgrading routine measurements were  
5 started in 2007. Almost 5000 ozone profiles were obtained from 1991 to February 2019, numerous examples can  
6 be found in our publications (see Appendix, the most recent one, on the period 2007 to 2016, being (Trickl et al.,  
7 2020)).

8 A summary of the work done is given in Table 3. Uncertainties estimated for the different periods and altitude  
9 ranges are specified in Table 4 as a guide for potential data users.

10 Figure 14 shows the raw backscatter signals (a) uncorrected and (b) with automatic exponential correction. The  
11 amplitudes of the corrections grow with the area of the backscatter signal that is larger for the far-field telescope  
12 than for the near-field telescope and grows with the wavelength due to the decreasing absorption cross section.  
13 In the range where such an exponential wing affects the lidar signal it does not exceed a few times  $10^{-5}$  of the  
14 input voltage range (100 mV). The slightly enhanced noise in channel 6 (313 nm, red curve) is caused by the  
15 early-morning daylight roughly one hour after sun rise.

16 The introduction of three-wavelength operation made possible an internal quality assurance. Ozone profiles are  
17 derived from different wavelength combinations. The observation of mutual deviations in the retrieved densities  
18 results in immediate re-examination of the alignment. As mentioned just two misalignments matter: the overlap  
19 of the partial beams emerging from the Raman shifters after recombination and the pointing of the beam emitted  
20 into the atmosphere. Minor discrepancies for 292 – 313 nm due to alignment drifts during extended periods of  
21 unattended operation can be conveniently recalibrated by using the 277 – 313-nm profiles as a reference, which  
22 was routinely done in recent years. As mentioned the 277-nm channel of the large telescope was found to be  
23 insensitive to slight misalignments presumably due to the particularly small focal point in the entrance slit of the  
24 spectrograph. In addition, small drifts in laser pointing are do not result in a transverse displacement of the spot  
25 on the detectors that are placed in the image planes of the principal mirror of the telescope.

26 One example for a measurement for a perfectly aligned lidar is shown in Fig. 15 (26 October 2015). The figure  
27 contains three ozone profiles from both receivers. The three ozone profiles match well in their common overlap  
28 regions. Nevertheless, due to low ozone the near-field signal (here 277 – 313 nm) yields reasonable ozone values  
29 up to 2.5 km above the ground (740 m a.s.l.). The range for same wavelength pair in the large receiver extends  
30 up to 6.5 km a.s.l., with moderately elevated ozone. The simultaneously measured ozone value at UFS is lower  
31 by just 0.7 ppb. The 292 – 313-nm ozone profile exhibits less structure than that for 277 – 313 nm. The  
32 absorption cross section for 292 nm is less than one quarter of that for 277 nm, which necessitates smoothing the  
33 292 – 313-nm ozone over larger intervals (Sect. 5). In the uppermost part of the red curve a 292-nm single-  
34 wavelength retrieval was applied that reduces the noise inferred by the 313-nm profile, but otherwise agrees with  
35 the DIAL solution. Such a retrieval is not possible in the presence of aerosol or clouds.

36 The ozone hump between 3.0 and 4.7 km is caused by a very dry layer (1 % minimum relative humidity at 4.2  
37 km for the Munich radiosonde (100 km roughly to the north; 1% is an artificial cut-off in the listings for the  
38 RS92 radiosonde (Trickl et al., 2014)). 315-h backward trajectories calculated with the HYSPLIT model  
39 (Draxler and Hess, 1998; [http://ready.arl.noaa.gov/HYSPLIT\\_traj.php](http://ready.arl.noaa.gov/HYSPLIT_traj.php)), selecting re-analysis meteorological  
40 data, suggest a long-range descent from the stratosphere over western Canada. The Munich thermal tropopause  
41 for both standard launch times is significantly higher than the onset of the ozone rise. It is well known, also from

1 our measurements, that the thermal tropopause does not perfectly coincide with the onset of the ozone rise  
2 (Hoerling et al., 1991; Pan et al., 2004).

3 In general, as pointed out in Sect. 4.2, the near-field receiver yields reasonable ozone typically up to at least 2  
4 km above the ground (2.74 km a.s.l.). The quality is limited due to the rapid drop of the backscatter signal. The  
5 useful range for 277 nm of the far-field receiver is 6.5 to 8 km in winter (40 to 50 ppb). 292 nm is rarely used in  
6 the lower troposphere because of the lower sensitivity for ozone and the stronger sensitivity to aerosol (Eisele  
7 and Trickl, 2005). However, the 277 – 292-nm profiles are preferred the presence of pronounced aerosol  
8 structures because of a less critical aerosol correction. The typical range for 292 nm is roughly 3 km above the  
9 tropopause, which can vary with the slope of ozone rise. In summer, when ozone in the free troposphere can  
10 exceed 100 ppb, sometimes the range is limited to 10 to 11 km and the seasonally higher tropopause is not  
11 reached due to the strong loss of radiation.

12 Due to the short measurement time of just 41 s the reproducibility of the data can be easily verified. In Figure 16  
13 we show the profiles for three measurements under complex conditions (Saharan dust up to 4 km and a  
14 stratospheric air intrusion around 5.7 km) obtained within less than three minutes on 18 June 2013. The intrusion  
15 originated at 10 km or more over the United States ~~roughly at least~~ 13 days backward in time (Trickl et al., 2020).  
16 The layer descended to southern Spain and then turned north-eastward towards the Alps, slightly rising. Due to  
17 the long travel the minimum relative humidity was as high as 6 %, as measured by both our water-vapour DIAL  
18 and the Munich radiosonde (Trickl et al., 2020).

19 Due to elevated ozone mixing ratios (50 to 80 ppb) the radiation loss results in an increase of the short-term  
20 variability of the ozone profiles in the upper troposphere which indicates a level of uncertainty of about  $\pm 10$  ppb.  
21 The noise of the 277-313-nm ozone values strongly increases above 5.5 km, where the data from the 292-313-  
22 nm pair are used.

23 With the latest PMT version (2012) the far-field performance of the lidar during the warm season decreases  
24 around noon due to the growing daylight background at 313 nm and the resulting nonlinearity. The 313-nm  
25 constant background is largest in the presence of clouds. The signal must be corrected mathematically (Sect. 5)  
26 to achieve both a quantitative ozone profile and a reasonable aerosol retrieval with zero aerosol in clean parts of  
27 the atmosphere. The DIAL result based on the corrected 313-nm data is then also compared with the 292-nm  
28 single-trace ozone retrieval and usually agrees well. These comparisons demonstrate the value of simultaneously  
29 evaluating aerosol and  $O_3$ . For the strongest ozone mixing ratios (exceeding 100 ppb in the middle and upper  
30 troposphere) the range of the system may be limited to about 10 km and the stratospheric ozone rise is missed.

31 The best results are achieved in winter due to low ozone and low solar background. In Fig. 18 we give as an  
32 example the measurements on 13 February 2014. The measurements were limited to the morning hours due to  
33 the arrival of clouds ahead of a cold front, just before 11:00 CET. The profiles coincide extremely well outside  
34 two dry layers (1 CET Munich radiosonde, 4 to 12 % and 6 % RH, respectively) in the lower free troposphere  
35 and above 6 km that might be associated with the slightly elevated ozone at 8:00 CET around 3.8 km and 6.1  
36 km, respectively. The tiny peak at 6.1 km at 8:35 CET does not significantly exceed the uncertainty level in that  
37 altitude range. However, in addition to the low RH around 1 CET the corresponding HYSPLIT trajectories  
38 indicate for both layers a descent over at least 13 d from high altitudes over the North Pacific, confirming the idea of  
39 stratospheric intrusions. Intrusions with just a low rise in ozone are not rare during the cold season (Trickl et al.,  
40 2020). They can be resolved at least in the range covered by the less noisy 277 – 313-nm wavelength pair.

41 In Fig. 19 examples of aerosol retrievals of ozone-corrected 313-nm backscatter profiles during the brightest  
42 period of the year are shown. A constant backscatter-to-extinction ratio of  $0.020 \text{ sr}^{-1}$  was applied. Backscatter

1 coefficients of  $(1-3) \times 10^{-6} \text{ m}^{-1} \text{ sr}^{-1}$  are typical of the warm season at this site unless there is a strong Saharan  
2 dust or fire event. Here, the air masses originate in Italy and eastern Europe. The top altitude of 5 km resembles  
3 that for Saharan dust (Jäger et al., 1988; Papayannis et al., 2008), but was caused by orographic lifting during a  
4 transport across the Alps almost parallel to the mountains. The free troposphere was free of aerosol on that day  
5 which allows one to visualize the low noise of the lidar, at least during the early hours. Aerosol data from  
6 ultraviolet channels are usually strongly influenced by the noise of the strong Rayleigh background.  
7 In the presence of strong aerosol in the PBL, such as in the case of smoke or pronounced Saharan dust, the  
8 signal-to-noise ratio is strongly attenuated. High-aerosol events prevail in summer which adds to lowering the  
9 upper-tropospheric performance of the system.  
10 Starting in late 2012, the aerosol backscatter coefficients have been archived in the EARLINET data base mostly  
11 with a delay of less than one day after the measurements.

## 12 **7.2 Examples for the Mobile System**

### 13 **29 April 1999**

14 The final performance of the mobile system was achieved shortly before its destruction in late May 1999 (Fig.  
15 19). It had turned out that a daylight signal background of more than 12 mV was present in the 299-nm channel  
16 which lead to signal distortion (Sect. 4.4). Due to inserting a 300 nm cut-off filter, bridging the gap to the 320  
17 nm edge of the Corion filter, the 299 nm channels became linear and the planned operating range of the DIAL of  
18 4 km could be reached. As mentioned, further range extension would be possible if a rotating attenuator could be  
19 used for 299 nm to get roughly equal maximum far-field returns for 289 nm and 299 nm. Below a distance  $r$  of  
20 2.7 km 266 – 299-nm pairs were taken.  
21 In the example of Fig. 19 the range could be extended to a distance  $r = 8.3$  km (9.0 km a.s.l.) by evaluating  
22 ozone from the much stronger (*less noisy*) 299-nm signal alone. A slight adjustment of that partial profile had to  
23 be made, based on the DIAL results for lower altitudes, which resulted in elevated uncertainties. As can be seen  
24 from the edges of the isolated structures smoothing over several hundred metres was applied here.  
25 The validation is based just on comparisons with the in-situ measurements at the three local stations operated by  
26 IFU. The small deviations from the 11:30 CET Wank and Zugspitze in-situ data also shown in the figure suggest  
27 an uncertainty of 2 ppb in this altitude range. For the higher altitudes a comparison is missing because the  
28 measurement was made on a Thursday, too early for the Friday morning Hohenpeißenberg ozone sonde ascent.  
29 As can be concluded from the rich structure of the ozone profile and the pronounced ozone changes in the in-situ  
30 data (we select for Fig. 19 the data for 5:00, 9:30, 11:30, 14:00, and 17:00 CET) the meteorological situation was  
31 complex. The situation was characterized prefrontal advection of North American air via Algeria at most  
32 altitudes, where the minimum altitude of about 1.5 km was reached. Up to  $r = 3.5$  km the ozone profile is  
33 difficult to interpret. The ozone peak between 2.5 and 3.0 km is not necessarily caused by a subsiding  
34 stratospheric air intrusion: The relative humidity (RH) at the Zugspitze summit rose from 38 % to 66 % until  
35 17:00 CET, when the Zugspitze ozone reached the mixing ratio of the 11:30 peak above the summit. Subsidence  
36 is not very likely under prefrontal conditions anyway (Trickl et al., 2020). Also contributions from Northern  
37 Italy could have been picked up.  
38 Above 3.5 km we clearly see a pronounced stratospheric intrusion layer. This view is supported by the very high  
39 peak ozone of 113 ppb, the minimum RH of 1 % in the 13:00-CET ascent of the Munich radiosonde and  
40 HYSPLIT backward trajectories. The HYSPLIT trajectories revealed descent over more than ten days from the  
41 north-western part of North America or beyond.

1 The low upper-tropospheric ozone values are in agreement with the calculated source region 2 km above the  
2 Pacific south of Hawaii. Directly above the remote Pacific almost zero ozone has been found (Kley et al., 1996),  
3 which justifies to assume 20-30 ppb 2 km above the surface.

4 **Milano field campaign**

5 The second example is chosen from the VOTALP II (Vertical Ozone Transport in the Alps) “Milano” field  
6 campaign in 1998, in a joint effort together with the PIPAPO (Pianura Padana Produzione di Ozono) air-quality  
7 campaign around Milano (Italy) (more details on the measurements: Trickl, 2010). The mobile ozone DIAL was  
8 operated at Barni (Provincia di Como) within the first mountain range of the Alps, about 40 km north of Milano  
9 between 1 and 5 June 1998. On the first four days a day-by-day increase of the afternoon peak ozone advected  
10 from the Milano metropolitan area to Barni by the daytime up-valley wind was observed. During each night the  
11 O<sub>3</sub> mixing ratio dropped to roughly 60 ppb due to the reversal of the orographic wind direction.

12 Figure 20 shows the situation for the day with the highest ozone values, 4 June. The behaviour of the ozone rise  
13 was surprisingly similar to that on the previous days, including the bimodal profile at 13:36 CET (Central  
14 European Time = UTC + 1 h). In the late afternoon 120 ppb of ozone were reached, exactly verified by side-by-  
15 side measurements with ozone sondes launched by a team from the Swiss Paul-Scherrer Institute. This high  
16 mixing ratio turned out to be the very limit for retaining an overlap between the near-field and the far-field 266-  
17 nm “on” detection channels for the chosen position of the far-field apertures (blades) and PMT settings. The  
18 comparison of the DIAL and the sonde measurements also indicates some air-mass lifting towards the main part  
19 of the lake since the boundary-layer height (defined here by elevated ozone) grew as the sonde drifted northward  
20 during its ascent. It is interesting to note that the 19:10-CET DIAL profile next to the ground would agree with  
21 the sonde profiles for some average position of the two sonde maxima.

22 **8. Discussion and Conclusions**

23 Differential-absorption lidar systems for trace-gas measurements have proved to be an invaluable tool for  
24 atmospheric studies (Trickl, 2010). Despite this fact the application of DIAL systems is rather limited, in  
25 particular combined approaches. Despite promising developments in Europe within TESLAS in the early 1990s  
26 no continental-scale ozone-lidar network could be established. Ozone measurements have been mostly limited to  
27 Haute Provence ([Gaudel et al., 2015; Tarasick et al., 2019](#)), Garmisch-Partenkirchen and Athens ([Kalobakas et al., 2012; Mytilinaios et al., 2018](#)). By contrast, the ozone-lidar network TolNET was implemented in North  
28 America (Newchurch et al., 2016).

29 America (Newchurch et al., 2016).  
30 At IMK-IFU (Garmisch-Partenkirchen, Germany) three DIAL systems have been developed since 1988, two for  
31 ozone and one for water vapour (Vogelmann and Trickl, 2008). The ozone systems have been used for a large  
32 number of focussed investigations until 2003 (e.g., Carnuth et al., 2002; Eisele et al., 1999; Stohl and Trickl,  
33 1999; Trickl, 2003; Trickl et al., 2003; 2010; 2011). The stationary ozone and water-vapour lidars, have been  
34 used for routine measurements since 2007 (e.g., Trickl et al., 2014; 2015; 2016; 2020). The measurements with  
35 the stationary ozone DIAL have yielded a total of almost 5000 evaluated ozone profiles since 1991. In the  
36 absence of interruptions in the measurement programme, the typical annual number of evaluated measurements  
37 has been of the order of 500 measurements. This number will grow with further growing reliability of the  
38 automatically produced quick-look ozone and 313-nm aerosol profiles, due to a diminishing requirement for  
39 manual optimization. Manual corrections are, still, required in the presence of high ozone levels, due to the  
40 residual daytime issues at 313 nm and in the presence of pronounced aerosol and cloud structures.

1 In the course of three decades of ozone-DIAL development at IMK-IFU we have gradually optimized the  
2 technology to a state where even small variations in tropospheric ozone can be sensed with a high level of  
3 credibility. A full restriction to analogue data acquisition is possible due to the large dynamic range of the 5600  
4 and 7400 Hamamatsu PMTs. Automatic operation was introduced in 1996 (for both systems) although it has  
5 been limited to clear weather situations. Thus, the largest effort has been spent for the data evaluation. The  
6 results of automatic data evaluation have rarely been directly adopted and careful manual corrections have been  
7 made. These corrections include the selection of the best partial profiles based on comparisons and optimizing  
8 the vertical resolution in relation to the changing signal-to-noise ratio or when zooming into interesting ozone  
9 features. As a consequence of the excellent data quality the full use of automatic data evaluation is now coming  
10 within reach at least under conditions of low to moderate aerosol.

11 The quality of the retrieved 313-nm aerosol backscatter coefficients almost matches that traditionally obtained in  
12 the green spectral region. Baseline corrections are needed during daytime due to signal distortions caused by the  
13 high daylight sensitivity of the 7400 PMTs. Spectral filtering must be improved. Perhaps one of the old 5400  
14 PMTs must return to the far-field 313-nm channel.

15 Quite a number of lessons have been learnt:

- 16 – Three-wavelength operation is mandatory: It provides a wide vertical range and internal quality assurance;  
17 the aerosol retrieval yields an additional quality control of the 313-nm backscatter profiles.
- 18 – Use of at least one short "on" wavelength below 280 nm is an important base for high accuracy and for a  
19 low to moderate level of interference by aerosols that can be readily corrected for. Even for 266 nm a range  
20 up to about  $r = 2.5$  km above the lidar was demonstrated.
- 21 – A short measurement time of 41 s was achieved with the stationary system whereas for the mobile system  
22 about 10 min were necessary. This longer signal accumulation is, in part, due to the slower repetition rate of  
23 15 Hz per wavelength for the longer wavelengths, in part also by the strong signal decay for 266 nm (30 Hz  
24 repetition rate) that necessitates longer averaging to achieve a reasonable signal-to-noise ratio at larger  
25 distances. For the stationary system, longer averaging (e.g., 5 min) will yield better results in the upper  
26 troposphere in summer. In principle, the free-tropospheric capability (i.e., without significant amounts of  
27 aerosol) can be driven close to the uncertainty limit set by the absorption cross sections.
- 28 – Current-day transient digitizers make single-photon counting in an ozone DIAL almost superfluous, except  
29 for very long measurements in dark environment.
- 30 – Simultaneous analogue and PC counting out of a single PMT is possible, but has so far led to a deterioration  
31 of the analogue signal that cannot easily be corrected mathematically (see Klanner et al., 2020). Single-  
32 photon counting will be resumed if the residual signal distortions can be removed. However, an operation  
33 for low PMT supply voltages must be ensured to avoid signal attenuation and excessive averaging.
- 34 – The application of the small Hamamatsu PMTs has allowed the use of higher signal voltage levels (100 mV  
35 or more) than in the traditionally used photo tubes. A photon flux as high as possible should be applied in  
36 the far field channels since the signal noise is strongly influenced by the photon noise.<sup>21</sup> This is an issue if  
37 both analogue and photon counting out of the same PMT is chosen, because photon counting requires  
38 elevated supply voltages of the order of 800 V, too high for strong irradiation.
- 39 – A problem with the Hamamatsu 7400 PMTs not yet fully solved is the high sensitivity with respect to  
40 daylight: The background signal must not exceed 1 mV in order to avoid undershot, which can be  
41 minimized by higher laser pulse energy (improving the peak-signal-to-background ratio), careful spectral  
42 filtering, reducing the slit width at the polychromator entrance, adding another black baffles up to the roof

Irupdwlhukkrfkjhvwhoow

1 for the incoming radiation [just below the entrance flap in the roof](#) and a very clean surface of the primary  
2 mirror of the telescope. Also, for 313 nm, a return to a 5600 PMT can be considered in the far-field receiver.  
3 – The use of two spatially separated telescopes for near-field-far-field separation is superior to cutting off the  
4 near-field portions in the far-field channels as done in the mobile system (and the water-vapour DIAL  
5 (Vogelmann and Trickl, 2008)), unless a rotating signal attenuator is used for reducing the stronger “off”  
6 return.  
7 – An operational calculation of uncertainties is planned, an important requirement for archiving the data in  
8 international data bases.

9 [\\*In the case of the mobile lidar this would have required to enhance the 266-nm pulse energy of the Powerlite](#)  
10 [9030 laser to the full 120 mJ, or to use a larger receiver \(see first example in Sect. 7.2\).](#)

Irupdwlhut#fkjhvwhoow  
Irupdwlhut#fkjhvwhoow#2ijhvwhoow  
Irupdwlhut#fkjhvwhoow

## 12 **9 Data availability**

13 Data and information on the lidar systems can be obtained on request from the author of this paper  
14 (thomas.trickl@kit.edu., thomas@trickl.de after feb 2020). The 313-nm aerosol backscatter coefficients are  
15 archived in the EARLINET data base, accessible through the ACTRIS data portal <http://actris.nilu.no/>.

## 16 **10 Author statement**

17 TT carried out most lidar measurements after spring 1997, following U. Kempfer and H. Eisele, assisted by HG  
18 and MP. He led the technical development of both ozone DIAL systems since 1990. FN was responsible for the  
19 technical infrastructure of the mobile system. HG, MP and HV were involved in the system upgrading since  
20 2007.

## 21 **11 Competing interests**

22 The author declares that he has no conflict of interest.

## 23 **Appendix**

### 24 **Table A1: List of citations of atmospheric transport studies including ozone lidar systems**

25 Browell et al., 1987	Ancellet et al., 1991	Ancellet et al., 1994	Browell et al., 1996
26 Lamarque et al., 1996	Langford et al., 1996	Newell et al., 1997	Ravetta et al., 1999
27 Eisele et al., 1999	Stohl and Trickl, 1999	Grant et al., 2000	Baray et al., 2000
28 Seibert et al., 2000	Kowol-Santen and Ancellet, 2000	Browell et al., 2001	Carnuth et al., 2002
29 Zanis et al., 2003	Roelofs et al., 2003	Trickl et al., 2003	Galani et al., 2003
30 Papayannis et al., 2005	Leclair De Bellevue et al., 2006	Ravetta et al., 2007	Liang et al., 2007
31 Trickl et al., 2010	Trickl et al., 2011	Kuang et al., 2012	Trickl et al., 2014
32 Trickl et al., 2015	<a href="#">Ancellet et al., 2016</a>	Granados-Muñoz and Leblanc, 2016	
33 Sullivan et al., 2016	Kuang et al., 2017	Granados-Muñoz et al., 2017	Langford et al., 2018
34 Trickl et al., 2020			

Irupdwlhut#Ghxwvfkodqg,  
Irupdwlhut#Ghxwvfkodqg,

### 36 **Table A2: List of citations of some air-quality studies including ozone lidar systems**

37 Durieux et al., 1998	Fiorani et al., 1998	Zhao et al., 1998	Banta et al., 1998
38 Valente et al., 1998	Senff et al., 1998	Thomasson et al., 2002	Kourtidis et al., 2002

1 Duclaux et al., 2002 Couach et al., 2003 Dufour et al., 2005 Simeonov et al., 2005  
2 Langford et al., 2009 Senff et al., 2010 Trickl, 2010 Langford et al., 2012  
3 Dreessen et al., 2016 Langford et al., 2017 Sullivan et al., 2017 Yates et al., 2017

4

5 **Table A3: List of citations of papers describing ozone DIAL systems**

6 Grant et al., 1975 Browell, 1982 Pelon and Mégie, 1982 Browell et al., 1983  
7 Uchino et al., 1983 Ancellet, 1989 McDermid, 1991 Zhao et al., 1992  
8 Uthe and Livingston, 1992 Sunesson et al. 1994 Kempfer et al., 1994 Bucreev et al., 1994  
9 Bucreev et al., 1996 Grabbe et al., 1996 Reichardt et al., 1996 Eisele and Trickl, 1997  
10 Brenner et al., 1997 Ancellet and Ravetta, 1997 Wallinder et al., 1997 Proffitt and Langford, 1997  
11 Ancellet and Ravetta, 1998 Alvarez et al., 1998 Veselovskii and Barchunov, 1999  
12 Baray et al., 1999 Matthias, 2000 Lazzarotto et al., 2001 McDermid et al., 2002  
13 Fix et al., 2002 Nakazato et al., 2007 Machol et al., 2008 Burlakov et al., 2010  
14 Alvarez et al., 2011 Kuang et al., 2011 Kuang et al., 2013 Uchino et al., 2014  
15 Sullivan et al., 2014 De Young et al., 2017 Strawbridge et al., 2018 Fix et al., 2019

16 **Acknowledgements**

17 The author thanks Wolfgang Seiler and Hans Peter Schmid for their support over that many years. Walter  
18 Carnuth designed the first version of the stationary ozone DIAL that was built by Ulrich Kempfer and Raul Lotz.  
19 The decisive upgrading, that included a lot of new approaches, was achieved in co-operation with H. Eisele. The  
20 author is indebted to Werner Funk, Bernd Mielke, Heinz Josef Romanski and Bernhard Stein for numerous  
21 important discussions and technical improvements of the detection electronics. The valuable contributions during  
22 certain periods of the system development ~~and operation~~ by Pietro Brenner, Josef-Michael Burger, Bernd Jänker,  
23 ~~and~~ Karl Maurer ~~and~~ Matthias Perfaßl are emphasized. Hans-Eckhart Scheel, Ludwig Ries, Hans Claude, and  
24 Wolfgang Steinbrecht have provided reference ozone data for the Wank, Zugspitze and Schneefernerhaus  
25 mountain stations in the vicinity of IFU and ozone sonde data for the Hohenpeißenberg observatory of the  
26 German weather service. Johannes Keller provided the ozone sonde profiles of the team from the Swiss Paul-  
27 Scherrer-Institut for the Milano field campaign. The development of the mobile system was based on a highly  
28 efficient co-operation with the company OHB System (Bremen). The different steps of the lidar development  
29 have been funded by the German Ministry of Research and Technology (BMFT), the German Foundation for the  
30 Environment (DBU, two projects), and the Bavarian Ministry of Economics. Since 2007 the aerosol results have  
31 contributed to EARLINET (European Aerosol Research Lidar Network) that is currently a part of the European  
32 Research Infrastructure ACTRIS.

33 The service charges for this open access publication have been covered by a Research Centre of the Helmholtz  
34 Association.

35 **References**

36 ATMOFAST: Atmosphärischer Ferntransport und seine Auswirkungen auf die Spurengaskonzentrationen in der  
37 freien Troposphäre über Mitteleuropa (Atmospheric Long-range Transport and its Impact on the Trace-gas  
38 Composition of the Free Troposphere over Central Europe), Project Final Report, T. Trickl, co-ordinator, M.  
39 Kerschgens, A. Stohl, and T. Trickl, subproject co-ordinators, funded by the German Ministry of Education and  
40 Research within the programme “Atmosphärenforschung 2000“, Forschungszentrum Karlsruhe, IMK-IFU

1 (Garmisch-Partenkirchen, Germany), <http://www.trickl.de/ATMOFAST.htm>, 130 pp., 2005 (in German), with  
2 revised publication list 2012

3 Amodeo, A., Bösenberg, J., Ansmann, A., Balis, D., Böckmann, C., Chaikovsky, A., Comeron, A., Mitev, V.,  
4 Papayannis, A., Pappalardo, G., Perrone, M. R., Rizi, V., Simeonov, V., Sobolewski, P., Spinelli, N., Stoyanov,  
5 D. V., Trickl, T., and Wiegner, M.: EARLINET: the European Aerosol Lidar Network, *Optica Pura y Aplicada*,  
6 39, 1-10, 2006.

7 Ancellet, G., Papayannis, A., Pelon, J., and Mégie, G.: DIAL Tropospheric Ozone Measurement Using a  
8 Nd:YAG Laser and the Raman Shifting Technique, *J. Atmos. Oceanic Technol.*, 6, 832-839, 1989.

9 Ancellet, G., Pelon, J., Beekmann, M., Papayannis, A., and Mégie, G.: Ground-Based Lidar Studies of Ozone  
10 Exchanges Between the Stratosphere and the Troposphere, *J. Geophys. Res.*, 96, 22401-22421, 1991.

11 Ancellet, A., Beekmann, M., and Papayannis, A.: Impact of cutoff low development on downward transport of  
12 ozone in the troposphere, *J. Geophys. Res.*, 99, 3451-3468, 1994.

13 Ancellet, A., and Ravetta, F.: The Airborne Lidar for Tropospheric Ozone (ALTO), *Advances in Atmospheric*  
14 *Remote Sensing with Lidar, Selected Papers of the 18th International Laser Radar Conference, Berlin (Germany,*  
15 *1996)*, A. Ansmann, R. Neuber, P. Rairoux, U. Wandinger, Eds., Springer (Berlin, Heidelberg, New York), 399-  
16 402, 1997.

17 Ancellet, A., and Ravetta, F.: Compact airborne lidar for tropospheric ozone: description and field  
18 measurements, *Appl. Opt.*, 37, 5509-5521, 1998.

19 [Ancellet, G., Pelon, J., Totems, J., Chazette, P., Bazureau, A., Sicard, M., Di Iorio, T., Du Lac, F., and Mallet,](#)  
20 [M.: Long-range transport and mixing of aerosol sources during the 2013 North American biomass burning](#)  
21 [episode: analysis of multiple lidar observations in the western Mediterranean basin, \*Atmos. Chem. Phys.\*, 16,](#)  
22 [4725-4742, 2016.](#)

23 Alvarez II, R. J., Senff, C. J., Hardesty, R. M., Parrish, D. D., Like, W. T., Watson, T. B., Daum, P. H., and  
24 Gillani, N.: Comparisons of airborne lidar measurements of ozone with airborne in situ measurements during the  
25 1995 Southern Oxidants Study, *J. Geophys. Res.*, 103, 31155-31171, 1998.

26 Alvarez II, R. J., Senff, C. J., Langford, A. O., Weikmann, A. M., Law, D. C., Machol, J. L., Merritt, D. A.,  
27 Marchbanks, R. D., Sandberg, S. P., Brewer, W. A., Hardesty, R. M., and Banta, R. M.: Development and  
28 application of a compact, tunable, solid-state airborne ozone lidar system for boundary layer profiling, *J. Atmos.*  
29 *Ocean. Technol.*, 28, 1258-1271, 2011.

30 Banta, R. M., Senff, C. J., White, A. B., Trainer, M., McNider, R. T., Valente, R. J., Mayor, S. D., Alvarez, R. J.,  
31 Hardesty, R. M., Parrish, D., and Fehsenfeld, F. C.: Daytime buildup and nighttime transport of urban ozone in  
32 the boundary layer during a stagnation episode, *J. Geophys. Res.*, 103, 22519-22544, 1998.

33 Baray, J.-L., Leveau, J., Porteneuve, J., Ancellet, G., Keckhut, P., Posny, F., and Baldy, S.: Description and and  
34 evaluation of a tropospheric ozone lidar implemented on an existing lidar in the southern subtropics, *Appl. Opt.*,  
35 38, 6808-6817, 1999.

36 Baray, J.-L., Daniel, V., Ancellet, G., and Legras, B.: Planetary-scale tropopause folds in the southern  
37 subtropics, *Geophys. Res. Lett.*, 27, 353-356, 2000.

1 Blackman, R. B., and Tukey, J. W.: in: The Measurement of Power Spectra, From the Point of View of  
2 Communications Engineering, Dover, Publications, New York, U.S.A., 95-101, 1959.

3 Brenner, P., Reitebuch, O., Schäfer, K., Trickl, T., and Stichternath, A.: A Novel Mobile Vertical-sounding  
4 System for Ozone Studies in the Lower Troposphere”, Advances in Atmospheric Remote Sensing with Lidar,  
5 Selected Papers of the 18th International Laser Radar Conference, Berlin (Germany, 1996), A. Ansmann, R.  
6 Neuber, P. Rairoux, U. Wandinger, Eds., Springer (Berlin, Heidelberg, New York), 383-386, 1997.

7 Browell, E. V.: Lidar measurements of tropospheric gases, Opt. Eng., 21, 128-132, 1982.

8 Bragg, S. L., Brault, J. W., and Smith, W. H.: Line Positions and Strengths in the H<sub>2</sub> Quadrupole Spectrum,  
9 Astrophys. J., 263, 999-1004, 1982.

10 Browell, E. V., Carter, A. F., Shipley, S. T., Allen, R. J., Butler, C. F., Mayo, M. N., Siviter, J. H., and Hall, W.  
11 M.: NASA multipurpose airborne DIAL system and measurements of ozone and aerosol profiles, Appl. Opt., 22,  
12 522-534, 1983.

13 Browell, E. V., Danielsen, E. F., Ismail, S., Gregory, G. L., and Beck, S. M.: Tropopause Fold Structure  
14 Determined From Airborne Lidar and in Situ Measurements, J. Geophys. Res., 92, 2112-2120, 1987.

15 Browell, E. V., Fenn, M. A., Butler, C. F., Grant, W. B., Merrill, J. T., Newell, R. E., Bradshaw, J. D.,  
16 Sandholm, S. T., Anderson, B. E., Bandy, A. R., Bachmeier, A. S., Blake, D. R., Davis, D. D., Gregory, G. L.,  
17 Heikes, B. G., Kondo, Y., Liu, S. C., Rowland, F. S., Sachse, G. W., Singh, H. B., Talbot, R. W., and Thornton,  
18 D. C.: Large-scale air mass characteristics observed over the Western Pacific during summertime, J. Geophys.  
19 Res., 111, 1691-1712, 1996.

20 Browell, E. V., Fenn, M. A., Butler, C. F., Grant, W. B., Ismail, S., Ferrare, R. A., Kooi, S. A., Brackett, V. G.,  
21 Clayton, M. B., Avery, M. A., Barrick, J. D. W., Fuelberg, H. E., Maloney, J. C., Newell, R. E., Zhu, Y.,  
22 Mahoney, M. J., Anderson, B. E., Blake, D. R., Brune, W. H., Heikes, B. G., Sachse, G. W., Singh, H. B., and  
23 Talbot, R. W.: Large-scale air mass characteristics observed over the remote tropical Pacific Ocean during  
24 March – April 1999: Results from the PEM-Tropics B field experiment, J. Geophys. Res., 106, 32481-32501,  
25 2001.

26 Bucreev, V. S., Vartapetov, S. K., Veselovskii, I. A., Galustov, A. S., Kovalev, Y. M., Prokhorov, A. M.,  
27 Svetogorov, E. S., and Khmelevtsov, S. S., and Lee, C. H.: Excimer-laser-based lidar system for stratospheric  
28 and tropospheric ozone measurements, Quantum Electronics, 24, 546-551, 1994; translated from Kvantova  
29 Electronica, 21, 591-596, 1994.

30 Bucreev, V. S., Vartapetov, S. K., Veselovskii, I. A., Galustov, A. S., Kovalev, Y. M., Svetogorov, E. S., and  
31 Khmelevtsov, S. S.: Combined lidar system for stratospheric and tropospheric ozone measurements, Appl. Phys.  
32 B, 62, 97-101, 1996.

33 Burlakov, V. D., Dolgii, S. I., Makeev, A. P., Nevezorov, A. V., Romanovskii, O. A., and Kharchenko, O. V.: A  
34 Differential-Absorption Lidar for Ozone Sensing in the Upper Atmosphere – Lower Stratosphere, Instruments  
35 and Experimental Techniques, 53, 886-889, 2010.

36 W. Carnuth, T. Trickl, Transport studies with the IFU three-wavelength aerosol lidar during the VOTALP  
37 Mesolcina experiment, Atmos. Environ., 34, 1425-1434, 2000.

38 Carnuth, W., Kempfer, U., and Trickl, T.: Highlights of the tropospheric lidar studies at IFU within the TOR  
39 project, Tellus B, 54, 163-185, 2002.

1 Couach, O., Balin, I., Jiménez, R., Ristori, P., Perego, S., Kirchner, F., Simeonov, V., Calpini, B., and van den  
2 Berg, H.: An investigation of ozone and planetary boundary layer dynamics over the complex topography of  
3 Grenoble combining measurements and modelling, *Atmos. Chem. Phys.*, 3, 549-562, 2003.

4 Cristofanelli, P., Bonasoni, P., Collins, W., Feichter, J., Forster, C., James, P., Kentarchos, A., Kubik, P. W.,  
5 Land, C., Meloen, J., Roelofs, G. J., Siegmund, P., Sprenger, M., Schnabel, C., Stohl, A., Tobler, L., Tositti, L.,  
6 Trickl, T., and Zanis, P.: Stratosphere to troposphere transport: a model and method evaluation, *J. Geophys.*  
7 *Res.*, 108, 8525, doi: 10.1029/2002JD002600, *STA* 10, 23 pp., 2003.

8 Daumont, D., Brion, J., Charbonnier, J., and Malicet, J.: Ozone UV Spectroscopy I: Absorption Cross-Sections  
9 at Room Temperature, *J. Atmos. Chem.*, 15, 145-155, 1992.

10 De Schoulepenkoff, L., Mitev, V., Simeonov, V., Calpini, B., and van den Bergh, H.: Experimental investigation  
11 of high-power single-pass Raman shifters in the ultraviolet with Nd:YAG and KrF lasers, *Appl. Opt.*, 36, 5026-  
12 5043, 1997.

13 De Young, R., Carrion, W., Ganoe, R., Pliutau, D., Gronoff, G., Berkoff, T., and Kuang, S.: Langley mobile  
14 ozone lidar: ozone and aerosol atmospheric profiling for air quality research, *Appl. Opt.*, 56, 721-730, 2017.

15 Dickensen, G. D., Niu, M. L., Salumbides, E. J., Komasa, J., Eikema, K. S. E., Pachuki, K., and Ubachs, W.:  
16 Fundamental Vibration of Molecular Hydrogen, *Phys. Rev. Lett.*, 110, 193601, 5 pp., 2013.

17 Draxler, R., and Hess, G.: An overview of the HYSPLIT\_4 modelling system for trajectories, dispersion, and  
18 deposition, *Aust. Meteorol. Mag.*, 47, 295-308, 1998.

19 Dreessen, J., Sullivan, J., and Delgado, R.: Observations and impacts of transported Canadian wildfire smoke on  
20 ozone and aerosol air quality in the Maryland region on June 9–12, 2015, *J. Air & Waste Managem. Ass.*, 66,  
21 842-862, 2016.

22 Duclaux, O., Frejafon, E., Thomasson, A., Yu, J., C., Puel, C., Savoie, F., Ritter, P., Boch, J. P., and Wolf, J. P.:  
23 3D-air quality model evaluation using the Lidar technique, *Atmos. Environ.*, 36, 5081-5095, 2002.

24 Dufour, A., Amodei, M., Ancellet, G., and Peuch, V.-H.: Observed and modelled “chemical weather” during  
25 ESCOMPTE, *Atmos. Res.*, 74, 161-189, 2005.

26 Durieux, E., Fiorani, L., Calpini, B., Flamm, M., Jaquet, L., and van den Bergh, H.: Tropospheric Ozone  
27 Measurements over the Great Athens Area during the MEDCAPHOT-TRACE Campaign, *Atmos. Environ.*, 32,  
28 2141-2150, 1998.

29 Eisele, H.: Aufbau und Betrieb eines Dreiwellenlängen-Lidars für Ozonmessungen in der gesamten Troposphäre  
30 und Entwicklung eines neuen Auswerteverfahrens zur Aerosol-korrektur, Dissertation, Universität Tübingen  
31 (Germany, 1997), published as Schriftenreihe des Fraunhofer-Instituts für Atmosphärische Umweltforschung,  
32 Vol. 55 (Verlag Dr. W. Maraun, Frankfurt/Main, Germany, 1998), ISBN 3-932666-08-9, 107 pp., 1997 (in  
33 German).

34 Eisele, H., and Trickl, T.: Second Generation of the IFU Stationary Tropospheric Ozone Lidar, *Advances in*  
35 *Atmospheric Remote Sensing with Lidar, Selected Papers of the 18th International Laser Radar Conference*  
36 (Berlin, Germany, 1996), A. Ansmann, R. Neuber, P. Rairoux, U. Wandinger, Eds., Springer (Berlin,  
37 Heidelberg, New York), 379-382, 1997.

1 Eisele, H., Scheel, H. E., Sladkovic, R., and Trickl, T.: High-Resolution Lidar Measurements of Stratosphere-  
2 Troposphere Exchange, *J. Atmos. Sci.*, 56, 319-330, 1999.

3 Eisele, H., and Trickl, T.: Improvements of the aerosol algorithm in ozone-lidar data processing by use of  
4 evolutionary strategies, *Appl. Opt.*, 44, 2638-2651, 2005.

5 EUROTRAC: Transport and Chemical Transformation of Pollutants in the Troposphere, Vol. 1, An Overview of  
6 the Work of EUROTRAC, P. Borrell and P. M. Borrell, Eds., Springer (Berlin, Heidelberg, New York), ISBN 3-  
7 540-66775-X, 474 pp., 1997.

8 Fiorani, L., Calpini, B., Jaquet, L., van den Bergh, H., and Durieux, E.: A Combined Determination of Wind  
9 Velocities and Ozone Concentration for a First Measurement of Ozone Fluxes with a DIAL Instrument during  
10 the MEDCAPHOT-TRACE Campaign, *Atmos. Environ.*, 32, 2151-2159, 1998.

11 Fix, A., Wirth, M., Meister, A., Ehret, G., Pesch, M., and Weidauer, D.: Tunable ultraviolet optical parametric  
12 oscillator for differential absorption lidar measurements of tropospheric ozone, *Appl. Phys. B*, 75, 153-163,  
13 2002.

14 Fix, A., Steinebach, F., Wirth, M., Schäfler, A., and Ehret, G.: Development and application of an airborne  
15 differential absorption lidar for the simultaneous measurement of ozone and water vapor profiles in the  
16 tropopause region, *Appl. Opt.*, 58, 5892-5900, 2019.

17 Freudenthaler, V.: The telecover test: A Quality assurance tool for the optical part of a lidar system, in:  
18 Reviewed and Revised Papers Presented at the 24<sup>th</sup> International Laser Radar Conference, Boulder (Colorado,  
19 U.S.A.), Vol. II, M. Hardesty, S. Mayor, Eds., ISBN 978-0-615-21489-4, 145-146, 2008.

20 Giehl, H., and Trickl, T.: Testing the IFU High-Spectral-Resolution Lidar at the 2009 Leipzig Field Campaign,  
21 in: Proceedings of the 25<sup>th</sup> International Laser Radar Conference, St.-Petersburg (Russia), July 5 to 9, 2010, G.  
22 Matvienko, A. Zemlyanov, Eds., V. E. Zuev Institute of Optics (Tomsk, Russia), 920-923, 2010.

23 Galani, E., Balis, D., Zanis, P., Zerefos, C., Papayannis, A., Wernli, H., and Gerasopoulos, E.: Observations of  
24 stratosphere-to-troposphere transport events over the eastern Mediterranean using a ground-based lidar system, *J.*  
25 *Geophys. Res.*, 108, 8527, doi: 10.1029/2002JD002596, STA 12, 10 pp., 2003.

26 [Gaudel A., Ancellet G., and Godin-Beekmann S.: Analysis of 20 years of tropospheric ozone vertical profiles by  
27 lidar and ECC at Observatoire de Haute Provence \(OHP\) at 44° N, 6.7° E. \*Atmos. Environ.\*, 113, 78-89, 2015.](#)

28 Gorshelev, V., Serdyuchenko, A., Weber, M., Chebade, W., and Burrows, J. P.: High spectral resolution ozone  
29 absorption cross sections – Part 1: Measurements, data analysis and comparison with previous measurement  
30 around 293 K, *Atmos. Meas. Tech.*, 7, 609-624, 2014.

31 Grabbe, G. C., Bösenberg, J., Dier, H., Gördsdorf, U., Matthias, V., Peters, G., Schaberl, T., and Senff, C.:  
32 Intercomparison of Ozone Measurements between Lidar and ECC Sondes, *Contr. Atmos. Phys.*, 69, 189-203,  
33 1996.

34 Granados-Muñoz, M. J., and Leblanc, T.: Tropospheric ozone seasonal and long-term variability as seen by lidar  
35 and surface measurements at the JPL-Table Mountain Facility, California, *Atmos. Chem. Phys.*, 16, 9299–9319,  
36 2016.

1 Granados-Muñoz, M. J., Johnson, M. S., and Leblanc, T.: Influence of the North American monsoon on  
2 Southern California tropospheric ozone levels during summer in 2013 and 2014, *Geophys. Res. Lett.*,  
3 doi:10.1002/2017GL073375, 6431-6439, 2017.

4 Grant, W. B., and Hake, R. D.: Calibrated remote measurements of SO<sub>2</sub> and O<sub>3</sub> using atmospheric backscatter, *J.*  
5 *Appl. Phys.*, 46, 3019-3023, 1975.

6 Grant, W. B., Browell, E. V., Butler, C. F., Fenn, M. A., Clayton, M. B., Hannan, J. R., Fuelberg, H. E., Blake,  
7 D. R., Blake, N. J., Gregory, G. L., Heikes, B. G., Sachse, G. W., Singh, H. B., Snow, J., and Talbot, R. W.: A  
8 case study of transport of tropical marine boundary layer and lower tropospheric air masses to the northern  
9 midlatitude upper troposphere, *J. Geophys. Res.*, 105, 3757-3769, 2000.

10 Hearn, A. G.: The Absorption of Ozone in the Ultra-violet and Visible Regions of the Spectrum, *Proc. Phys.*  
11 *Soc.*, 78, 932-940, 1961.

12 Hoerling, M. P., Schaack, T. K., and Lenzen, A. J.: Global Objective Tropopause Analysis, *Mon. Weather Rev.*,  
13 119, 1816-1831, 1991.

14 Iarlori, M., Madonna, F., Rizi, V., Trickl, T., and Amodeo, A.: Effective resolution concepts for lidar  
15 observations, *Atmos. Meas. Tech.*, 8, 5157-5176, 2015.

16 Jäger, H., Carnuth, W., and Georgii, B.: Observations of Saharan dust at a North Alpine mountain station, *J.*  
17 *Aerosol Sci.* 19, 1235-1238, 1988.

18 Jeunouvrier, A., Mérienne, M.-F., Coquart, B., Carleer, M., Fally, S., Vandaele, A. C., Hermans, C., and Colin,  
19 R.: Fourier Transform Spectroscopy of the O<sub>2</sub> Herzberg Bands – I. Rotational Analysis, *J. Mol. Spectrosc.*, 198,  
20 136-162, 1999.

21 Jonson, J. E., Simpson, D., Fagerli, H., and Solberg, S.: Can we explain the trends in European ozone levels?  
22 *Atmos. Chem. Phys.*, 6, 51-66, 2006.

23 Kalabokas, P., Papayannis, A., Tsaknakis, G., and Ziomas, I.: A study on the atmospheric concentrations of  
24 primary and secondary air pollutants in the Athens basin performed by DOAS and DIAL measuring techniques,  
25 Science of the Total Environment, 414, 556-563, 2012.

26 Kempfer, U.: Entwicklung und Anwendung eines differentiellen Absorptions-LIDAR-Systems zur Messung der  
27 troposphärischen Ozonkonzentration, Dissertation, Ludwig-Maximilians-Universität München (Germany), 151  
28 pp., 1992.

29 Kempfer, U., Carnuth, W., Lotz, R., and Trickl, T.: A wide range ultraviolet lidar system for tropospheric ozone  
30 measurements: development and application, *Rev. Sci. Instrum.*, 65, 3145-3164, 1994.

31 Klanner, L., Höveler, K., Khordakova, D., Perfahl, M., Rolf, C., Trickl, T., and Vogelmann, H.: Lidar  
32 measurements of atmospheric water vapour up to 20 km within one hour, submitted to *Atmos. Meas. Tech.*,  
33 2020.

34 Kley, D., Crutzen, P. J., Smit, H. G. J., Vömel, H., Oltmans, S. J., Grassl, H., and Ramanathan, V.: Observations  
35 of near-zero ozone concentrations over the convective Pacific: effects of air chemistry, *Science*, 274, 230-233,  
36 1996.

37 Kley, D., Beck, J., Grennfelt, P. I., Hov, O., and Penkett, S. A.: Tropospheric Ozone Research (TOR) A Sub-  
38 Project of EUROTRAC, *J. Atmos. Chem.*, 28, 1-9, 1997.

1 Kourtidis, K., Zerefos, C., Rapsomanikis, S., Simeonov, V., Balis, D., Perros, P. E., Thompson, A. M., Witte, J.,  
2 Calpini, B., Sharobiem, W. M., Papayannis, A., Mihalopoulos, N., and Drakou, R.: Regional levels of ozone in  
3 the troposphere over eastern Mediterranean, *J. Geophys. Res.*, 107, 8140, doi: 10.1029/2000JD000140, PAU 7,  
4 13 pp., 2002.

5 Kowol-Santen, J., and Ancellet, G.: Mesoscale analysis of transport across the subtropical tropopause, *Geophys.*  
6 *Res. Lett.*, 27, 3345-3347, 2000.

7 Kreipl, S.: Messung des Aerosoltransports am Alpennordrand mittels Laserradar (Lidar), Dissertation, Friedrich-  
8 Alexander-Universität Erlangen-Nürnberg (Germany), 195 pp.; 2006; in German.

9 Krupenie, P. H.: The Spectrum of Molecular Oxygen, *J. Phys. Chem. Ref. Data*, 1,423-534, 1972.

10 Kuang, S., Burris, J. F., Newchurch, M. J., Johnson, S., and Long, S.: Differential Absorption Lidar to measure  
11 subhourly variation of tropospheric ozone profiles, *IEEE Trans. Geosci. Remote Sens.*, 49, 557-571, 2011.

12 Kuang, S., Burris, J. F., Newchurch, M. J., Johnson, S., and Long, S.: Differential Absorption Lidar to Measure  
13 Subhourly Variation of Tropospheric Ozone Profiles, *IEEE Trans. Geosci. Remote Sens.*, 49, 557-571, 2011.

14 Kuang, S., Newchurch, M. J., Burris, J., Wang, L., Knupp, K., and Huang, G.: Stratosphere-to-troposphere  
15 transport revealed by ground-based lidar and ozonesonde at a midlatitude site, *J. Geophys. Res.*, 117, D18305,  
16 doi: 10.1029/2012JD017695, 14 pp., 2012.

17 Kuang, S., Newchurch, M. J., Burris, J. F., and Liu, X.: Ground-based lidar for atmospheric boundary layer  
18 ozone measurements, *Appl. Opt.*, 52, 3557-3566, 2013.

19 Kuang, S., Newchurch, M. J., Johnson, M. S., Wang, L., Burris, J. F., Pierce, R. B., Eloranta, E. W., Pollack, I.  
20 W., Graus, M., de Gouw, J., Warneke, C., Ryerson, T. B., Markovic, M. Z., Holloway, J. S., Pour-Bazar, A.,  
21 Huang, G., Liu, X., and Feng, N.: Summertime tropospheric ozone enhancement associated with a cold front  
22 passage due to stratosphere-to-troposphere transport and biomass burning: Simultaneous ground-based lidar and  
23 airborne measurements, *J. Geophys. Res.*, 122, doi:10.1002/2016JD026078, 1293-1311, 2017.

24 Lamarque, J.-F., Langford, A. O., and Proffitt, M. H.: Cross-tropopause mixing of ozone through gravity wave  
25 breaking: Observation and modelling, *J. Geophys. Res.*, 101, 22969-22976, 1996.

26 Langford, A. O.: Identification and correction of analog-to-digital-converter nonlinearities and their implications  
27 for differential absorption lidar measurements, *Appl. Opt.*, 34, 8330-8340, 1995.

28 Langford, A. O., Masters, C. D., Proffitt, M. H., Hsie, E.-Y., and Tuck, A. F.: Ozone measurements in a  
29 tropopause fold associated with a cut-off low system, *Geophys. Res. Lett.*, 23, 2501-2504, 1996.

30 Langford, A. O., Aikin, K. C., Eubank, C. S., and Williams, E. J.: Stratospheric contribution to high surface  
31 ozone in Colorado during springtime, *Geophys. Res. Lett.*, 36, L12801, doi:10.1029/2009GL038367, 5 pp., 2009

32 Langford, A. O., Brioude, J., Cooper, O. R., Senff, C. J., Alvarez II, R. J., Hardesty, R. M., Johnson, B. J., and  
33 Oltmans, S. J.: Stratospheric influence on surface ozone in the Los Angeles area during late spring and early  
34 summer of 2010, *J. Geophys. Res.*, 117, D00V06, doi: 10.1029/2011JD016766, 17 pp., 2012.

35 Langford, A. O., Alvarez II, R. J., Brioude, J., Fine, R., Gustin, M. S., Lin, M. Y., Marchbanks, R. D., Pierce, R.  
36 B., Sandberg, S. P., Senff, C. J., Weickmann, A. M., and Williams, E. J.: Entrainment of stratospheric air and  
37 Asian pollution by the convective boundary layer in the southwestern U.S., *J. Geophys. Res.*, 122,  
38 doi:10.1002/2016JD025987, 1312-1337, 2017.

1 Langford, A. O., Alvarez II, R. J., Brioude, Evan, S., Iraci, L. T., Kirgas, G., Kuang, S., Leblanc, T., Newchurch,  
2 M. J., Pierce, R. B., Senff, C. J., and Yates, E. L.: Coordinated profiling of stratospheric intrusions and  
3 transported pollution by the Tropospheric Ozone Lidar Network (TOLNet) and NASA Alpha Jet experiment  
4 (AJAX): Observations and comparison to HYSPLIT, RAQMS, and FLEXPART, *Atmos. Environ.*, 174, 1-14,  
5 2018.

6 Lazzarotto, B., Frioud, M., Larchevêque, G., Mitev, V., Quaglia, P., Simeonov, V., Thompson, A., van den  
7 Bergh, H., and Calpini, B.: Ozone and water-vapor measurements by Raman lidar in the planetary boundary  
8 layer: error sources and field measurements, *Appl. Opt.*, 40, 2985-2997, 2001.

9 Leblanc, T., Sica, R., van Gijsel, A., Godin-Beckmann, S., Haefele, A., Trickl, T., Payen, P., and Gabarrot, F.:  
10 Proposed standardized definitions for vertical resolution and uncertainty in the NDACC lidar ozone and  
11 temperature algorithms. Part 1: Vertical resolution, *Atmos. Meas. Tech.*, 9, 4029-4049, 2016; 18 pp. of  
12 supplementary material

13 Leblanc, T., Brewer, M. A., Wang, P. S., Granados-Muñoz, M. J., Strawbridge, K. B., Travis, M., Firanski, B.,  
14 Sullivan, J. T., McGee, T. J., Sumnicht, G. K., Twigg, L. W., Berkoff, T. A., Carrion, W., Gronoff, G., Aknan,  
15 A., Chen, G., Alvarez, R. J., Langford, A. O., Senff, C. J., Kirgis, G., Johnson, M. S., Kuang, S., and  
16 Newchurch, M. J.: Validation of the TOLNet lidars: the Southern California Ozone Observation Project  
17 (SCOOP), *Atmos. Meas. Tech.*, 11, 6137-6162, 2018.

18 Leclair De Bellevue, J., Réchou, A., Baray, J. L., Ancellet, G., and Diab, R. D.: Signatures of stratosphere to  
19 troposphere transport near deep convective events in the southern subtropics, *J. Geophys Res.*, 111, D24107, doi:  
20 10.1029/2005JD006947, 14 pp., 2006.

21 Liang, Q., Jaeglé, L., Hudman, R. C., Turquety, S., Jacob, D. J., Avery, M. A., Browell, E. V., Sachse, G. W.,  
22 Blake, D. R., Brune, W., Ren, X., Cohen, R. C., Dibb, J. E., Fried, A., Fuelberg, H., Porter, M., Heikes, B. G.,  
23 Huey, G., Singh, H. B., and Wennberg, P. O.: Summertime influence of Asian pollution in the free troposphere  
24 over North America, *J. Geophys. Res.*, 112, D12S11, doi: 10.1029/2006JD007919, 20 pp., 2007.

25 Machol, J. L., Marchbanks, R. D., Senff, C. J., McCarty, B. J., Eberhard, W. L., Brewer, W. A., Richter, R. A.,  
26 Alvarez II, R. J., Law, D. C., Weickmann, A. M., and Sandberg, S. P.: Scanning tropospheric ozone and aerosol  
27 lidar with double-gated photomultipliers, *Applied Optics*, 48, 512-524, 2008.

28 Malicet, J., Daumont, D., Charbonnier, J., Parisse, C., Chakir, A., and Brion, J.: Ozone UV Spectroscopy I:  
29 Absorption Cross-Sections and Temperature Dependence, *J. Atmos. Chem.*, 21, 263-273, 1995.

30 Marenco, A., Thouret, V., Nédélec, P., Smit, H., Helten, M., Kley, D., Karcher, F., Simon, P., Law, K., Pyle, J.,  
31 Poschmann, G., von Wrede, R., Hume, C., and Cook, T.: Measurement of ozone and water vapor by Airbus in-  
32 service aircraft: The MOZAIC airborne program, An overview, *J. Geophys. Res.*, 103, 25631-25642, 1998.

33 Matthias, M.: Vertikalmessungen der Aerosolextinktion und des Ozons mit einem UV-Raman-Lidar,  
34 Dissertation, Universität Hamburg, published as Examensarbeit Nr. 80, Max-Planck-Institut für Meteorologie  
35 (Hamburg, Germany), ISSN 0938-5177, 143 pp., 2000 (in German).

36 McDermid, I. S., Haner, D. A., Kleiman, M. M., Walsh, T. D., and White, M. L.: Differential absorption lidar  
37 systems for tropospheric and stratospheric ozone measurements, *Opt. Engin.*, 30, 22-30, 1991.

1 McDermid, I. S., Beyerle, G., Haner, D. A., and Leblanc, T.: Redesign and improved performance of the  
 2 tropospheric ozone lidar at the Jet Propulsion Laboratory Table Mountain Facility, *Appl. Opt.*, 41, 7550-7555,  
 3 2002.

4 Milton, M. J. T., Ancellet, G., Apituley, A., Bösenberg, J., Carnuth, W., Castagnoli, F., Trickl, T., Edner, H.,  
 5 Stefanutti, L., Schaberl, T., Sunesson, A., and Weitkamp, C.: Raman-shifted laser sources suitable for  
 6 differential-absorption lidar measurements of ozone in the troposphere, *Appl. Phys. B*, 66, 105-113, 1998.

7 [Mytilinaios, M., Papayannis, A., and Tsaknakis, G.: Lower-free tropospheric ozone DIAL measurements over](#)  
 8 [Athens, Greece". EPJ Web of Conferences, 176, 05025, doi.org/10.1051/epjconf/201817605025, 2018.](#)

9 Nakazato, M., Nagai, T., Sakai, T., and Hirose, Y.: Tropospheric ozone differential-absorption lidar using  
 10 stimulated Raman scattering in carbon dioxide, *Appl. Opt.*, 46, 2269-2279, 2007.

11 Newchurch, M. J., Kuang, S., Leblanc, T., Alvarez II, R. J., Langford, A. O., Senff, C. J., Burris, J. F., McGee,  
 12 T. J., Sullivan, J. T., DeYoung, R. J., Al-Saadi, J., Johnson, M., and Pszenny, A.: TOLNet – A Tropospheric  
 13 Ozone Lidar Profiling Network for Satellite Continuity and Process Studies, *Proc. 27<sup>th</sup> International Laser Radar*  
 14 *Conference*, New York (U.S.A., 2015), EPJ Web of Conferences, 119, 20001, 4 pp., 2016.

15 Newell, R. E., Browell, E. V., Davis, D. D., and Liu, S. C.: Western Pacific ozone and potential vorticity:  
 16 Implications for Asian pollution, *Geophys. Res. Lett.*, 24, 2733-2736, 1997.

17 Ordoñez, C., Brunner, D., Stachelin, J., Hadjinicolaou, P., Pyle, J. A., Jonas, M., Wernli, H., and Prévôt, A. S.  
 18 H.: Strong influence of lowermost stratospheric ozone on lower tropospheric background ozone changes over  
 19 Europe, *Geophys. Res. Lett.*, 34, L07805, doi: 10.1029/2006GL029113, 5 pp., 2007.

20 Pan, L. L., Randel, W. J., Gary, B. L., Mahoney, M. J., and Hints, E. J.: Definitions and sharpness of the  
 21 extratropical tropopause: A trace gas perspective, *J. Geophys. Res.*, 109, D23103, doi: 10.1029/2004JD004982,  
 22 11 pp., 2004.

23 Papayannis, A., Balis, D., Zanis, P., Galani, E., Wernli, H., Zerefos, C., Stohl, A., Eckhardt, S., and Amiridis, V.:  
 24 Sampling of an STT event over the Eastern Mediterranean region by lidar and electrochemical sonde, *Ann.*  
 25 *Geophys.*, 23, 2039-2050, 2005. Papayannis, A., Amiridis, V., Mona, L., Tsaknakis, G., Balis, D., Bösenberg, J.,  
 26 Chaikovsky, A., De Tomasi, F., Grigorov, I., Mattis, I., Mitev, V., Müller, D., Nickovic, S., Pérez, C.,  
 27 Pietruczuk, A., Pisani, G. L., Ravetta, F., Rizi, V., Sicard, M., Trickl, T., Wiegner, M., Gerdin, M., Mamouri,  
 28 R. E., D'Amico, G., and Pappalardo, G.: Systematic lidar observations of Saharan dust over Europe in the frame  
 29 of EARLINET (2000-2002), *J. Geophys. Res.*, 113, D10204; doi: 10.1029/2007JD009028, 17 pp., 2008.

30 [Papayannis, A., Añellet, G., Pelon, J., and Mégie, G.: Multiwavelength lidar for ozone measurements in the](#)  
 31 [troposphere and the lower stratosphere. Appl. Opt.](#) 29, 467-476, 1990.

32 Pelon, J., and Mégie, G.: Ozone Monitoring in the Troposphere and Lower Stratosphere: Evaluation and  
 33 Operation of a Ground-Based Lidar Station, *J. Geophys. Res.*, 87, 4947-4955, 1982.

34 Perrone, M. R., and Piccinno, V.: On the benefits of astigmatic focusing configurations in stimulated Raman  
 35 scattering processes, *Opt. Comm.*, 133; 534-540, 1997.

36 Proffitt, M. H., and Langford, A. O.: Ground-based differential-absorption lidar system for day or night  
 37 measurements of ozone throughout the free troposphere, *Appl. Opt.*, 36, 2568-2585, 1997.

1 Ravetta, F., Ancellet, G., Kowol-Santen, J., Wilson, R., and Nedeljkovic, D.: Ozone, Temperature, and Wind  
2 Field Measurements in a Tropopause Fold: Comparison with a Mesoscale Model Simulation, *Mon. Wea. Rev.*,  
3 127, 2641-2653, 1999.

4 Ravetta, F., Ancellet, A., Colette, A., and Schlager, H.: Long-range transport and tropospheric ozone variability  
5 in the western Mediterranean region during the Intercontinental Transport of Ozone and Precursors (ITOP-2004)  
6 campaign, *J. Geophys. Res.*, 112, D10S46, doi: 10.1029/2006JD007724, 12 pp., 2007.

7 Reichardt, J., Wandinger, U., Servazi, M., and Weitkamp, C.: Combined Raman lidar for aerosol, ozone and  
8 moisture measurements, *Opt. Eng.*, 35, 1457-1465, 1996.

9 Roelofs, G. J., Kentarchos, A. S., Trickl, T., Stohl, A., Collins, W. J., Crowther, R. A., Hauglustaine, D.,  
10 Klonecki, A., Law, K. S., Lawrence, M. G., von Kuhlmann, R., and van Weele, M.: Intercomparison of  
11 tropospheric ozone models: Ozone transport in a complex tropopause folding event, *J. Geophys. Res.*, 108, 8529,  
12 10.1029/2003JD003462, STA 14, 13 pp., 2003.

13 Scheel, H. E.: Ozone Climatology Studies for the Zugspitze and Neighbouring Sites in the German Alps, pp.  
14 134-139 in: *Tropospheric Ozone Research 2*, EUROTRAC-2 Subproject Final Report, A. Lindskog, Co-  
15 ordinator, EUROTRAC International Scientific Secretariat (München, Germany, 2003);  
16 <http://www.trickl.de/scheel.pdf>.

17 Seibert, P., Feldmann, H., Neininger, B., Bäumle, M., and Trickl, T.: South foehn and ozone in the Eastern  
18 Alps – case study and climatological aspect, *Atmos. Environ.*, 34, 1379-1394, 2000.

19 Senff, C. J., Hardesty, R. M., Alvarez II, R. J., and Mayor, S. D.: Airborne lidar characterization of power plant  
20 plumes during the 1995 Southern Oxidants Study, *J. Geophys. Res.*, 103, 31173-31189, 1998.

21 Senff, C. J., Alvarez II, R. J., Hardesty, R. M., Banta, R. M., and Langford, A. O.: Airborne lidar measurements  
22 of ozone flux downwind of Houston and Dallas, *J. Geophys. Res.*, 115, D20307, doi:10.1029/2009JD013689, 13  
23 pp., 2010.

24 Serdyuchenko, A., Gorshelev, V., Weber, M., Chebade, W., and Burrows, J. P.: High spectral resolution ozone  
25 absorption cross sections – Part 2: Temperature dependence, *Atmos. Meas. Tech.*, 7, 625–636, 2014, 2014.

26 Simeonov, V., Larcheveque, G., Quaglia, P., van den Bergh, H., and Calpini, B.: Influence of the photomultiplier  
27 tube spatial uniformity on lidar signals, *Appl. Opt.*, 38, 5186-5190, 1999.

28 Simeonov, V., Ristori, P., Taslakov, M., Dinoev, T., Molina, L. T., Molina, M. J., and van den Bergh, H.: Ozone  
29 and aerosol distribution above Mexico City measured with a DIAL/elastic lidar system during the Mexico City  
30 Metropolitan Area (MCMA) 2003 field campaign, in: *Lidar Technologies, Techniques, and Measurements for*  
31 *Atmospheric Remote Sensing*, U. N. Singh, Ed., *Proc. SPIE*, 5968, 59840O, doi: 10.1117/12.629429, 8 pp.,  
32 2005.

33 Stohl, A., and Trickl, T.: A textbook example of long-range transport: Simultaneous observation of ozone  
34 maxima of stratospheric and North American origin in the free troposphere over Europe, *J. Geophys. Res.*, 104,  
35 30445-30462, 1999.

36 Stohl, A., Spichtinger-Rakowsky, N., Bonasoni, P., Feldmann, H., Memmesheimer, M., Scheel, H. E., Trickl, T.,  
37 Hübener, S., Ringer, W., and Mandl, M.: The influence of stratospheric intrusions on alpine ozone  
38 concentrations, *Atmos. Environ.*, 34, 1323-1354, 2000.

IrupdwluhuvkuliwDukkhw

1 Stohl, A., Bonasoni, P., Cristofanelli, P., Collins, W., Feichter, J., Frank, A., Forster, C., Gerasopoulos, E.,  
2 Gäggeler, H., James, P., Kentarchos, T., Kromp-Kolb, H., Krüger, B., Land, C., Meloen, J., Papayannis, A.,  
3 Priller, A., Seibert, P., Sprenger, M., Roelofs, G. J., Scheel, H. E., Schnabel, C., Siegmund, P., Tobler, L., Trickl,  
4 T., Wernli, H., Wirth, V., Zanis, P., and Zerefos, C.: Stratosphere-troposphere exchange - a review, and what we  
5 have learned from STACCATO, *J. Geophys. Res.*, 108, 8516, doi:10.1029/2002JD002490, STA 1, 15 pp., 2003.

6 Strawbridge, K. B., Travis, M. S., Firanski, B. J., Brook, J. R., Staebler, R., and Leblanc, T.: A fully autonomous  
7 ozone, aerosol and nighttime water vapour lidar: a synergistic approach to profiling the atmosphere in the  
8 Canadian oil sands region, *Atmos. Meas. Tech.*, 11, 6735–6759, 2018.

9 Sullivan, J. T., McGee, T. J., Sumnicht, G. K., Twigg, L. W., and Hoff, R. M.: A mobile differential absorption  
10 lidar to measure sub-hourly fluctuations of tropospheric ozone in the Baltimore-Washington, D.C. region,  
11 *Atmos. Meas. Tech.*, 7, 3529-3548, 2014.

12 Sullivan, J. T., McGee, T. J., Thompson, A. M., Pierce, R. B., Sumnicht, G. K., Twigg, L. W., Eloranta, E. W.,  
13 and Hoff, R. M.: Characterizing the lifetime and occurrence of stratospheric-tropospheric exchange events in the  
14 rocky mountain region using high-resolution ozone measurements, *J. Geophys. Res.*, 120, 12410-12424, doi:  
15 10.1002/2015JD023877, 2016.

16 Sullivan, J. T., Rabenhorst, S. T., Dreessen, J., McGee, T. J., Delgado, R., Twigg, L., and Sumnicht, G.: Lidar  
17 observations revealing transport of O<sub>3</sub> in the presence of a nocturnal low-level jet: Regional implications for  
18 “next-day” pollution, *Atmos. Environ.*, 158, 160-171, 2017.

19 Sunesson, J. A., Apituley, A., and Swart, D. P. J.: Differential absorption lidar system for routine monitoring of  
20 tropospheric ozone, *Appl. Opt.*, 33, 7045-7058, 1994.

21 Tarasick, D., Galbally, I. E., Cooper, O. R., Schultz, G M., Ancellet, G., Leblanc, T., Wallington, T. J., Ziemke,  
22 J., Liu, X., Steinbacher, M., Staehelin, J., Vigouroux, C., Hannigan, J., Garcia, O., Foret, G., Zanis, P.,  
23 Weatherhead, E., Petropavlovskikh, I., Worden, H., Osman, M., Liu, J., Chang, K.-L., Gaudel, A., Lin, M.,  
24 Granados-Muñoz, M., Thompson, A. M., Oltmans, S. J., Cuesta, J., Dufour, G., Thouret, V., Hassler, B., Trickl,  
25 T., and Neu, J. L.: Tropospheric Ozone Assessment Report: Tropospheric ozone from 1877 to 2016, observed  
26 levels, trends and uncertainties, *Elem. Sci. Anth.*, 7, Article 39, DOI: <https://doi.org/10.1525/elementa.376>, 72  
27 pp. (plus 56 pp. of supplemental material), 2019.

28 TESLAS: Tropospheric Environmental Studies by Laser Sounding (TESLAS), in: *Transport and Chemical*  
29 *Transformation of Pollutants in the Troposphere*, Vol. 8, *Instrument Development for Atmospheric Research and*  
30 *Monitoring*, J. Bösenberg, D. Brassington, and P. C. Simon, Eds., Springer (Berlin, Heidelberg, New York),  
31 ISBN 3-540-62516-X, 1-203, 1997.

32 Thomasson, A., Geffroy, S., Frejafon, E., Weidauer, D., Fabian, R., Godet, Y., Nominé, M., Ménard, T.,  
33 Rairoux, P., Moeller, D., and Wolf, J. P.: LIDAR mapping of ozone-episode dynamics and intercomparison with  
34 spot analyzers, *Appl. Phys. B*, 74, 453-459, 2002.

35 Trickl, T.: Lidar Studies of Tropospheric Transport, in: *Tropospheric Ozone Research 2*, *EUROTRAC-2*  
36 *Subproject Final Report*, A. Lindsjö, Subproject Co-ordinator, *EUROTRAC-2 International Scientific*  
37 *Secretariat* (München, Germany, 2003), 146-159, 2003; <http://www.trickl.de/TOR.pdf>

38 Trickl, T.: Upgraded 1.56-μm lidar at IMK-IFU with 0.28 J/pulse, *Appl. Opt.*, 49, 3732-3740, 2010.

1 Trickl, T.: Tropospheric trace-gas measurements with the differential-absorption lidar technique, in: Recent  
2 Advances in Atmospheric Lidars, L. Fiorani, V. Mitev, Eds., INOE Publishing House, Bucharest (Romania),  
3 Series on Optoelectronic Materials and Devices, Vol. 7, ISSN 1584-5508, ISSN 978-973-88109-6-9; 87-147,  
4 2010; revised version: <http://www.trickl.de/DIAL.pdf>.

5 Trickl, T., Vrakking, M. J. J., Cromwell, E. F., Lee, Y. T., and Kung, A. H.: Ultrahigh-resolution (1 + 1)  
6 photoionization spectroscopy of Kr I: Hyperfine structures, isotope shifts and lifetimes for the  $n = 5, 6, 7$  4p 5ns  
7 Rydberg levels, Phys. Rev. A, 39, 2948-2955, 1989.

8 Trickl, T., Cooper, O. R., Eisele, H., James, P., Mücke, R., and Stohl, A.: Intercontinental transport and its  
9 influence on the ozone concentrations over central Europe: Three case studies, J. Geophys. Res., 108, D12, 8530,  
10 10.1029/2002JD002735, STA 15, 23 pp., 2003.

11 Trickl, T., A. H. Kung, A. H., and Y. T. Lee, Y. T.: Krypton atom and testing the limits of extreme-ultraviolet  
12 tunable-laser spectroscopy, Phys. Rev. A 75, 022501, 13 pp, 2007.

13 Trickl, T., Feldmann, H., Kanter, H.-J., Scheel, H. E., Sprenger, M., Stohl, A., and Wernli, H.: Deep  
14 stratospheric intrusions over Central Europe: case studies and climatological aspects, Atmos. Chem. Phys., 10,  
15 499-524, 2010.

16 Trickl, T., Eisele, H., Bärtsch-Ritter, N., Furger, M., Mücke, R., Sprenger, M., and Stohl, A.: High-ozone layers  
17 in the middle and upper troposphere above Central Europe: potential import from the stratosphere along the  
18 subtropical jet stream, Atmos. Chem. Phys., 11, 9343-9366; 5-p. Supplement, 2011.

19 Trickl, T., Vogelmann, H., Giehl, H., Scheel, H. E., Sprenger, M., and Stohl, A.: How stratospheric are deep  
20 stratospheric intrusions? Atmos. Chem. Phys., 14, 9941-9961, 2014.

21 Trickl, T., Vogelmann, H., Flentje, H., and Ries, L.: Stratospheric ozone in boreal fire plumes – the 2013 smoke  
22 season over Central Europe, Atmos. Chem. Phys., 15, 9631-9649, 2015.

23 Trickl, T., Vogelmann, H., Fix, A., Schäfler, A., Wirth, M., Calpini, B., Levrat, G., Romanens, G., Apituley, A.,  
24 Wilson, K. M., Begbie, R., Reichardt, J., Vömel, H. and Sprenger, M.: How stratospheric are deep stratospheric  
25 intrusions into the troposphere? LUAMI 2008, Atmos. Chem. Phys., 16, 8791-8815, 2016.

26 Trickl, T., Vogelmann, H., Ries, L., and Sprenger, M.: Very high stratospheric influence observed in the free  
27 troposphere over the Northern Alps – just a local phenomenon? Atmos. Chem. Phys., 20, 243-266, 2020.

28 Uchino, O., Tokunaga, M., Maeda, M., and Miyazoe, Y.: Differential-absorption-lidar measurements of  
29 tropospheric ozone with excimer-Raman hybrid laser, Opt. Lett., 8, 347-349, 1983.

30 Uchino, O., Sakai, T., Nagai, T., Morino, I., Maki, T., Deushi, M., Shibata, K., Kajino, M., Kawasaki, T., Akaho,  
31 T., Takubo, S., Okumura, H., Arai, K., Nakazato, M., Matsunaga, T., Yokota, T., Kawakami, S., Kita, K., and  
32 Sasano, Y.: DIAL measurement of lower tropospheric ozone over Saga (33.24° N, 130.29° E), Japan, and  
33 comparison with a chemistry-climate model, Atmos. Meas. Tech., 7, 1385-1394, 2014.

34 U.S. Standard Atmosphere 1976, National Oceanic and Atmospheric Organization (NOAA), National  
35 Aeronautics and Space Administration, United States Air Force, NOAA-S/T 76-1562, U.S. Printing Office  
36 (Washington, D.C.), 227 pp., 1976.

37 Uthe, E. E., and Livingston, J. M.: Airborne Lidar Mapping of Ozone Concentrations During the Lake Michigan  
38 Ozone Study, J. Air Waste Manage. Assoc., 42, 1313-1318, 1992.

1 Valente, R. J., Imhoff, R. E., Tanner, R. L., Meagher, J. F., Daum, P. H., Hardesty, R. M., Banta, R. M., Alvarez,  
2 R. J., McNider, R. T., and Gillani, N. V.: Ozone production during an urban air stagnation episode over  
3 Nashville, Tennessee, *J. Geophys Res.*, 103, 22555-22568, 1998.

4 Vautard, R., Szopa, S., Beekmann, M., Menut, L., Hauglustaine, D. A., Rouil, L., and Roemer, M.: Are decadal  
5 anthropogenic emission reductions in Europe consistent with surface ozone observations? *Geophys. Res. Lett.*,  
6 33, L13810, doi:10.1029/2006GL026080, 4 pp., 2006.

7 VDI guide line 4210, Remote Sensing, Atmospheric Measurements with LIDAR, Measuring gaseous air  
8 pollution with the DAS LIDAR (Verein Deutscher Ingenieure, Düsseldorf, Germany), 47 pp., 1999.

9 Veselovskii, I., and Barchunov, B.: Excimer-laser-based lidar for tropospheric ozone monitoring, *Appl. Phys. B*,  
10 68, 1131-1137, 1999.

11 Viallon, J., Lee, S., Moussay, P., Tworek, K., Peterson, M., and Wielgosz, R. I.: Accurate measurements of  
12 ozone absorption cross-sections in the Hartley band, *Atmos. Meas. Tech.*, 8, 1245-1257, 2015.

13 Völger, P., Bösenberg, J., and Schult, I.: Scattering Properties of Selected Model Aerosols Calculated at UV-  
14 Wavelengths: Implications for DIAL Measurements of Tropospheric Ozone, *Beitr. Phys. Atmosph.*, 69, 177-  
15 187, 1996.

16 Vogelmann, H. and Trickl, T.: Wide-Range Sounding of Free-Tropospheric Water Vapor with a Differential-  
17 Absorption Lidar (DIAL) at a High-Altitude Station, *Appl. Opt.*, 47, 2116-2132, 2008.

18 VOTALP II: Vertical Ozone Transport in the Alps II, Final Report for the European Union, Contract Nr.: ENV4  
19 CT970413, Reporting Period 1/3/1998-29/2/2000, H. Kromp-Kolb, Co-ordinator, Universität für Bodenkultur  
20 Wien (Austria), Institut für Meteorologie und Physik, 96 pp., 2000.

21 Wallinder, E., Edner, H., Ragnarson, P., and Svanberg, S.: Vertically Sounding Ozone Lidar System based on a  
22 KrF Excimer Laser, *Physica Scripta*, 55, 714-718, 1997.

23 Wang, L., Newchurch, M. J., Alvarez II, R. J., Berkoff, T. A., Brown, S. S., Carrion, W., De Young, R. J.,  
24 Johnson, B. J., Ganoe, R., Gronoff, G., Kirgis, G., Kuang, S., Langford, A. O., Leblanc, T., McDuffie, E. E.,  
25 McGee, T. J., Pliutau, D., Senff, C. J., Sullivan, J. T., Sumnicht, G., Twigg, L. W., and Weinheimer, A. J.:  
26 Quantifying TOLNet ozone lidar accuracy during the 2014 DISCOVER-AQ and FRAPPÉ campaigns, *Atmos.*  
27 *Meas. Tech.*, 10, 3865-3876, 2017.

28 Weitkamp, C., Baumbach, G., Becker, K.-H., Braun-Schoen, S., Burger, H., Dinev, S., Fabian, R., Frey, S.,  
29 Fritzsche, F., Glaser, K., Glauer, J., Herb, F., Immler, F., Junkermann, W., Kanter, H. J., Lindemann, C.,  
30 Loescher, A., Mohnen, V. A., Möller, D., Neidhart, B., Olariu, R., Reimer, E., Schmidt, V., Schubert, G.,  
31 Spittler, M., Vogt, U., Weidauer, D., Windholz, L., and Wöste, L.: Wie richtig sind Lidarmessungen der  
32 Ozonverteilung?, *Gefahrstoffe – Reinhal tung der Luft*, 60, 279-284, 2000; in German

33 Wotava, G., and Kromp-Kolb, H.: The research project VOTALP – general objectives and main results, *Atmos.*  
34 *Environ.*, 34, 1319-1322, 2000.

35 Yates, E. L., Johnson, M. S., Iraci, L. T., Ryoo, J.-M., Pierce, R. B., Cullis, P. D., Gore, W., Ives, M. A.,  
36 Johnson, B. J., Leblanc, T., Marrero, J. E., Sterling, C. W., and Tanaka, T.: An Assessment of Ground Level and  
37 Free Tropospheric Ozone Over California and Nevada, *J. Geophys. Res.*, 122, 10089-10102,  
38 <https://doi.org/10.1002/2016JD026266>, 2017.

1 Zanis, P., Trickl, T., Stohl, A., Wernli, H., Cooper, O., Zerefos, C., Gaeggeler, H., Priller, A., Schnabel, C.,  
2 Scheel, H. E., Kanter, H. J., Tobler, L., Kubik, P. W., Cristofanelli, P., Forster, C., James, P., Gerasopoulos, E.,  
3 Delcлоo, A., Papayannis, A., and Claude, H.: Forecast, observation and modelling of a deep stratospheric  
4 intrusion event over Europe, *Atmos. Chem. Phys.*, 3, 763-777, 2003.

5 Zhao, Y., Howell, J. N., and Hardesty, R. M.: Transportable Lidar for the Measurement of Ozone Concentration  
6 and Flux Profiles in the Lower Troposphere, in: *Proceedings of the 16<sup>th</sup> International Laser Radar Conference*,  
7 Cambridge (Massachusetts, U.S.A, 1992), 185-187, 1992.

8 Zhao, Y., Marchbanks, R. D., Senff, C. J., and Johnson, H. D.: Lidar Profiling of Ozone and Aerosol in the  
9 SCOS97-NARSTO Experiment, in: *Proceedings of the Nineteenth International Laser Radar Conference*,  
10 Annapolis (Maryland, U.S.A., 1998), U. N. Singh, S. Ismail, and G. K. Schwemmer, Eds., NASA Langley  
11 Research Center, NASA/CP-1998-207671/PT1, 375-378, 1998.

12

1 **Table 1. Transmitter Details**

2 The numbers are given for normal operating conditions

	<b>Stationary system</b>	<b>Mobile system</b>
4	Laser source	KrF laser
5	Wavelength	245.50 nm
6	Pulse energy	400 mJ
7	Pulse repetition rate	99 Hz
8	Operating wavelengths [nm]	277.124 <sup>a</sup> , 291.838 <sup>b</sup> , 313.188 <sup>a</sup>
9	Emission	simultaneous
10		289 nm and 299 nm sequential, 266 nm for each pulse
11	Beam expansion	5:1
12	Beam divergence	< 0.75 mrad
13		< 0.5 mrad

14 (a) Q<sub>1</sub> line of first Stokes shift in H<sub>2</sub> (Bragg et al., 1982; Dickensen et al., 2013): 4155.2521 cm<sup>-1</sup>

15 (b) Q<sub>2</sub> second Stokes shift in D<sub>2</sub> (Jennings et al., 1986): 2987.289 cm<sup>-1</sup>

16

1 **Table 2. Receiver Details**

2 Latest version only

	<b>Stationary system</b>	<b>Mobile system</b>
4 Primary mirrors	0.13 m diameter, $f = 0.72$ m	0.36 m diameter, $f = 1.56$ m
5	0.50 m diameter, $f = 2.0$ m	
6 Wavelength separation	two 1.1-m grating	sequential detection of 289 nm,
7	Spectrographs	299 nm, 266 nm optically separated
8 PMTs	Hamamatsu 7400,	Hamamatsu 5600
9	modified by RSV	
10 Pre-amplifiers	gain 1–10, bandwidth 4 MHz	
11	(1996–2011)	
12 Transient digitizers	6 units, 12 bit, 20 MHz	4 units, 12 bit, 20 MHz
13	ground-free input stages	
14 Photon counting	10 GHz time bins	
15 <u>Measurement time</u>	<u>41 s</u>	<u>10 min</u>

16

1    **Table 3. Measurement periods of the stationary DIAL**

2    **Projects:** TOR (EUROTRAC subproject Tropospheric Ozone Research <sup>a</sup>), VOTALP (Vertical Ozone Transport  
3    in the Alps<sup>b</sup>), STACCATO (Influence of Stratosphere-Troposphere Exchange in a Changing Climate on  
4    Atmospheric Transport and Oxidation Capacity<sup>c</sup>), ATMOFAST (German abbreviation of “Atmospheric Long-  
5    range Transport and its Impact on the Trace-gas Concentrations in the Free Troposphere over Central Europe”<sup>d</sup>);  
6    for references see text.

7 <b>Period</b>	8 <b>Measurements</b>	9 <b>Comments</b>
10    Jan.-Dec. 1991	11    580 measurements (just about 60 12    re-evaluated)	13    within TOR
14    1993	15    a few measurements	16    within TOR
17    Jan. 1996-Feb. 1998	18    1122 evaluated measurements	19    within VOTALP 1+2
20    May 1999	21    86 evaluated measurements	22    within VOTALP 2
23    Aug. 2000-Aug. 2001	24    520 evaluated measurements	25    within STACCATO
26    July 2003	27    37 evaluated measurements	28    within ATMOFAST
29    2007-2018	30    2959 evaluated measurements	31    routine measurements; gaps due to repairs

1 **Table 4. Uncertainties of the stationary ozone lidar**

2 Altitudes: above sea level (a.s.l.); E ... EMI PMTs, H ... Hamamatsu PMTs

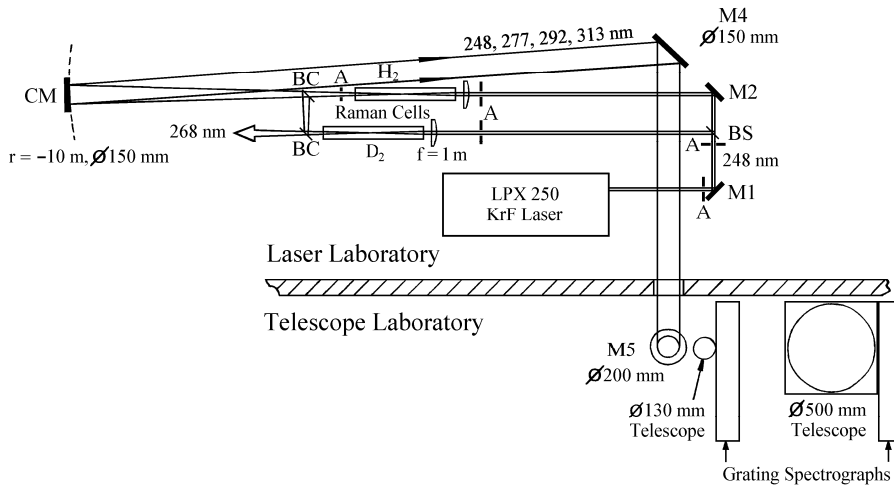
3	Period	1-2.3 km	2.3-5 km.	5-8 km	8 km-tropopause	Electronics
4	1991-1993	5 ppb	3-5 ppb	5-20 ppb	not reached	8 bit DSP, E
5	1996-4/1996	5 ppb	2-4 ppb	4-8 ppb	up to 10 ppb (winter)	12 bit DSP, E
6					up to 20 ppb (summer)	
7	5/1996-4/1997	5 ppb	2-4 ppb	4-8 ppb	unknown <sup>*)</sup>	12 bit DSP, H
8	5/1997-2003	5 ppb	2-4 ppb	4-8 ppb	best: 7 ppb; up to 10 ppb (winter)	12 bit DSP, H,
9					best: 7-10 ppb; up to 20 ppb (summer)	1 GHz Optec
10	2007-2011	5 ppb	2.5-4 ppb	3-7 ppb	best: 7 ppb; up to 10 ppb (winter)	12 bit Licel, H
11					best: 7-10 ppb; up to 20 ppb (summer)	
12	2012-2019	2-4 ppb	1.5-4 ppb	3-7 ppb	best: 5 ppb; up to 8 ppb (winter)	12 bit Licel, H
13					best: 5-8 ppb; up to 15 ppb (summer)	(ground-free)

14 <sup>\*)</sup> Sometimes artefacts in upper troposphere due to preamplifier ringing, corrected for important examples

15

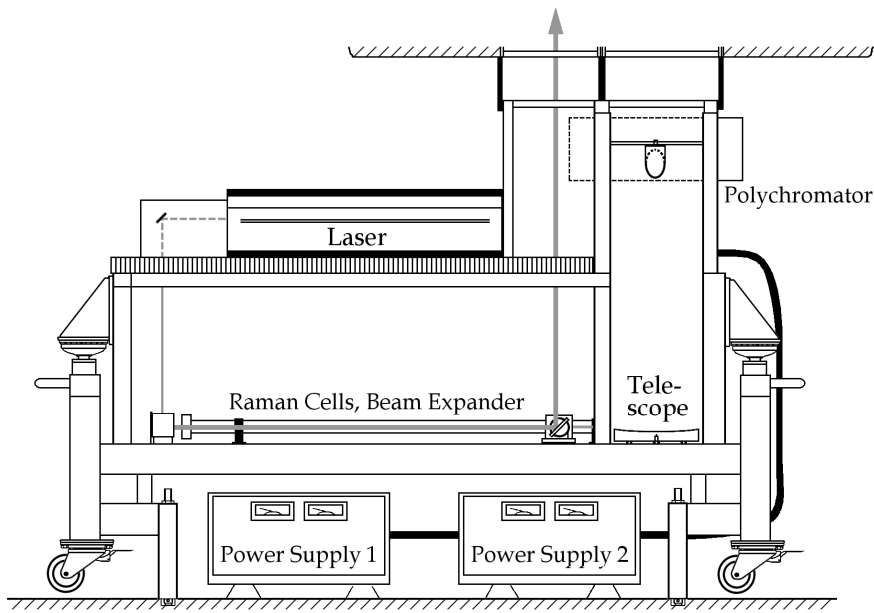
1 **Figures:**

2  
3



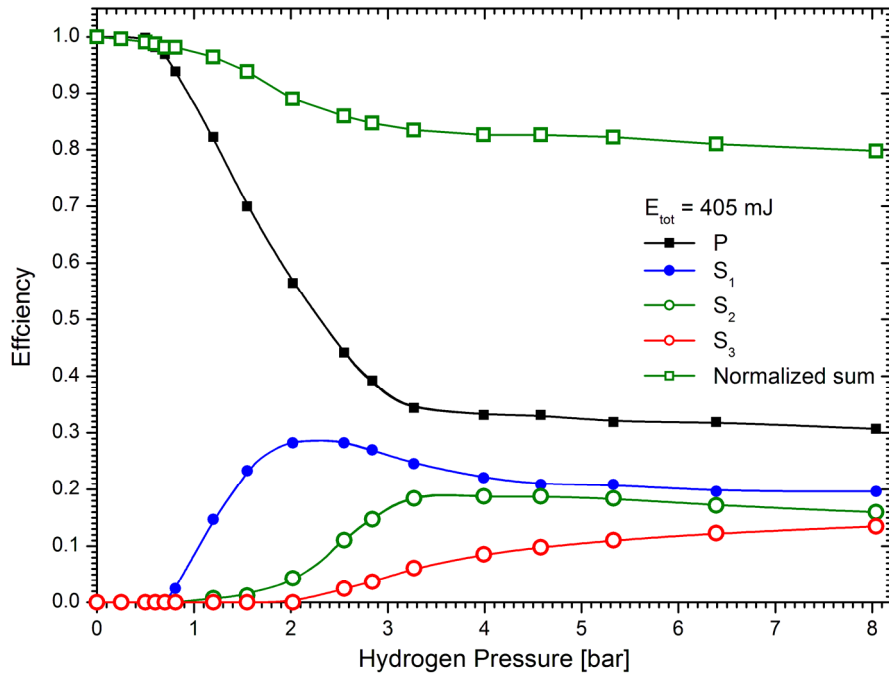
4 **Fig. 1.** Overview of the IFU stationary ozone DIAL system; the system covers two separate laboratories for the  
5 laser and the telescopes, respectively. Abbreviations:  
6 M1, M2 ... dielectric high-reflecting mirrors for 248 nm  
7 SM ... spherical mirror ("M3"), high reflecting for 248 to 313 nm,  $f = 5$  m  
8 M4, M5 ... dielectric mirrors, high reflecting for 248 to 313 nm  
9 BS ... 50-% beam splitter  
10 BC ... wavelength-selective beam combiner, reflecting 99 % at 292 nm for an incidence angle of  $45^\circ$  and  
11 transmitting all the other lidar wavelengths with losses of not exceeding 12 %.  
12 A ... rectangular sand-blasted aluminium apertures for blocking divergent parts of the amplifier emission that  
13 would otherwise hit and evaporate the black surfaces of the optics holders, leading to more rapid ageing of the  
14 optics.  
15

1



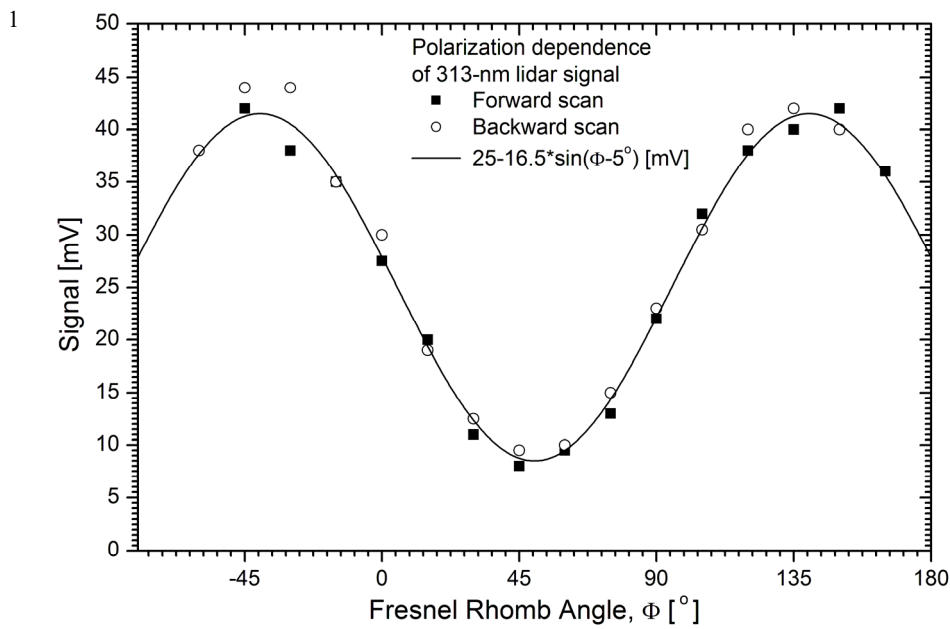
2 **Fig. 2.** Overview of the mobile ozone DIAL: the laser and the Raman-shifting components were mounted on  
 3 optical tables at two different levels of a shock-isolated frame. The Newtonian telescope was located in a  
 4 separate tower, the secondary mirror directing the beam into a polychromator perpendicularly to the plane  
 5 formed by the telescope and the outgoing laser beam. The covers of the Raman compartment (jalousies on both  
 6 sides) and the telescope (door) were removed in this simple view. The laser power supply was delivered in two  
 7 units custom-made to fit under the lower laser table. The entire frame was rolled into the the lorry through the  
 8 rear doors.

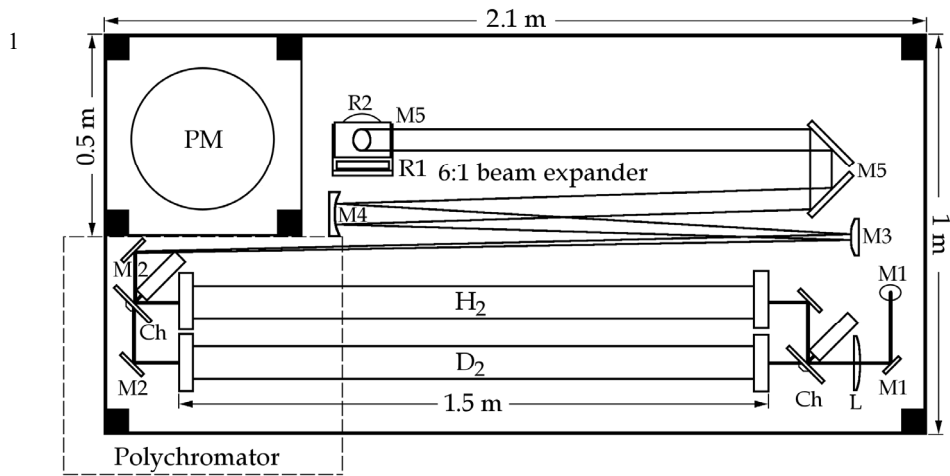
9



2 **Fig. 3.** Raman conversion efficiency ( $f = 1.0$  m) as a function of pressure for shifting the 248.5-nm radiation in  
3 hydrogen; the top curve (dark green) represents the sum of the residual pump energy and the first three Stokes  
4 emissions, normalized to the pump energy at zero pressure. The less important higher-Stokes emissions were not  
5 measured here, but may contribute above 4 bar which would shift the sum to higher values.

6  
7





2 **Fig. 5.** Lower compartment of the transmitter section of the mobile DIAL; the 266-nm beam enters vertically  
 3 from the top compartment and hits the first of the two M1 mirrors. The polychromator is located above the two  
 4 compartments as indicated by the broken line.

5 Abbreviations:

6 M1 ... high-reflecting mirror for 266 nm

7 M2 ... high-reflecting mirror for at least 266 – 300 nm

8 Ch .... rotating beam splitter (“chopper”)

9 L .....  $f = 1.00 \text{ m}$ , AR coated

10 M3 ... curved mirror,  $f = -0.20 \text{ m}$ , HR coated for at least 266 – 300 nm

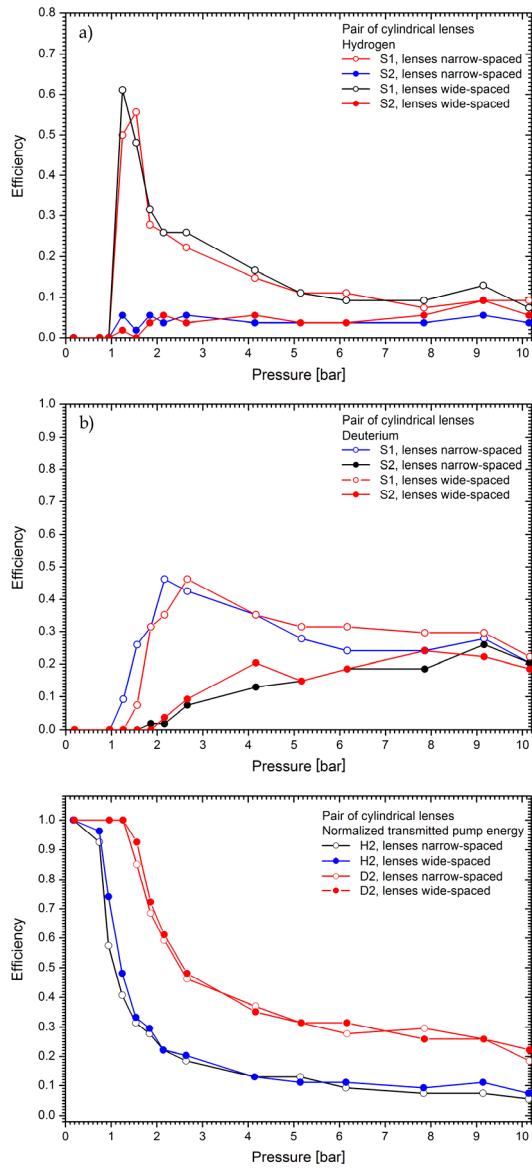
11 M4 ... curved mirror,  $f = -0.20 \text{ m}$ , coated for at least 266 – 300 nm

12 M5 ... rectangular mirrors, high-reflecting mirror for at least 266 – 300 nm

13 R1, R2 ... motorized rotation stages, mounted vertically and horizontally, respectively)

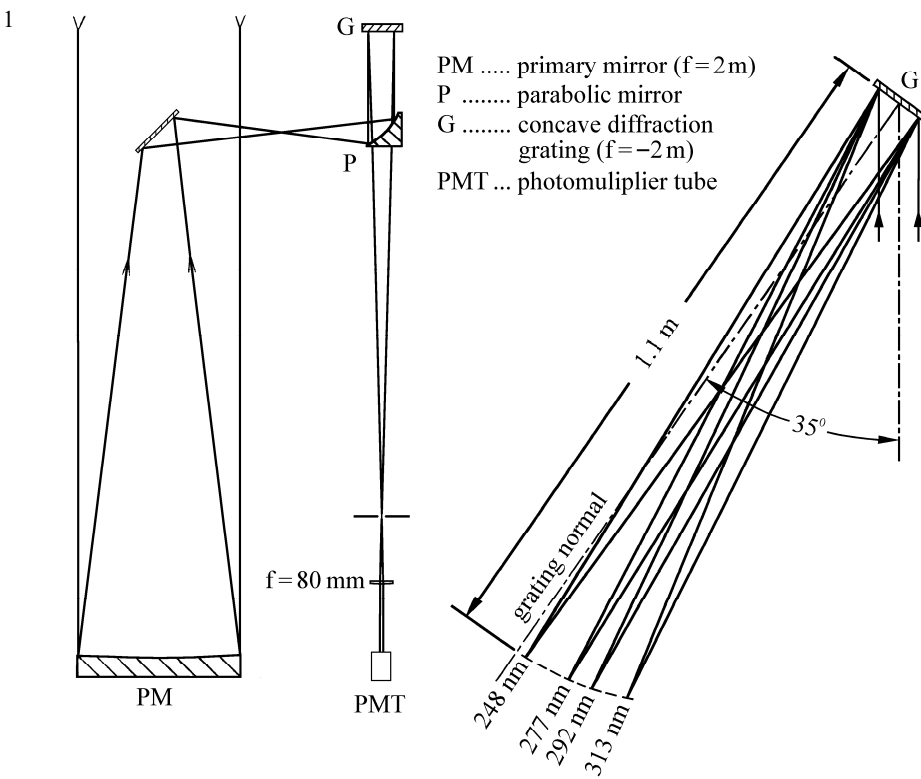
14

1

2 **Fig. 6.** Raman conversion efficiencies and pump-beam depletion for a pair of crossed  $f = **$  m cylindrical lenses:3 (a) S1 and S2 in hydrogen (b) S1 and S2 in deuterium (c) normalized transmitted pump energy in both  $H_2$  and4  $D_2$ .

5

6

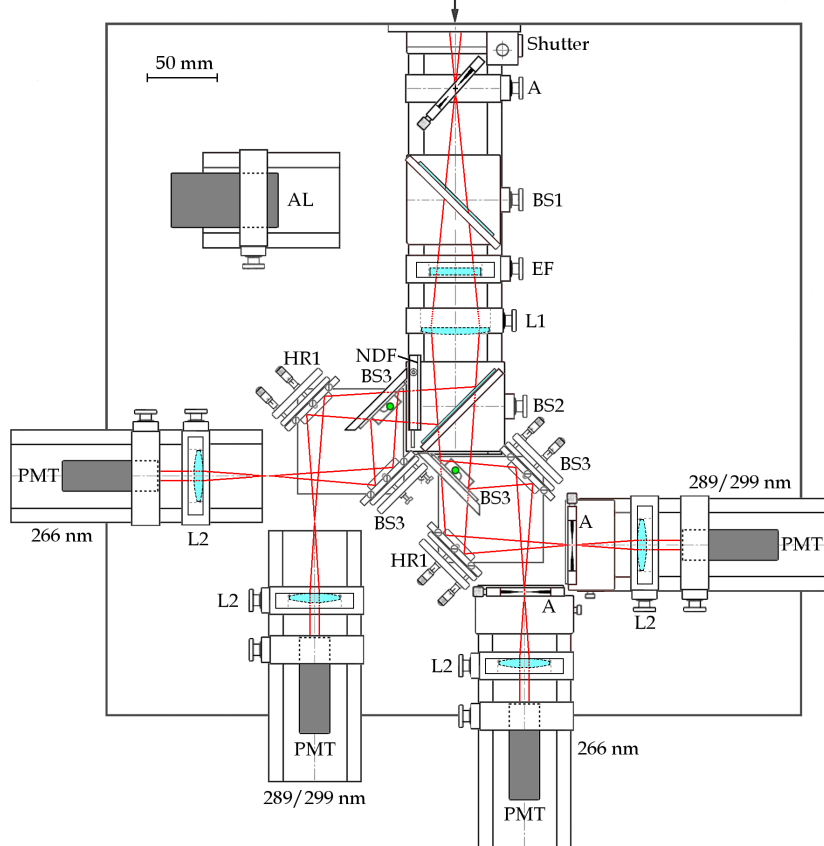


2 **Fig. 7.** Layout of the two grating spectrographs;  $\alpha = 35^\circ$  is the Wadsworth angle chosen, corresponding to a  
 3 wavelength of 240.0 nm. The choice of angle was limited by the space available in the housing of the  
 4 spectrograph, also considering the big PMTs initially used.

5

1

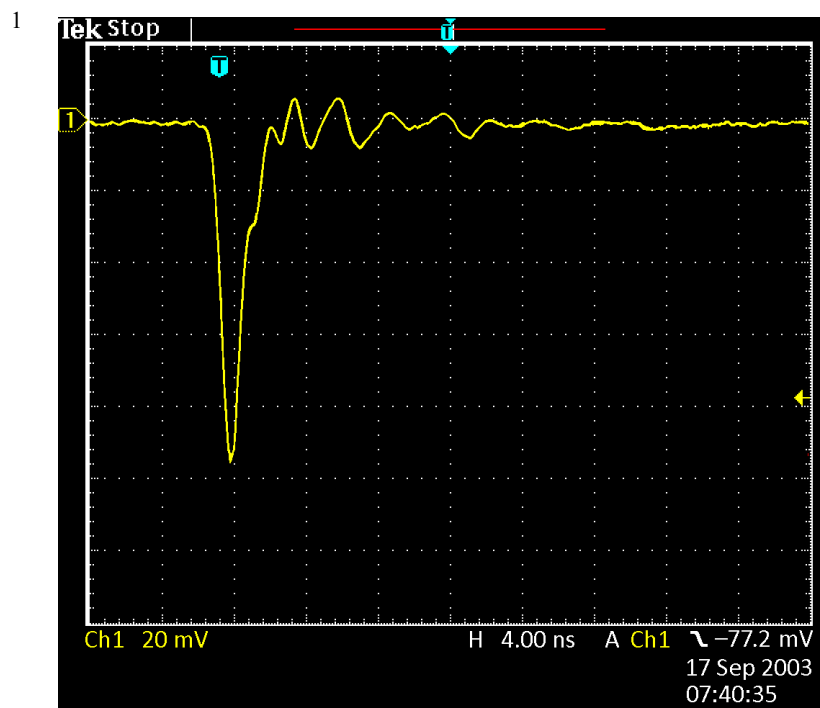
## Telescope



2 **Fig. 8.** Polychromator of the mobile ozone DIAL: The opto-mechanical components were mounted on a rail  
 3 system attached to a black optical table with a 25 mm  $\times$  25 mm hole pattern (M6 threads, not shown). The two  
 4 green dots mark the intermediate image planes of the primary mirror of the telescope. (the secondary image  
 5 planes coincide with the PMT cathodes). Abbreviations:

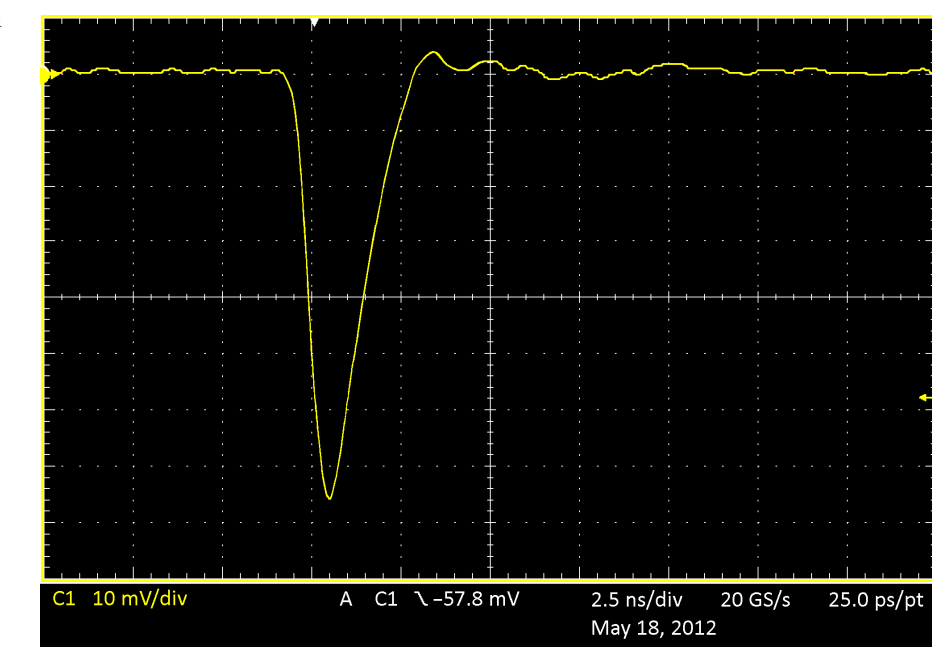
- 6 A ... rectangular aperture with four adjustable black blades
- 7 BS1 ... beam splitter for reflecting 532 nm or 1064 nm out of the received radiation for aerosol measurements  
 8 (not implemented)
- 9 BS2 ... 1:100 beam splitter for near-field – far-field separation
- 10 BS3 ... dichroic beam splitter with  $T < 4\%$  for 289 and 299 nm
- 11 HR1 ... high-reflecting mirror ( $45^\circ$ )
- 12 EF ... Dielectric edge filter, blocking the radiation above 299 nm
- 13 NDF ...  $T = 10\%$  neutral density filter
- 14 L1 ...  $f = 100$  mm lenses
- 15 L2 ...  $f = 50$  mm lens
- 16 AL ... alignment laser

17



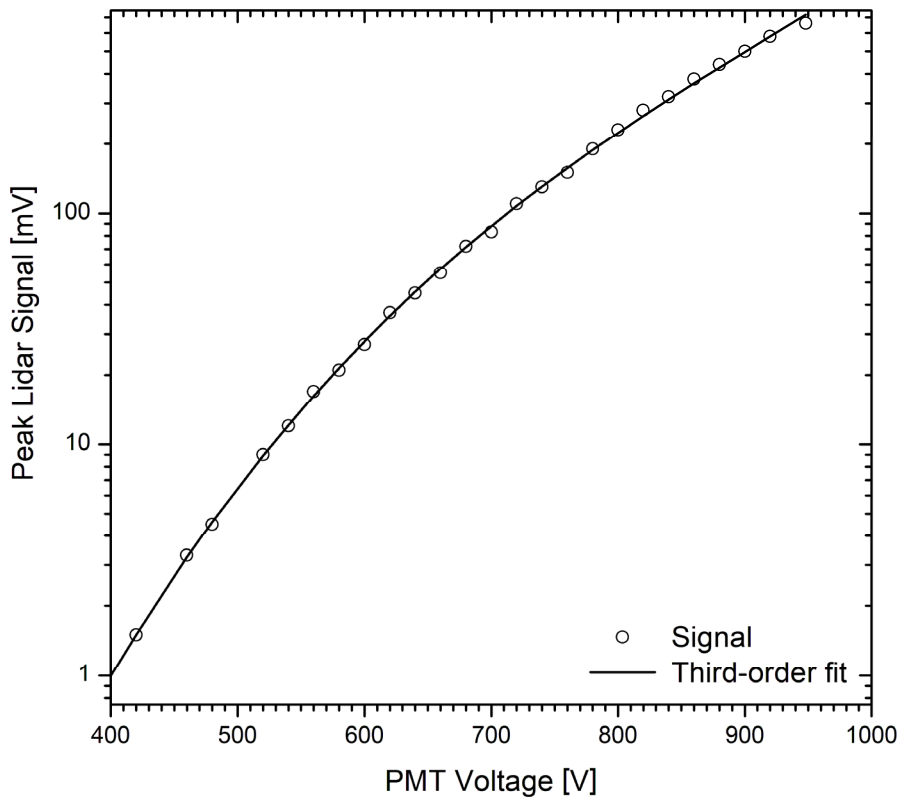
2 **Fig. 9a.** Single-photon pulse from a Hamamatsu 5600 or 7400 PMT, measured with a 500-MHz digital  
3 oscilloscope (Tektronix, TDS 3045 C)

4



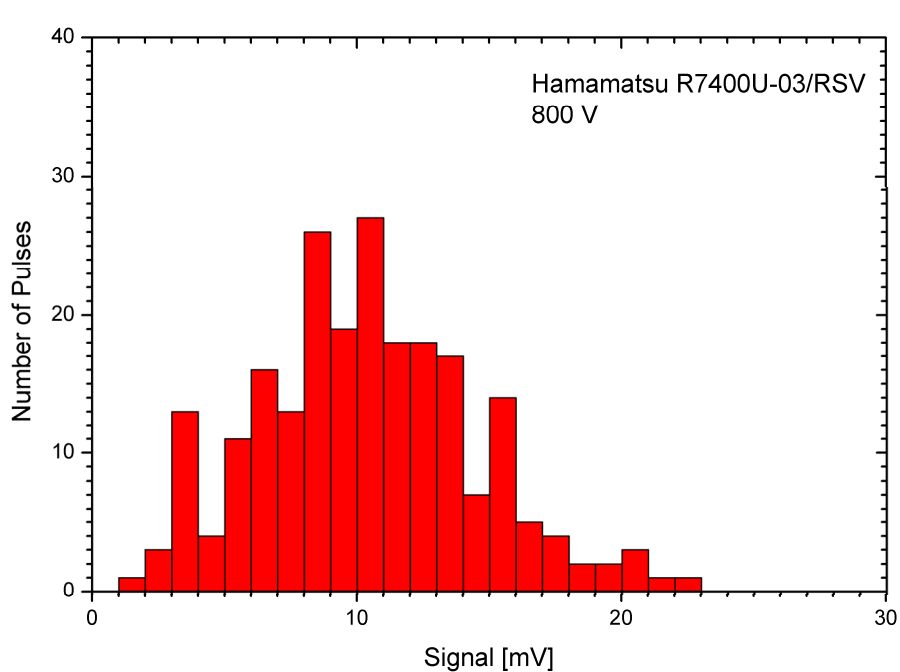
2 **Fig. 9b.** Single-photon pulse from a Hamamatsu R7400P-03 PMT with the most recent version of the Romanski  
3 (RSV) socket, measured with a 1-GHz digital oscilloscope (Tektronix, DPO 7104)

4

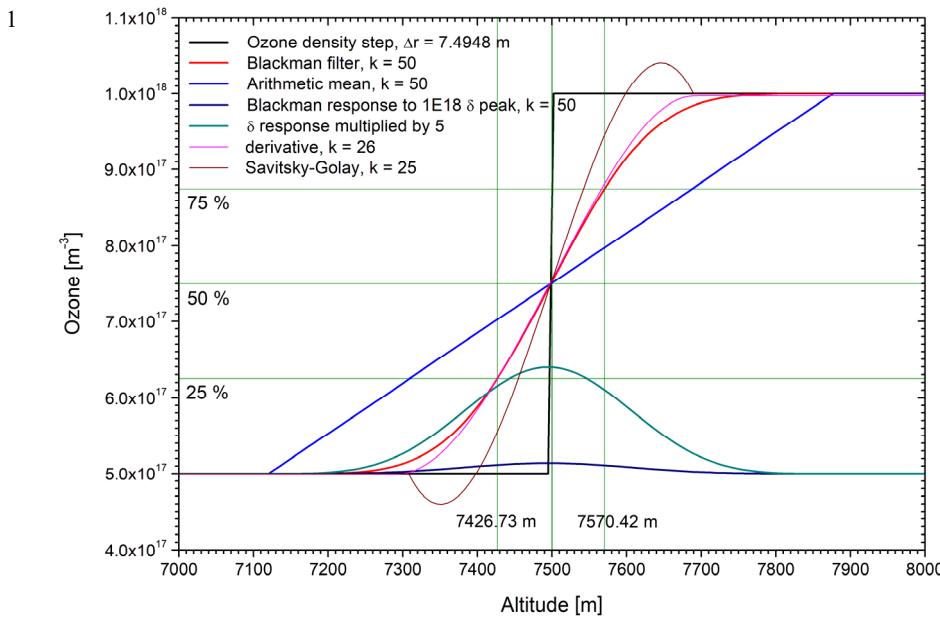


2 **Fig. 10.** Peak lidar signal measured with a R7400P-03 PMT as a function of the supply high voltage. The  
3 measurement was made for different attenuations of the incoming radiation, calibrating the data to the results for  
4 the standard settings. Signal-induced nonlinearities were only observed for very high photon fluxes, for which  
5 the supply voltage had to be reduced to 450 V to ensure signals below 100 mV (Kreipl, 2006).

6



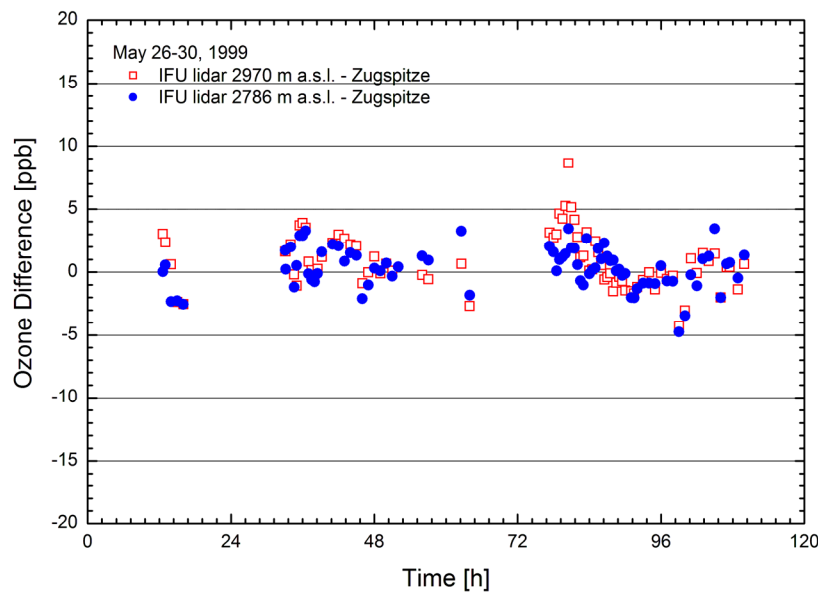
2 **Fig. 11.** Pulse height distribution of a Hamamatsu R7400-03 PMT (RSV module) for 800 V of operating voltage  
3 determined from a long time scan with a 1-GHz digital oscilloscope (sign of the pulse amplitudes inverted)  
4



2 **Fig. 12.** Response of the digital filter used in the data-evaluation procedure for the IFU DIAL systems to a  
3 Heaviside ozone step and for a sliding arithmetic mean, both filters shown for smoothing over 101 points; a  
4 digitizer bin size of 7.4948 m is assumed. The VDI vertical resolution is the altitude difference for a rise from 25  
5 % to 75 % of the input step. For comparison, the very small response of the Blackman filter to a delta (single-  
6 bin) signal peak of  $1 \times 10^{18}$  residing on a  $5 \times 10^{17}$  background is shown, the enhancement also multiplied by 5. The  
7 slope for a  $k = 27$  derivative filter (see text) is identical with that of the Blackman filter at half rise. Finally, the  
8 result of  $k = 25$  Savitsky-Golay smoothing is shown, 25 being the maximum possible  $k$  value in the ORIGIN  
9 graphics package. This kind of smoothing is absolutely inadequate.

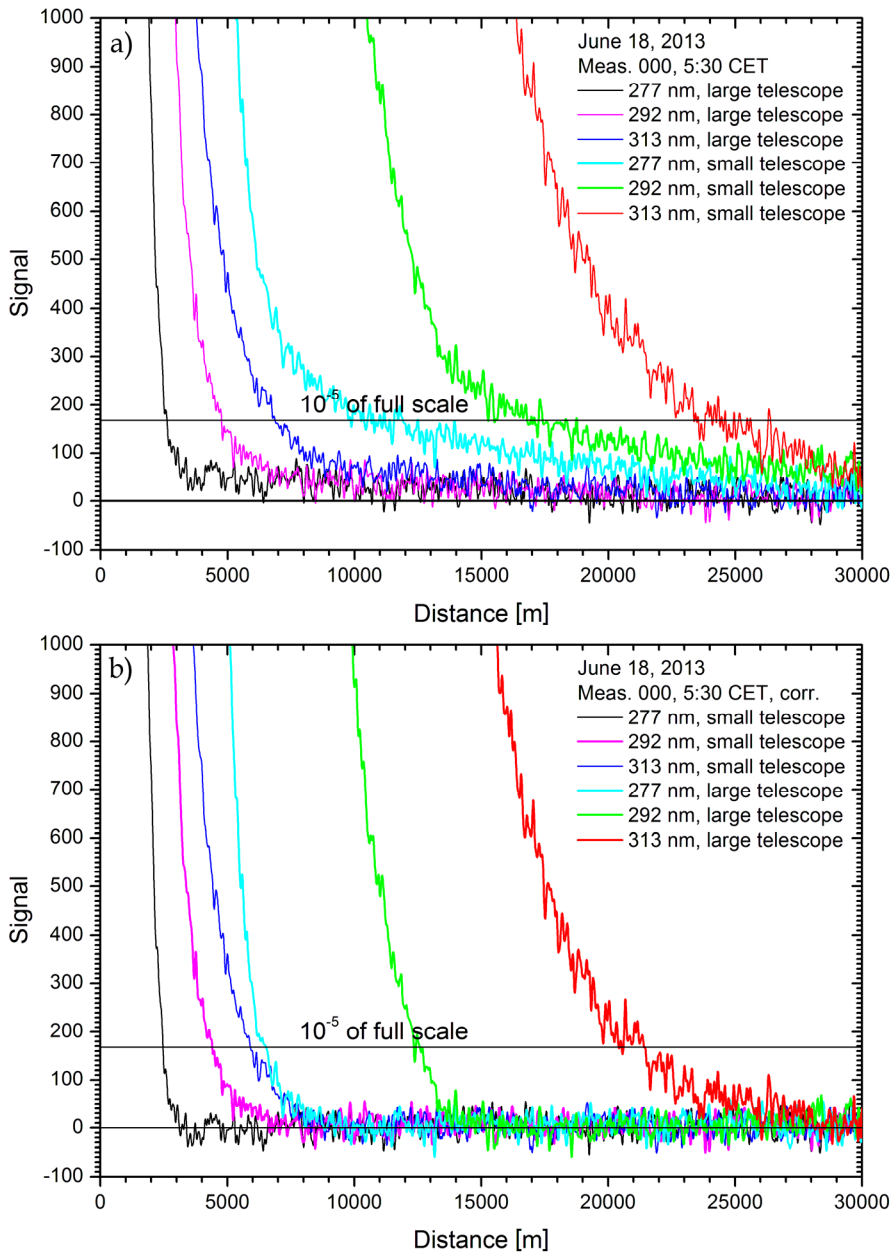
10

1



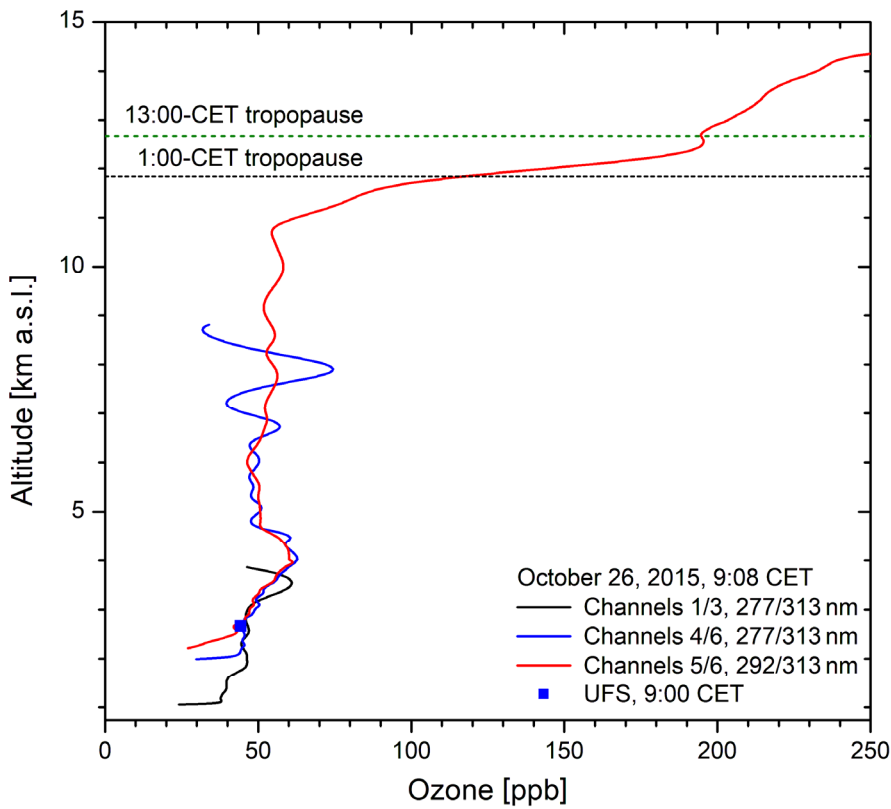
2 **Fig. 13.** Comparison of the stationary DIAL with the Zugspitze in-situ data during four days in May 1999  
3 (VOTALP "Munich" field campaign); the deviations have diminished to about one half of the noise shown here  
4 ever since.

5  
6



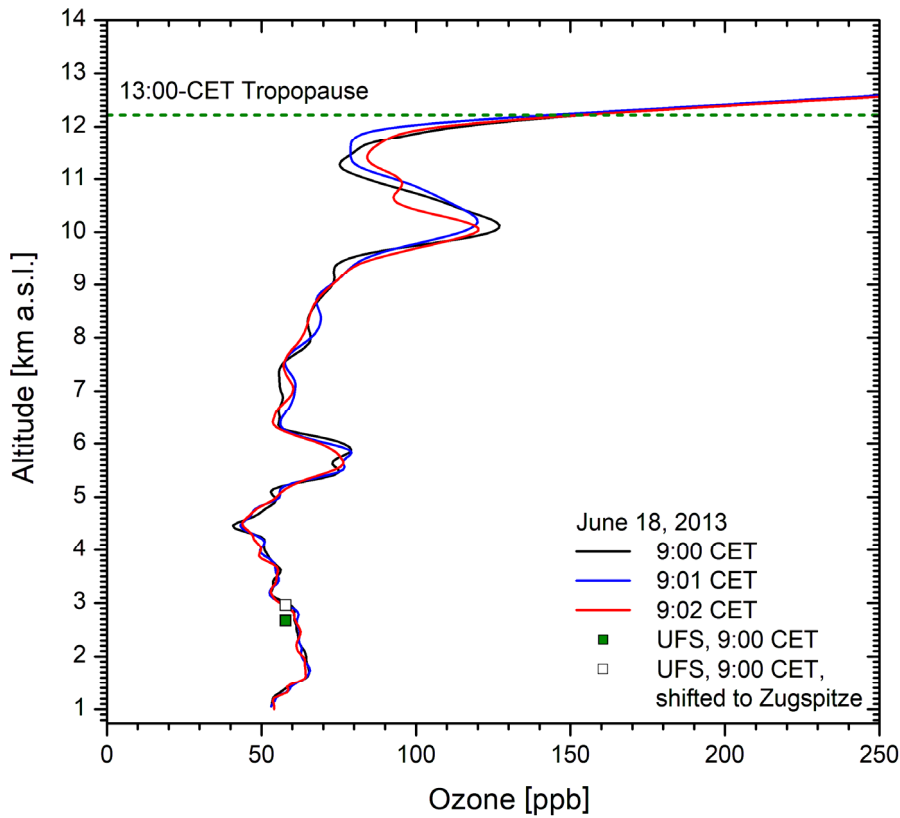
2 **Fig. 14.** Strongly expanded backscatter profiles without (a) and with (b) exponential correction, recorded after  
3 the introduction of the ground-free input stage to the transient digitizers in late 2012; the 313-nm signals are  
4 noisier due to the early-morning daylight background. The data are smoothed over  $\pm 14$  points (VDI vertical  
5 resolution 40 m) in order to reduce the digital ripple.

6



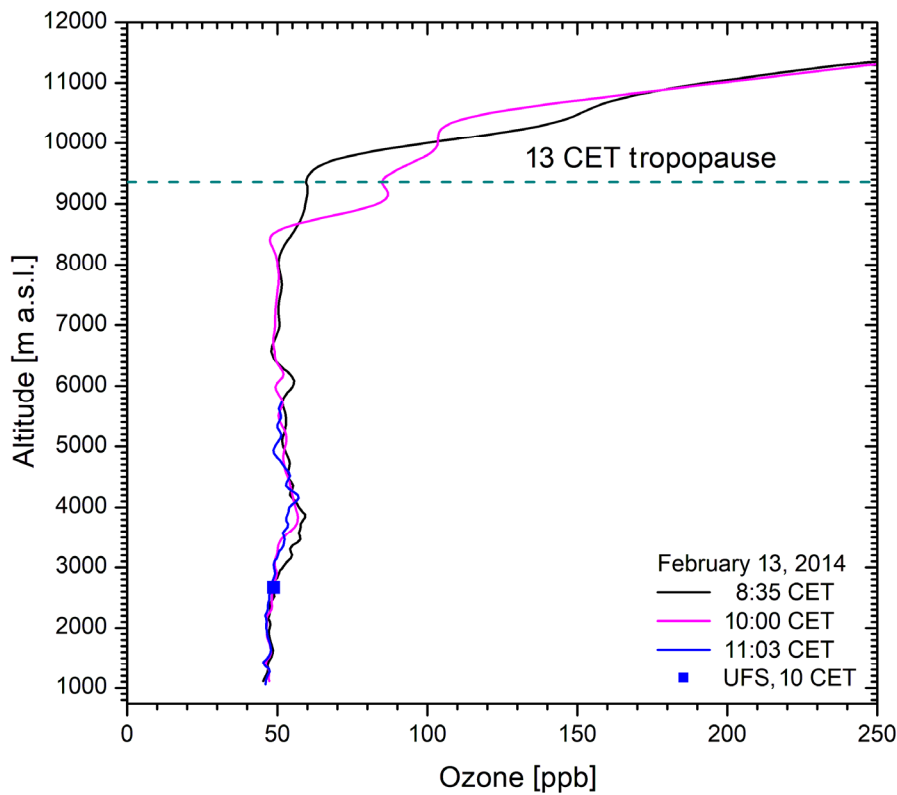
2 **Fig. 15.** Selection of partial ozone profiles from both receivers of the stationary: The near-field result can be  
 3 used here to more than 2 km above the lidar due to low ozone density. The ozone hump between about 3.0 and  
 4 4.8 km is caused by a remote stratospheric air intrusion. The lidar measurement agrees with that at the nearby  
 5 Schneefernerhaus station (UFS, 2670 m; 0.7 ppb below blue curve). The altitude of the tropopause is taken from  
 6 the Munich radiosonde.

7



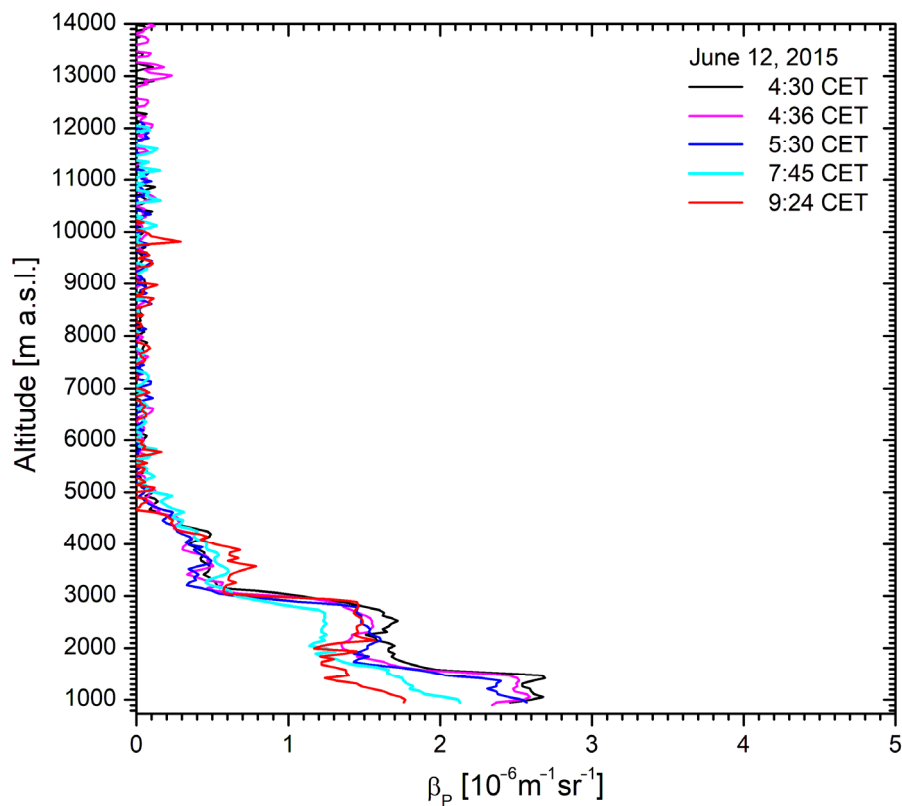
2 **Fig. 16.** Example for reproducibility testing during a period of elevated ozone: The “on” wavelengths used are  
 3 277 nm (channel 1, near-field telescope, up to 2.23 km), 277 nm (channel 6, up to about 6 km) and 292 nm  
 4 (channel 5, up to the top). The lidar measurement perfectly agrees with that at UFS if the altitude is shifted to  
 5 that of the Zugspitze summit (2962 m), justified by the southerly advection. Above 5 km the signal in channel 6  
 6 becomes low due to the high ozone values in the lower troposphere and a weighted average of the 277/292 nm  
 7 ozone profile with that for 292/313 nm was applied for the final few hundred metres below 6 km. Above 9 km  
 8 the 292-nm signal starts to become noisy resulting in reduced reproducibility. The altitude of the tropopause is  
 9 taken from the Munich radiosonde.

10

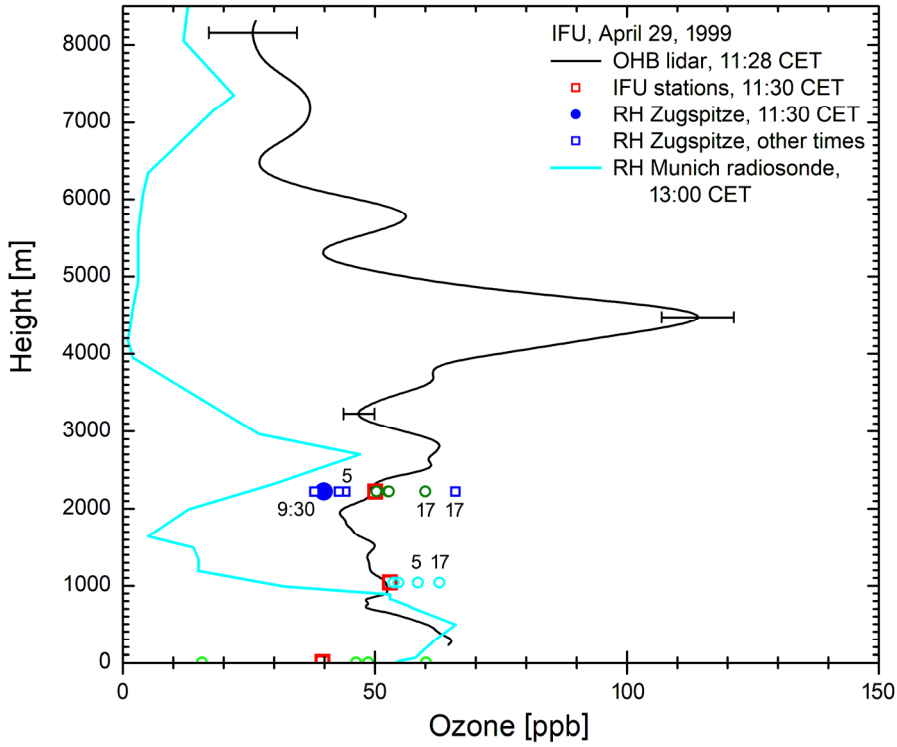


2 **Fig. 17:** Ozone measurement with the stationary DIAL on 13 February 2014; the variability is low apart from the  
 3 two dry layers at below 4 km and at 6.1 km that are also visible in the 1-CET Munich radiosonde data and that  
 4 seem to erode after 8:35 CET. The agreement with the in-situ measurements at UFS is perfect.

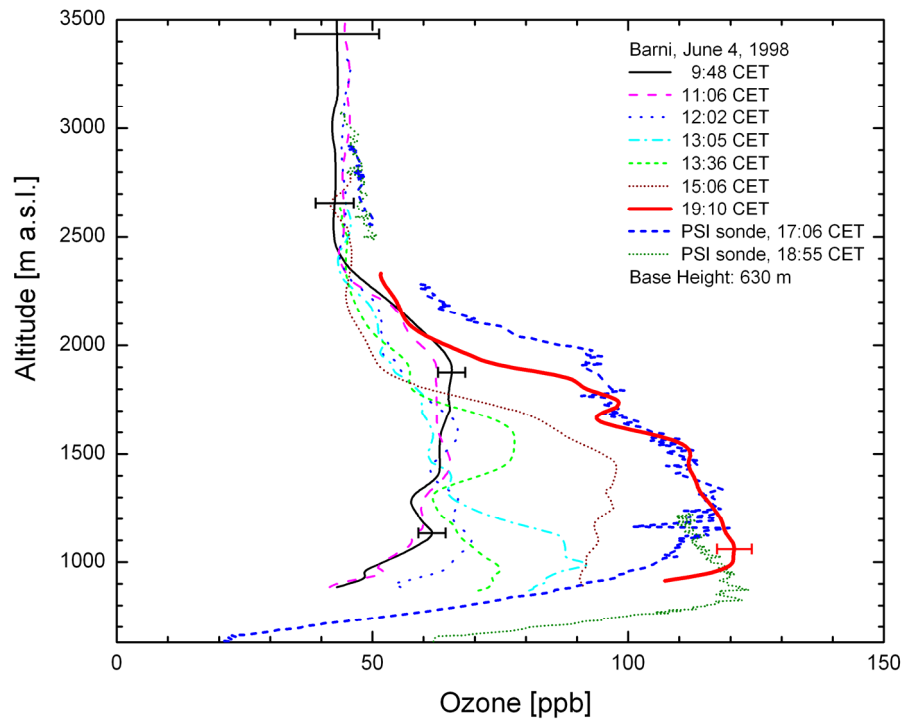
5



2 **Fig. 18.** 313-nm aerosol backscatter coefficients for 12 June 2015



2 **Fig. 19.** Ozone measurement with the mobile DIAL during the brightest part of the day, after all modifications  
 3 had been made (about  $10^4$  laser shots): The vertical axis is the height above the lidar site (IFU, 730 m a.s.l.): Up  
 4 to 2.7 km above the ground 266-299-nm wavelength pairs were taken (near-field: up to 1.5 km). Up to 3.7 km  
 5 the combination 289-299 nm was used. Above this, ozone was obtained from a single-trace evaluation for 299  
 6 nm, slightly recalibrated at the lower end of that range. For comparison, in-situ ozone values from the three local  
 7 monitoring stations IFU (745 m a.s.l.), Wank (1780 m a.s.l.) and Zugspitze (2962 m a.s.l.) are shown for 11:30  
 8 CET, (red squares). Additional values from these stations are marked with open circles for 5:00 CET, 9:30 CET,  
 9 14:00 CET and 17:00 CET (labelled in some cases). For the interpretation of the complicated meteorological  
 10 situation, the corresponding relative-humidity of the Zugspitze summit and the noon operational ascent of the  
 11 Munich radiosonde are also included. Outside the most reliable part of the operating range a few representative  
 12 error bars are drawn.  
 13



2 **Fig. 20.** Ozone measurements at Barni (Provincia di Como, Italy) on 4 June 1998, during the VOTALP Milano  
 3 field campaign; the profiles show the day-time gradual advection of the Milano ozone plume. The ozone sonde  
 4 data from the two launches at the lidar site have been kindly supplied by J. Keller (Paul-Scherrer-Institut,  
 5 Switzerland; the times are launch times). Only 266 nm could be used as the “on” wavelength. As a consequence  
 6 the range was strongly reduced during the period with the highest ozone mixing ratio.  
 7